# REPORT DOCUMENTATION PAGE

Form Approved
OMB No. 0704-0188

Public reporting burden for this collection of information is estimated to average 1 hour per response, including the time for reviewing instructions, searching existing data sources, gathering and maintaining the data needed, and completing and reviewing the collection of information. Send comments regarding this burden estimate or any other aspect of this collection of information, including suggestions for reducing this burden, to Washington Headquarters Services, Directorate for Information Operations and Reports, 1215 Jefferson Davis Highway, Suite 1204, Arlington, VA 22202-4302, and to the Office of Management and Budget, Paperwork Reduction Project (0704-0188), Washington, DC 20503

| 1. AGENCY USE ONLY (Leave blank) | 2. REPORT DATE | 3. REPORT TYPE AND DATES COVERED |
|---|---|---|
| | March 6, 1995 | Final Report Oct 1, 1992-Sept 30, 1994 |

**4. TITLE AND SUBTITLE**
Novel High-Power Solid-State Sources for the Millimeter-Wave Region

**5. FUNDING NUMBERS**
61102F
2305BS

19950329 035

**6. AUTHOR(S)**
E. R. Brown

**7. PERFORMING ORGANIZATION NAME(S) AND ADDRESS(ES)**
Lincoln Laboratory, Massachusetts Institute of Technology
High Speed Electronics Group
244 Wood Street
Lexington, MA 02173-9108

**. PERFORMING ORGANIZATION REPORT NUMBER**
AFOSR-TR-95-0237
232-8-201

DTIC
SELECTED
MAR 31 1995
S G

**9. SPONSORING/MONITORING AGENCY NAME(S) AND ADDRESS(ES)**
Air Force Office of Scientific Research
110 Duncan Avenue, Suite 115B
Bolling AFB
Washington, DC 20332

**10. SPONSORING/MONITORING AGENCY REPORT NUMBER**
AFOSR PD 94-~~004~~ 0002

**11. SUPPLEMENTARY NOTES**
The view, opinions and/or findings contained in this report are those of the author(s) and should not be construed as an official Department of the Army position, policy, or decision, unless so designated by other documentation.

**12a. DISTRIBUTION/AVAILABILITY STATEMENT**
Approved for public release; distribution unlimited.

**12b. DISTRIBUTION CODE**

**13. ABSTRACT** *(Maximum 200 words)*

The goal of this two-year program was to create two new sources for ultrafast electronic circuits. Two technical approaches were pursued. The first was a cw optoelectronic photomixer using low-temperature-grown (LTG) GaAs as the active material. Prior to this research, little work had been done on cw photomixers at millimeter-wave (i.e., f > 30 GHz) or higher frequencies. The primary limitation was the lack of a suitably fast photoconductive material. LTG GaAs is a promising material for this application because of its short photoconductive lifetime and robust electrical properties. Through the research carried out on this program, the photomixer was developed into a very useful source for frequencies above 100 GHz. The second approach was an electronic pulse generator using a resonant-tunneling diode (RTD) as the active device. The basis for this generator was the high switching speed of the RTD when connected to a low-impedance transmission line. Previous work had produced single high-speed switching events in RTDs, but the switching d not been made self-induced and repetitive. In this effort self-generated pulse trains were produced having a pulse width of approximately 25 ps, a repetition rate up to 3 GHz, and a pulse amplitude of approximately 0.5 V. One attractive feature of the RTD pulse generator is that it can be modified to generate several useful types of pulse waveforms, such as the impulse function and square waves.

| 14. SUBJECT TERMS | 15. NUMBER OF PAGES |
|---|---|
| Low-temperature-grown GaAs, photoconductive mixing, terahertz radiation, resonant tunneling diode, pulse generation, relaxation oscillations. | 29 |
| | 16. PRICE CODE |

| 17. SECURITY CLASSIFICATION OF REPORT | 18. SECURITY CLASSIFICATION OF THIS PAGE | 19. SECURITY CLASSIFICATION OF ABSTRACT | 20. LIMITATION OF ABSTRACT |
|---|---|---|---|
| UNCLASSIFIED | UNCLASSIFIED | UNCLASSIFIED | UL |

Accesion For
NTIS CRA&I [X]
DTIC TAB [ ]
Unannounced [ ]
Justification
By
Distribution /
Availability Codes
Dist | Avail and / or Special
A-1

# NOVEL HIGH-POWER SOLID-STATE SOURCES FOR THE MILLIMETER-WAVE REGION

FINAL REPORT

Name of Contractor: Lincoln Laboratory
Massachusetts Institute of Technology
Lexington, MA 02173-9108

DTIC ELECTE MAR 31 1995 G

Effective Date of Contract: Oct. 1, 1992

Contract Expiration Date: Sept. 30, 1994

Principal Investigator: Dr. Elliott R. Brown
(617) 981-7844

Short Title of Work: Millimeter-Wave Coherent Sources

Contract Report Period Covered: 1 Oct. 1992 to 30 Sept. 1994

This work was sponsored by:

Air Force Office of Scientific Research
AFOSR/NE
Bolling Air Force Base, D.C. 20332
Monitored by Dr. Gerald Witt

The views and conclusions contained in this document are those of the contractor and should not be interpreted as necessarily representing the official policies, either expressed or implied, of the United States Government.

# 1. INTRODUCTION

This is the final report for the program entitled "Novel High-Power Solid-State Sources for the Millimeter-Wave Region," which was undertaken from 1 October 1992 through 30 September 1994. The primary goal of this program was to create two new sources for ultrafast electronic circuits. Two technical approaches were pursued. The first was a cw optoelectronic photomixer using low-temperature-grown (LTG) GaAs as the active material. Prior to this research, little work had been done on cw photomixers at millimeter-wave (i.e., f > 30 GHz) or higher frequencies. The primary limitation was the lack of a suitably fast photoconductive material. LTG GaAs was a promising material for this application because of its short photoconductive lifetime and robust electrical properties. The LTG GaAs photomixers would utilize the low-temperature MBE technology developed at Lincoln Laboratory in the late 1980s. Through the research carried out on this program, the photomixer was developed into a very useful source for frequencies above 100 GHz.

The second approach was an electronic relaxation oscillator using a resonant-tunneling diode (RTD) as the active device. The basis for this generator was the high switching speed of the RTD when connected to a low-impedance circuit. Although some experiments had been conducted to measure the switching speed experimentally, the switching process had not been made repetitive. Two attractive aspects of the RTD relaxation oscillator were that it could generate useful types of pulse waveforms, such as the impulse function, and that it could readily be integrated monolithically on GaAs or InP wafers. The relaxation oscillator was fabricated using the thin-heterobarrier MBE technology perfected at Lincoln Laboratory during the 1980s. Through the research carried out on this program, the relaxation oscillator was demonstrated at microwave frequencies and modeled up to 1 THz.

A significant by-product of this program was the set of applications that it spawned. The LTG GaAs photomixer is now being used in three different scientific areas: (1) as a highly-tunable coherent source in molecular spectroscopy, (2) as a THz-bandwidth optoelectronic mixer for laser metrology, and (3) as a fixed-frequency local oscillator in THz radiometric systems. The first two applications are being pursued at the National Institute of Standards and Technology (NIST) laboratories in Gaithersburg, MD, and Boulder, CO, respectively. The third application is being pursued at the NASA Jet Propulsion Laboratory and the California Institute of Technology. The RTD relaxation oscillator has been used and is being further investigated as a diode-laser driver in optical communications systems. A variant of the relaxation oscillator, a RTD-loaded active transmission line, has recently attracted great interest as an active interconnect for massively parallel computers. Each of these applications is discussed in great detail in Sec. 3.

## 2. PROGRAM OBJECTIVES

To achieve a useful LTG GaAs photomixer, the first objective was to acquire a theoretical understanding of some of the salient physical issues related to optical mixing in LTG material. For example, it was essential to predict to some level of accuracy the optical-to-electrical (O-E) conversion efficiency. Unless this efficiency was much greater than that of the competitive techniques of optical three-wave mixing and electrical harmonic conversion, there was little point in pursuing the photomixer for practical applications. After this theoretical exercise, the photomixer effort was mostly experiments aimed at the following objectives: (1) determine the optimum GaAs material relative to pump wavelength, (2) confirm that the very short response time measured in earlier measurements of LTG GaAs by time-resolved techniques would translate into the frequency domain of photomixing, and (3) ascertain the maximum O-E conversion efficiency and the limitations thereof. The final objective was a useful application, which turned out to be an optoelectronic sweep oscillator for molecular spectroscopy at NIST, Gaithersburg.

To achieve a useful relaxation oscillator, it was first necessary to carry out some sophisticated computer simulations of an RTD connected to a length of transmission line. The objective here was to understand the dynamics of the oscillator and the effects of non-ideality in the RTD and transmission-line. Once these simulations were completed, experimental work commenced in earnest and was aimed at the following objectives: (1) determine the maximum repetition frequency and minimum pulse width achievable in a hybrid-packaged relaxation oscillator, and (2) fabricate a monolithic RTD relaxation oscillator and determine its speed and amplitude limits. The final objective was to use the relaxation oscillator in a useful application, which turned out to be a diode-laser driver experiment in the optical communications group at Lincoln Laboratory.

## 3. ACCOMPLISHMENTS

The discussion of accomplishments on this program will be split into the two topical areas, and will follow closely the objectives discussed above. Frequent reference will be made to publications collected as Appendices at the end of this report.

## 3.1. LTG GaAs PHOTOMIXERS

### *3.1.1. Photomixer Theory and Comparison with other Techniques*

The first effort in this program was a theoretical exercise aimed at determining the operational characteristics of the LTG-GaAs photomixer. The details are given in the reprint of Appendix A. In summary, an analytical model was developed based on the assumption that when the LTG GaAs is pumped by radiation lying just above the band gap (i.e., $\lambda \leq 850$ nm), it behaves like a photoconductor with a single time constant equal to the electron-hole lifetime $\tau_{eh}$. This assumption was consistent with earlier work done on LTG switches and detectors in Prof. Mourou's group at the University of Michigan, and is mostly consistent with our subsequent work on high-frequency photomixers discussed below. The photomixer operates by the fact that two pump lasers offset in frequency by f generate in the LTG GaAs a time varying conductance at the same frequency. When the photomixer is connected to a constant-voltage bias, the time varying conductance leads to a time varying current. The latter current is readily coupled to output circuits, such as transmission lines and planar antennas, to generate power.

With these considerations we predicted (Appendix A) that in photomixers constructed by fabricating interdigitated electrodes directly on the LTG GaAs, the O-E conversion efficiency to low difference frequencies could be as high as a few percent and the 3-dB electrical bandwidth could be at least 250 GHz. Most importantly, the bandwidth could designed to be limited by $\tau_{eh}$ and not the parasitic RC time associated with the resistive part of the load circuit and the interdigitated-electrode capacitance. Such numbers were calculated for just tens of milliwatts of optical pump power in each laser beam. This engendered a sense of confidence in the overall photomixer approach because single-frequency solid-state lasers (i.e., Ti:$Al_2O_3$) were readily available that could pump the LTG GaAs above its band gap and put out at least 100 mW of power each.

The analysis also served to contrast the LTG-GaAs photomixer against other techniques for generating tunable THz coherent radiation. One such technique is three-wave mixing in nonlinear crystals, whose maximum conversion efficiency is limited fundamentally by the Manley-Rowe relation:

$$\frac{P_f}{f} = \frac{P_1}{\nu_1} + \frac{P_2}{\nu_2}$$

where $\nu_1$ ($P_1$) and $\nu_2$ ($P_2$) are the optical frequencies (powers) and f ($P_f$) is the difference-frequency (power). For example, using pump lasers around 0.8-μm wavelength and a 300 GHz frequency difference, we calculate a maximum conversion efficiency of 0.05%. And this

neglects the important practical problem of phase matching. In contrast, the analysis in Appendix A showed that even with heating and impedance-matching effects considered, the LTG-GaAs photomixer is capable of at least a 5% O-E conversion efficiency for the same pump conditions. Experience with three-wave mixing has shown that imperfect phase matching drops the conversion efficiency several more orders of magnitude, as exemplified by the $2\times10^{-9}$ efficiency from $CO_2$-laser wavelengths (approximately 10 μm) to millimeter wavelengths. Because the photomixer is not limited by the Manley-Rowe relation and does not require phase matching, it could, in principle, yield an O-E efficiency exceeding unity. Note, however, that this would require that the LTG-GaAs exhibit photoconductive gain, which has not yet been observed experimentally.

The photomixer analysis also highlighted its inherent simplicity compared to the all-electronic technique based on harmonic generation in non-linear devices. The standard device in this technique is the Schottky varactor diode. The difficulty in this technique is that solid-state devices only extend up to just over 100 GHz, so that to get to THz frequencies high-order harmonics must be generated or else lower-order multipliers must be used in tandem. In either case, the circuits required are very complicated because with each harmonic comes an idler frequency, which must be properly terminated to achieve high output power on the desired harmonic. In contrast, when the LTG-GaAs photomixer is pumped with the cw power levels considered in this program (< 0.5 W from each laser), the only significant time variation in the photocurrent is at the laser difference frequency. There is no harmonic of either laser (at least not in the photocurrent) and there is no harmonics or idlers of the difference frequency unless the pump power drives the conductance of the photomixer to the level of the load conductance. With cw optical pumping, heating becomes a problem long before this point is reached.

Finally, our analysis showed clearly how the LTG-GaAs photomixer compared in absolute power to more common optoelectronic terahertz-generation techniques based on optically triggered photoconductive switches coupled to antennas or transmission lines. The key is that photomixer concentrates all of its photocurrent at one (difference) frequency and, therefore, generates a much greater power spectral density $S_p$, (defined as the average power generated per unit Hz of bandwidth). For the photomixer, the highest spectral density generated up to 300 GHz to date is the ratio of the highest power of approximately 50 μW, to the instantaneous linewidth, which is roughly 10 KHz for two Ti:sapphire pumps. This yields $S_p \approx 5\times10^{-9}$ W/Hz, which as discussed above, is expected to increase substantially by increasing the pump power and providing better cooling of the photomixer element. For photoconductive switching devices driven by mode-locked optical lasers, $S_p \approx (V^2/R_A)\,(f_{rep}\tau)/\Delta f$, where V is the dc bias voltage across the photoconductive gap, $R_A$ is the radiation resistance of the load antenna or the characteristic impedance of the transmission line, $f_{rep}$ is the repetition rate of the mode-

locked laser, and $\tau$ and $\Delta f$ are the electrical switching time and bandwidth of the overall circuit in which the photoconductive gap is embedded. Using representative values of V = 100 V, $R_A$ = 100 Ω, $f_{rep}$ = 100 MHz, $\tau$ = 1 ps, and $\Delta f$ = 100 GHz, we find $S_p \approx 1\times10^{-13}$ W/Hz. This spectral density is the relevant figure of merit for many applications of coherent sources, such as coherent tunable spectrometers for molecular spectroscopy, local oscillators in terahertz radiometers, and sweep oscillators for device and material diagnostics. The much higher terahertz peak power of the switched sources may be useful in pulsed applications such as radar.

### *3.1.2. Material Growth*

Our LTG InGaAs was grown by molecular-beam epitaxy (MBE) at a temperature in the range of 180 to 250 °C and in the presence of arsenic over pressure in the growth chamber. The first several wafers for our program were grown in an old Varian Gen II system that was originally used to investigate LTG GaAs from its beginnings in the mid-1980s. Although it had only 2-inch substrate capability, the fact that the substrates were indium-soldered to the block lead to good temperature control. The last few wafers for our program were grown in a relatively new Intevac Gen II system designed for 3-inch substrates. This machine contained a BN solder-free sample holder that was convenient and gave very reproducible growths, but its temperature could not be precisely calibrated. Independent of the MBE machine, the resulting LTG material was nonstoichiometric with about 1% excess arsenic. After growing approximately 1 μm of material, the gallium source is closed. A thermal anneal is then carried out at approximately 600 °C in the arsenic flux for a duration of 10 minutes. The thermal anneal causes the large concentration of excess arsenic atoms to rearrange either as antisite defects (i.e., an arsenic atom at a gallium site) or to cluster together as metallic arsenic precipitates. The relationship between the defects and the desirable characteristics (i.e., high resistivity and short photoconductive lifetime) is somewhat controversial. One school of thought, started by Lincoln Laboratory and the University of California at Berkeley, attributes these characteristics exclusively to the high concentration ($\approx10^{18}$ $cm^{-3}$) of antisite defects, which leads to very low background-carrier concentrations and a high probability of Shockley-Read-Hall-like recombination. The other school of thought, started mostly by IBM and Purdue University, attributes these characteristics to the short distance between the precipitates, which leads to a depletion of background carriers and a high probability for recombination of photocarriers close to the site of their generation.

### *3.1.3 Time-Resolved Lifetime Measurement*

For the photomixer application, the most important characteristic of the LTG GaAs is the electron-hole photocarrier lifetime, $\tau_{eh}$. To determine this quantity, we used the technique of time-resolved photoreflectance depicted in Fig. 1. This is a pump-probe technique in which the

optical pulse train from a Ti:$Al_2O_3$ mode-locked laser is split into two separate beams. The more powerful pump beam is directed through an optical delay line, mechanically chopped, and then focused on the surface of the LTG-GaAs epitaxial layer where it excites electron-hole pairs. The probe beam is focused onto the same spot as the pump beam and the average power of the reflected probe beam is measured with a slow photon detector as the delay line varies the optical path length of the pump beam. The change in path length is equivalent to a time delay of the probe beam with respect to the pump beam. The photon detector is connected to a lock-in amplifier synchronized at the chopper frequency, so that the output signal of the lock-in amplifier is sensitive only to changes in the reflectivity induced by the pump beam. As the time delay of the pump beam is varied so that the pump and probe pulses arrive at the LTG-GaAs layer simultaneously, the pump has its maximum effect, as shown in the inset of Fig. 1. As the probe beam is delayed further, the signal strength drops off over a time scale directly related to the lifetime of the photocarriers induced by the pump. The accuracy of this method is limited only by the finite length of the pump and probe pulses, which in our laser is approximately 80 fs.

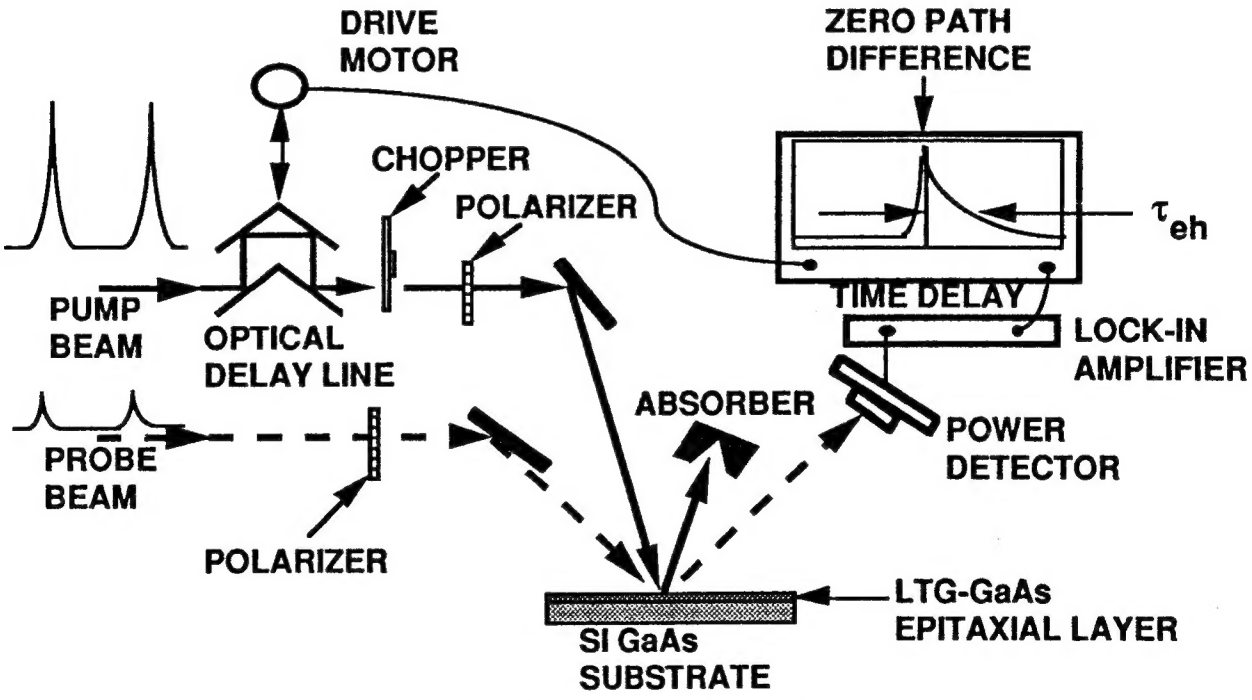


Fig. 1. Time-resolved photoreflectance experiment.

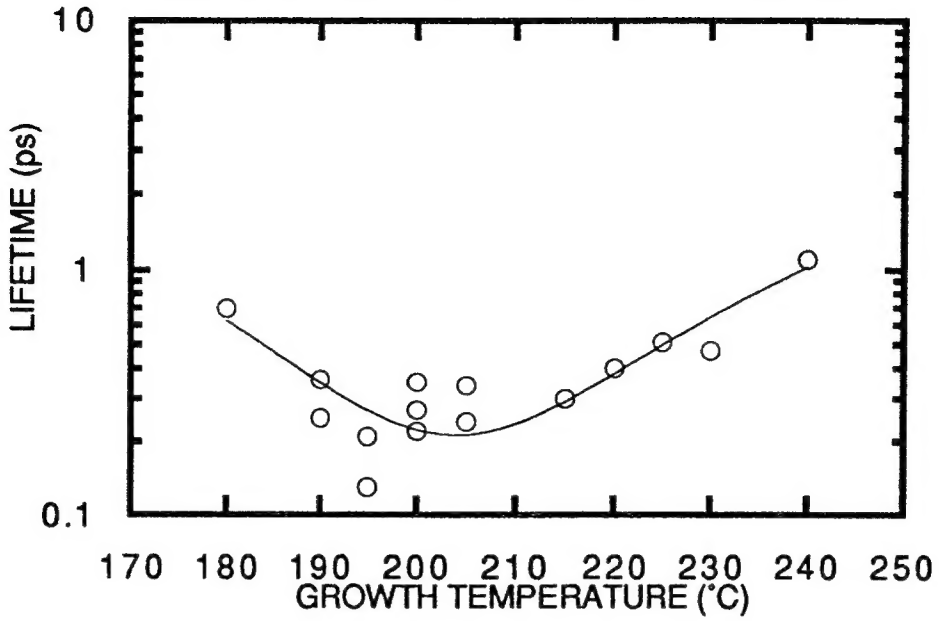


Fig. 2. Experimental results of photocarrier lifetime vs MBE growth temperature.

Shown in Fig. 2 are the experimental results for $\tau_{eh}$ measured for a variety of LTG-GaAs samples grown between 180 and 240 °C. Over this entire temperature range, the lifetime is below 1 ps. The best samples for photomixers are those grown between about 190 and 210 °C, in which the lifetime is in the range of 0.2 to 0.4 ps. The minimum lifetime that we have observed is 0.15 ps in a sample grown at 195 °C. This temperature defines a rough minimum in the lifetime vs growth temperature represented by the solid curve fit shown in Fig. 2.

### *3.1.4. CW Optical Pumping Set Up*

A schematic diagram of the laser pumping configuration used in our experiments is shown in Fig. 3 and discussed in more detail in Appendix B. It consists of two Ti:$Al_2O_3$ lasers, each pumped by an argon-ion laser. One of the Ti:$Al_2O_3$ lasers has a standing-wave optical cavity and is kept at a fixed wavelength of about 800 nm over the course of the experiments. The output power of this laser is typically in the range of 0.1 to 0.5 W depending on the ion-laser pump power. The output is divided between, at most, two longitudinal modes separated in frequency by 200 MHz. The other Ti:$Al_2O_3$ laser has a ring cavity with an optical isolator just outside to maintain single-mode, single-frequency operation. The ring laser is tuned continuously in wavelength by a birefringent etalon located inside the cavity. The cw output power of the ring laser is typically in the range of 0.2 to 1.0 W, again depending on the ion-laser pump power.

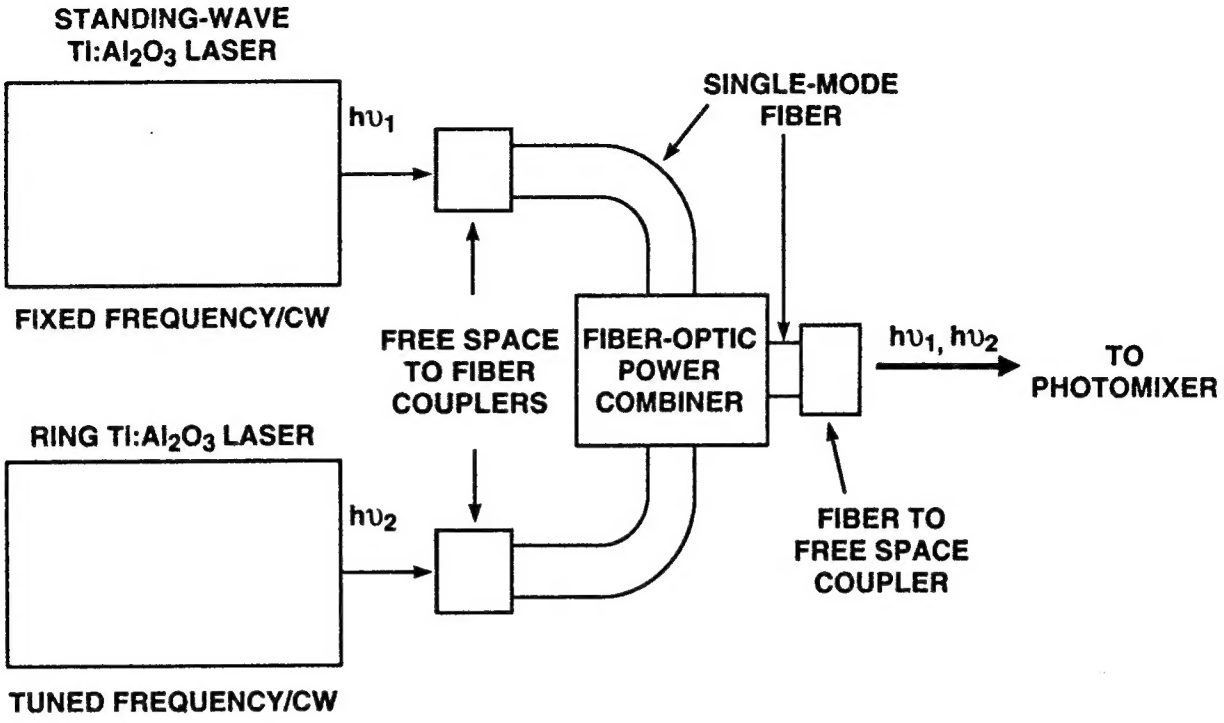


Fig. 3. Experimental configuration for optically pumping the photomixer.

One of the attractive features of photomixing is that the delicate task of beam combining can now be carried out using fiber-optic components. As shown in Fig. 3, this is done by first transforming the output beams of the Ti:$Al_2O_3$ lasers into single-mode fiber using free-space-to-fiber couplers. The two single-mode fibers are connected to a broadband fiber-optic power Although the combiner is somewhat inefficient (only about 25% of the total input power gets into the output fiber), it is quite rugged and vibration insensitive compared to any free-space combining technique. After combining, the beams are transformed back into free space and focused on the photomixer active region.

### *3.1.5. Photomixer Fabrication*

To obtain a photomixer having a sufficiently low capacitance to operate at terahertz frequencies, we have implemented the interdigitated contact structure shown in the inset of Fig. 4. The interdigitated electrodes are fabricated on the top surface of the LTG GaAs by the following steps. First, electron-beam lithography is used to open up channels having the dimension of the desired electrodes in a thin layer of polymethylmethacrylate (PMMA). Then thin layers of titanium and gold are deposited on the entire pattern. Finally, the metal over the

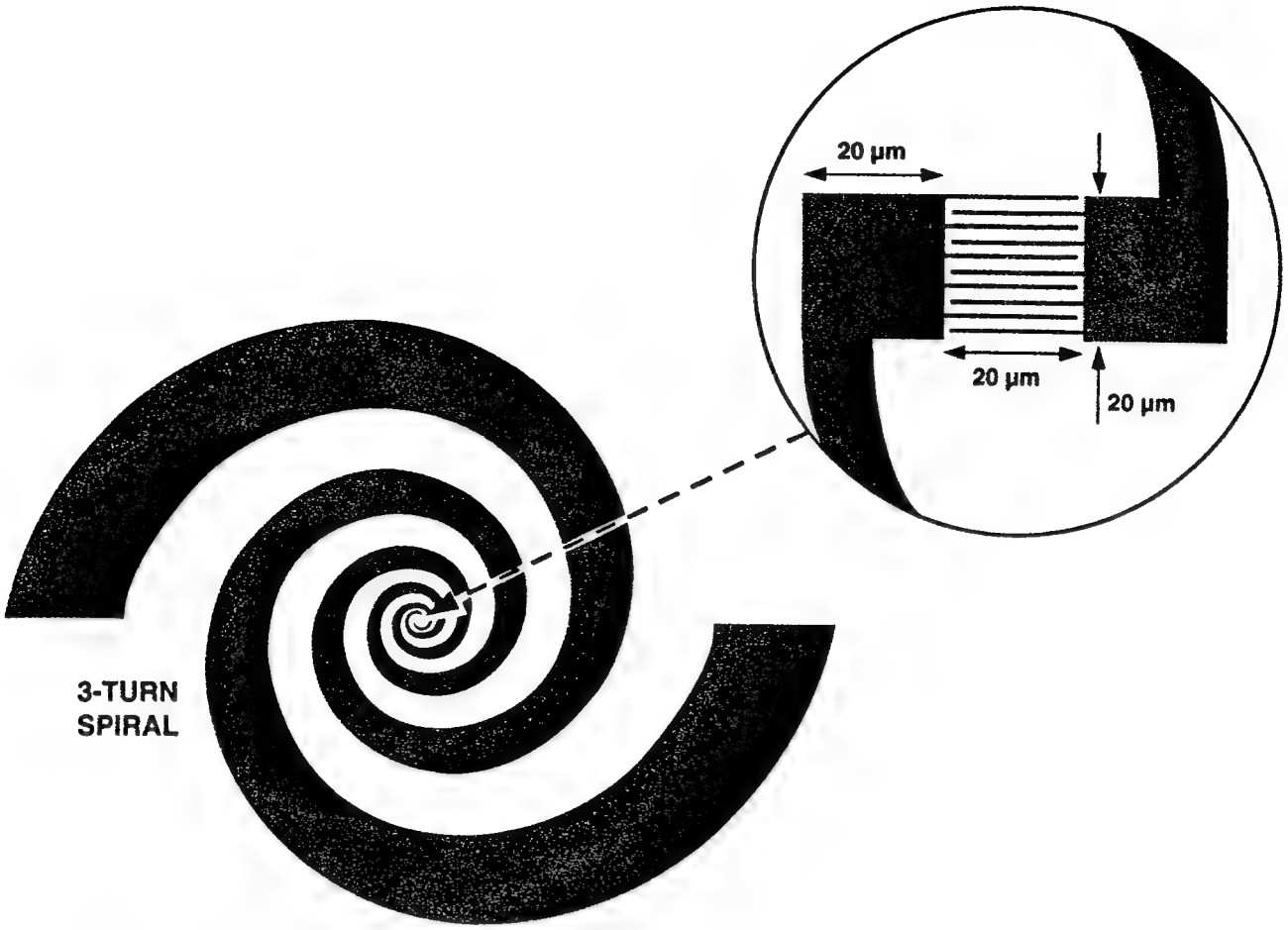


Fig. 4. LTG-GaAs photomixer coupled to broadband self-complementary spiral antenna.

grid of remaining PMMA is lifted off using a chemical solvent. The width of the electrodes is typically 0.2 μm and the gap between electrodes ranges between typically 0.4 and 1.8 μm.

In operation, the laser beams are focused on the interdigitated-electrode region, generating electron-hole pairs in the LTG-GaAs gaps between the electrodes. The density of electrons and holes varies in time at the difference frequency between the two lasers. Because of the large dc-bias field applied between electrodes, the photocarriers drift to opposite contacts. This constitutes a time varying photocurrent that can generate power by driving the characteristic impedance of a transmission line or the radiation resistance of an antenna. We used a 50-Ω coplanar waveguide as the transmission line for frequencies from 0.2 to 50 GHz, as described in Appendix B. For higher frequencies, we coupled the interdigitated-electrode structure to a self-complementary spiral antenna as shown in Fig. 4. The spiral is a type of broadband antenna whose useful range can easily exceed 1 decade of frequency. When lying on a GaAs half-space, its radiation resistance is approximately 72 Ω. The low frequencies radiate from the outer extent of the spiral, and the high ones radiate from the inner extent. At all frequencies most of the radiation goes into the GaAs substrate because of its high dielectric constant. The radiation is

transformed into free space without significant total-internal reflection by abutting the substrate to a silicon hyper-hemispherical lens. The radiation coming out of the lens forms a diverging Gaussian beam which is easily coupled into other millimeter-wave components and systems.

### *3.1.6. Radio-Frequency Photomixing*

To make accurate measurements of the output power and O-E conversion efficiency, CPW photomixers having 20×20 μm active area were driven by a single (standing wave) Ti:$Al_2O_3$ solid-state laser operating near 750 nm. The standing wave laser was internally adjusted by etalons to operate with nearly equal output power in two adjacent longitudinal modes separated in frequency by 200 MHz. The output beam was focused down to a spot diameter of approximately 20 μm at the interface of the photomixer and the total power was varied incrementally by changing the power of the argon-ion laser that pumped the Ti:$Al_2O_3$ crystal. For each pump power, the dc bias voltage was increased from zero up to a value just below that which rendered electrical destruction. The electrical output of the photomixer was measured with a spectrum analyzer.

Described in Appendix C and shown in Fig. 5(a) are the experimental results for a 0.6-μm-gap photomixer at room temperature and for total optical pump powers of 45 and 75 mW. At both power levels, we observed a nearly quadratic increase in output power with dc bias voltage up to about 8 V, followed by a super-quadratic increase at higher voltages. At a fixed bias voltage less than about 5 V, the output power also increased nearly quadratically with pump power between 45 and 75 mW. Both quadratic functions are characteristic of any photomixer in which the photocurrent is ohmic. The super-quadratic dependence on bias voltage is believed to be caused by space-charge effects in the LTG-GaAs material. For 45-mW pump power, the output power at room temperature approaches a maximum value of -9 dBm at a bias voltage of 30 V. This represents an O-E conversion efficiency of approximately 0.3%. When the optical power or bias voltage was increased beyond this level, the device displayed burn-out.

With thermal burn-out in mind, we tested a 0.6-μm-gap photomixer at 77 K by mounting the coplanar-waveguide sample on the cold finger of a liquid-nitrogen cryostat. The laser pump beam was focused on the photomixer through a glass window on the outer vacuum jacket of the cryostat. Shown in Fig. 5(b) are the experimental results for optical pump powers of 75 and 225 mW. For 75 mW pump and bias voltages less than 10 V, the output power was slightly less than at room temperature and the same pump power. Above 10 V bias, the output power at 77 K exceeded that at room temperature as the dependence on bias voltage became super-quadratic. For 225 mW pump power, the output power was nearly ten times that obtained with 75 mW, consistent with the quadratic theoretical dependence of output power on pump power. At biases above about 10 V, the output power increases in a nearly quartic fashion such that +6 dBm (4

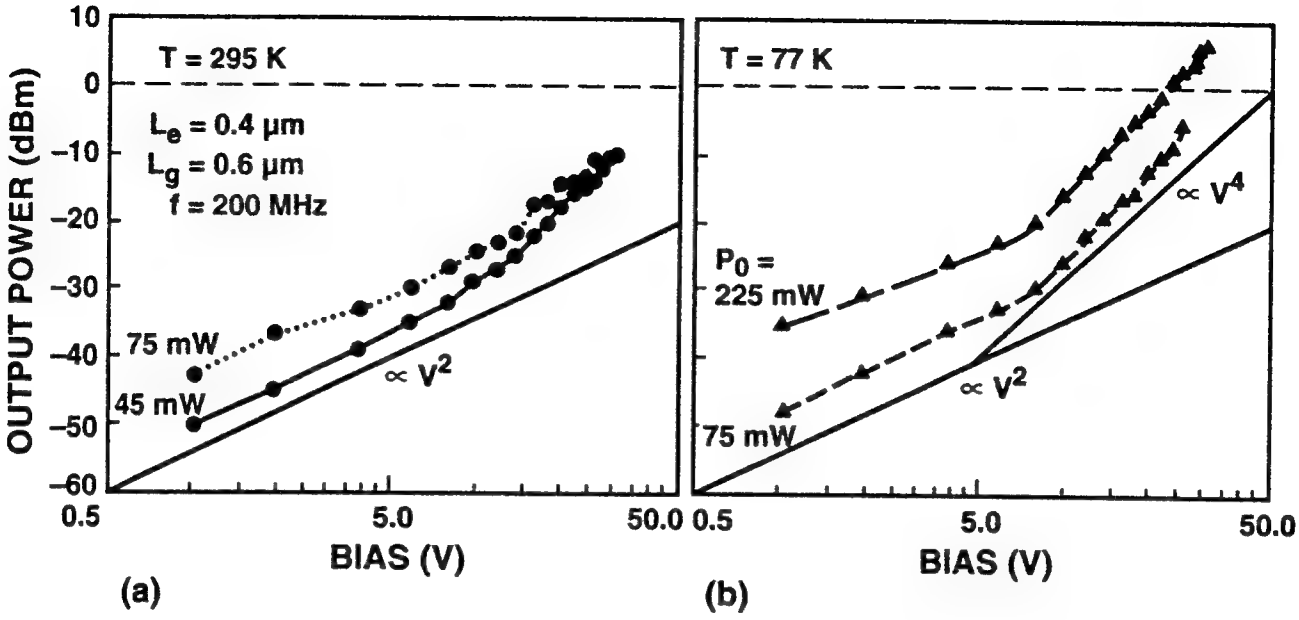


Fig. 5. Output power from 0.6-micron-gap LTG-GaAs photomixer at 0.2 GHz.

mW) was obtained at 30-V bias. The highest O-E conversion efficiency at 77 K was 1.5% under the conditions of 225 mW pump power and 30-V bias. Further details on this interesting results are found in Appendix C.

Other size photomixers were studied at a 200-MHz difference frequency, as discussed fully in the manuscript of Appendix C entitled "Milliwatt output levels and superquadratic bias dependence in a low-temperature-grown GaAs photomixer."

### *3.1.7. Terahertz Photomixing*

At frequencies above 100 GHz, spiral-antenna photomixers were used because of their ability to radiate into free space and because of the relative ease in measuring the output characteristics quasioptically at these frequencies. These results were first reported in the manuscript of Appendix D. Plotted in Fig. 6 is the output power of a 1.8-μm-gap photomixer up to 3.8 THz. For a total pump power of 50 mW distributed equally between the two lasers and a bias voltage of 25 V between electrodes, we measured an output power of approximately 0.035 mW for the CPW structure at frequencies up to about 20 GHz. The data point in Fig. 6 at 10 GHz is scaled up by the factor 72/50 to indicate what would be measured by a 72-Ω load (i.e.,

the antenna resistance). This is valid when the photomixer differential resistance is much higher than the load resistance, as is true under the present, rather modest, optical-pumping conditions. We see that the spiral-antenna output is nearly constant out to about 300 GHz and is down 3 dB at 405 GHz. This bandwidth is consistent with the two-time-constant expression

$$P = \frac{P_0}{[1+(\omega\tau_{eh})^2][1+(\omega R_A C)^2]}$$

where $P_0$ is the reference output power at 10 GHz. Substituting in the time constants $\tau_{eh}$ = 0.27 ps and $R_A C$ = 0.21 ps yields a 3-dB rolloff frequency of 425 GHz, in good agreement with the experiment. At frequencies above 500 GHz the power rolls off monotonically at a rate slightly over 12 dB/octave - the limiting behavior of Eq. (2). This is gradual compared to the roll off of fundamental-frequency electronic oscillators, which made it possible to measure the output power of the present photomixer to 3.8 THz.

The local peak near 800 GHz is thought to represent a transition from spiral radiation to dipole radiation by the interconnect metal between the interdigitated electrodes and the inner radius of the spiral. This is consistent with polarization measurements which indicated that the output radiation was circularly polarized at the lower frequencies, elliptically polarized near 800 GHz, and linearly polarized at the highest frequencies. It is also consistent with the resonant length of the interconnect. Taking the 60-μm length of the interconnect as the physical length of a dipole, we estimate that a half-wave resonance should occur at a frequency of 950 GHz, in fair agreement with the experiment. Between this point and the full-wave resonance, we expect the interconnect to continue radiating because the real part of the radiation impedance should increase somewhat with frequency. This counteracts the expected decrease in radiated power with frequency that arises from the increase of the metallic surface impedance due to the skin effect.

The output power up to 300 GHz represents an optical-to-electrical (O-E) conversion efficiency of approximately 0.1%. This is substantially less than the >1% value reported previously at low frequencies. One reason for this is that the optical pump power was limited to 50 mW total because of insertion loss in the fiber-optic combiner. A second reason is that the bias voltage was limited to values about three-times less than expected. This was caused by breakdown either in the Si-GaAs substrate below the 1.0-μm LTG-GaAs layer or in the gaps between the ends of the electrodes and the opposite contact pad, whose sub-micron dimension was inadvertently made too small. Since the output power (O-E efficiency) goes as the square (linear) of the total pump power and at least as the square (linear) of the bias voltage, we have good reason to believe that the implementation of a lower-loss fiber-optic combiner, better

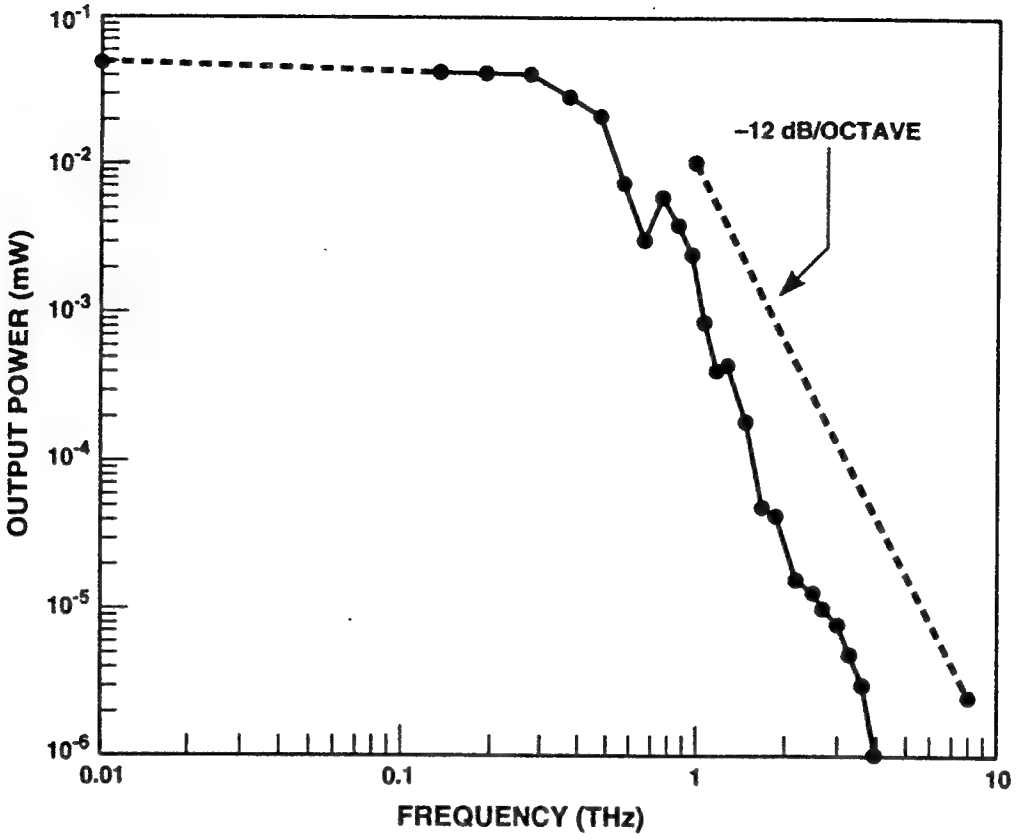


Fig. 6. Output power from 1.8-micron-gap LTG-GaAs photomixer up to 3.8 THz.

electrode definition, or thicker LTG-GaAs layers will yield substantially higher terahertz output power and conversion efficiency in future photomixers.

To test the dependence of bandwidth on electrode separation, we also measured a 0.3-μm-gap photomixer connected to a three-turn spiral antenna. Relative to the 100-GHz output power, the measured 3-dB frequency for this photomixer was 240 GHz. This is an upper limit on the actual bandwidth since the output power was already dropping at more than 4 dB/octave at 100 GHz. By 500 GHz the output power was down 14 dB relative to 100 GHz compared to only 4 dB down for the 1.8 μm-gap device. The results are consistent with the expected increase in device capacitance from 2.9 to 22.4 fF as calculated from a theoretical expression, which decreases the $R_AC$-limited 3-dB bandwidth to 99 GHz. In addition, these results also prove unequivocally that the LTG-GaAs photomixers are not transit-time limited devices as the present interdigitated electrode structures would likely be on standard epitaxial GaAs (i.e., GaAs grown at high temperatures). In the transit-time-limited case, the observed bandwidth would *increase* significantly with the given reduction in gap width, contrary to what was observed here.

## 3.2. RTD RELAXATION OSCILLATOR

### *3.2.1. Principles of Operation*

The RTD relaxation oscillator is based on the repetitive switching through the NDR region between dc-stable points lying below the peak point and above the valley point. To establish this type of oscillation, we imagine that the RTD is connected to one end of a short-circuited transmission line, as shown in Fig. 7. The transmission line has quiescent operation point is initially just below the peak or just above the valley, and the RTD is induced to switch toward the valley or peak, respectively, by a shift in the bias voltage $V_B$. Once the first switch occurs, a pulse travels down the line, is reflected from the short with inverted polarity, and arrives back at the RTD after a time $2t_d$. If $2t_d$ is sufficiently greater than the RTD switching time $t_s$, then the return pulse will induce the RTD to switch back to the initial operating point. The subsequent return pulse then induces a switch similar to the first one, and the process repeats at a rate of $(4\ t_d)^{-1}$. The overall process is classified as a relaxation oscillation because the RTD dwells in either of its PDR regions between switching events. Further conceptual details can be found in Appendix E.

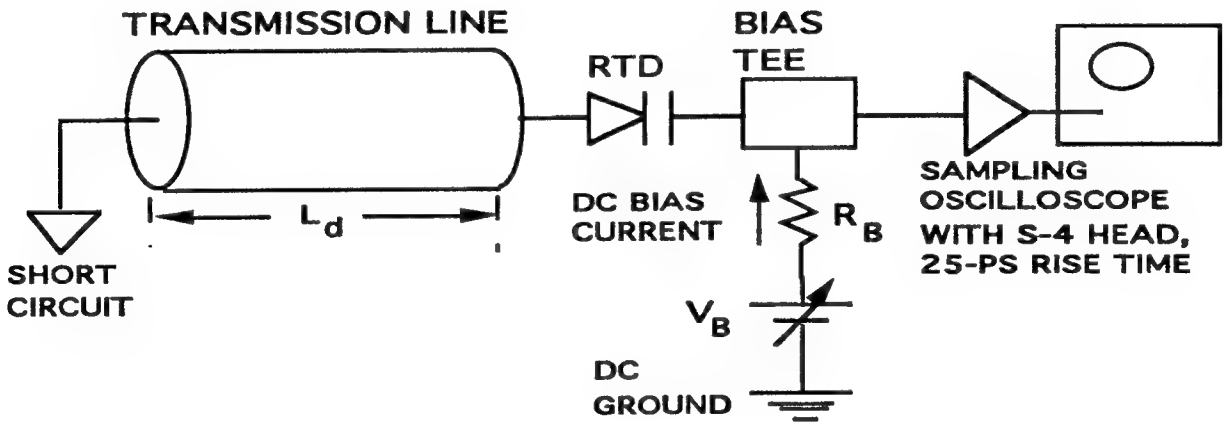


Fig. 7. Schematic diagram of the resonant-tunneling transmission-line relaxation oscillator.

### *3.2.2. Numerical Modeling*

To demonstrate the operational characteristics of the relaxation oscillator, we have simulated it numerically using the program SPICE3E. The transmission line is represented by the standard SPICE3 model, which is lossless and dispersionless. The RTD is represented by the parallel combination of a nonlinear voltage-controlled current generator and a nonlinear capacitance. The voltage dependence of the current generator is designed to be an accurate physical

representation of the RTD, taking advantage of the transcendental functions available in SPICE3E. The current-voltage (I-V) characteristic of the RTD is assumed to have the form

$$I = c_1 V [ \tan^{-1} ( c_2 V + c_3 ) - \tan^{-1} ( c_2 V + c_4 )] + c_5 V^m + c_6 V^n$$

where the constants $c_1$ through $c_4$ are determined by the turn-on voltage, peak voltage, peak current, and peak differential conductance of the RTD, and the constants $c_5$ and $c_6$ are determined, after obtaining $c_1$ through $c_4$, by fitting to the valley current and one arbitrary point beyond the valley. The exponents m and n ($n > m$) are chosen to obtain a satisfactory fit to the overall I-V curve beyond the valley point. A good fit for high-quality RTDs is obtained with $m = 3$ and $n = 9$. The two $\tan^{-1}$ terms occur in the stationary-state tunneling theory of the RTD, with a Lorentzian form used for the transmission probability and a degenerate electron population assumed on the cathode side of the resonant-tunneling structure. The two polynomial terms account for the excess current, which is the primary current component beyond the valley point. The capacitance of the RTD is represented by the SPICE model for a back-biased junction diode, $C = C_0 [ 1 + V / V_J ]^{-1/2}$, where $C_0$ is the zero-bias capacitance and $V_J$ is the built-in potential. The diode reverse saturation current is made negligibly small.

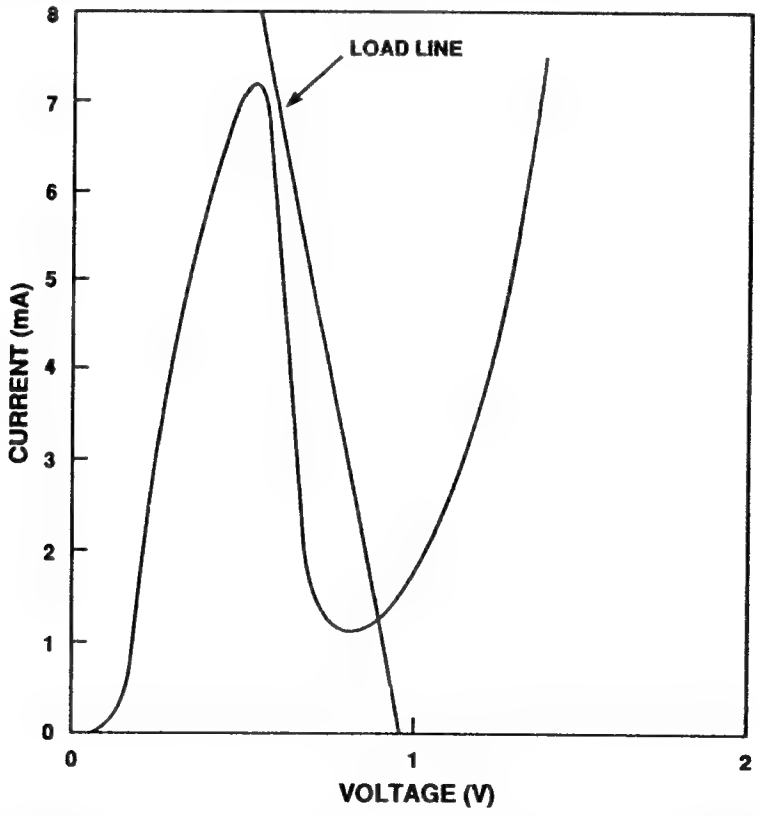


Fig. 8. Current-voltage characteristic of RTD modeled as relaxation oscillator. The straight line shows the dc load line presented to the RTD after the application of the start-up ramp.

Shown in Fig. 8 is the I-V curve simulated here. It applies to a 4-$\mu m^2$ RTD having a peak current density of $1.8 \times 10^5$ A–$cm^{-2}$ and a specific capacitance at the peak of 1.4 fF $\mu m^{-2}$. The model I-V curve has the parameters $c_1 = 0.0052$, $c_2 = 24.5$, $c_3 = 5.0$, $c_4 = 15.0$, $c_5 = 0.0000809$, $c_6 = 0.0014$, $m = 1$, and $n = 5$. The resulting peak-to-valley current ratio (PVCR) is 6.3, equal to the highest room-temperature PVCR obtained with GaAs/AlGaAs RTDs. The capacitance parameters are $C_0 = 14.0$ fF and $V_J = 0.1$ V, yielding $C = 5.5$ fF at the peak voltage.

The output voltage waveform across the load resistance is shown in Fig. 9 for a transmission line having an electrical delay of 3.0 ps. It is apparent that the waveform is highly non-sinusoidal. It consists of a sequence of pulses having a full width at half-maximum of 1.9 ps and a repetition time of approximately $4t_d$. During the repetition period two pulses occur having opposite polarities. These pulses represent the two switching events required to complete one cycle around the dynamic load line of the RTD. For both polarities, the pulse width is somewhat greater than the 10-90% switching time $t_R$ of the RTD between the peak and valley points. An analytic expression for $t_R$ was derived in the previous phase of this project, $t_R = 4.4\Delta VC/\Delta I$, where $\Delta V$ is the difference between the valley and peak voltages, C is the capacitance at the peak point, and $\Delta I$ is the difference between the peak and valley currents. For the simulated RTD, we have $\Delta V = 0.28$ V, $\Delta I = 6.0$ mA, and $C = 5.5$ fF, so that $t_R = 1.1$ ps. The difference between $t_R$ and the generator pulse width is caused by the fact that the generator switches over a wider voltage range between the peak and a point approximately 0.4 V beyond the valley. Other simulated waveforms can be found in Appendix E.

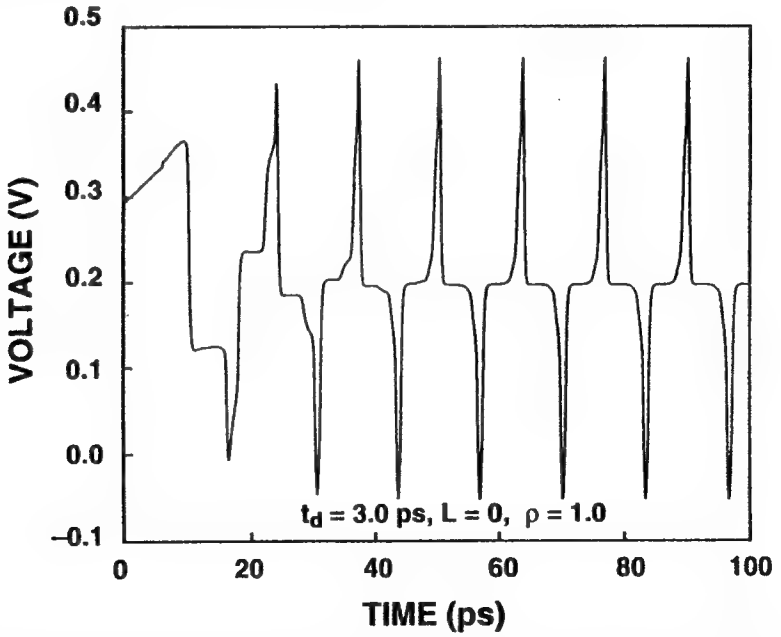


Fig. 9. Simulated output waveform of RTD relaxation oscillator connected to transmission line having an electrical delay of 3.0 ps.

### *3.2.3. Microwave Experiments*

The relaxation oscillations were measured in the time domain using the set up shown in Fig. 7. The bias voltage used to induce and maintain the oscillation was coupled to the RTD through a broadband bias tee. The high-frequency output port of the tee was coupled to a sampling oscilloscope having an input risetime of 25 ps.

Shown in Fig. 10 is the output waveform of a typical hybrid RTD relaxation oscillator demonstrated during this program. The repetition rate is approximately 150 MHz. As predicted in the numerical simulations, pulses of both polarities appear at the output. The positive-going amplitude is 0.45 V, and the negative-going amplitude is 0.25 V. The pulse width at the 3-dB-down point of both pulses is roughly 25 ps. This is limited mostly by the risetime of the S-4 sampling head used in these experiments. The highest-frequency repetition rate obtained with the relaxation oscillator was about 3 GHz. In this case, the amplitude was also about 0.5 V and the pulse width was about 25 ps. However, the oscillating waveform looked quasi-sinusoidal rather than impulsive.

For many applications, the presence of pulses of both polarities is detrimental. Two examples are the use of the RTD relaxation oscillator to drive p-n junction heterojunction diode lasers and its use as an on-chip clock in very high-speed (e.g., ECL) bipolar logic circuits. In both cases, one of the pulses is either useless or detrimental.

To eliminate the pulse of one polarity, we investigated the combination of an RTD relaxation oscillator and a series Schottky diode biased near the "knee" of its I-V characteristic. The schematic diagram is shown in Fig. 11. As connected, the series-mounted Schottky diode prevents the passage of positive-going pulses because they are blocked by the reverse bias applied to the diode. Negative-going pulses are passed very readily providing that the series resistance of the Schottky diode is sufficiently low.

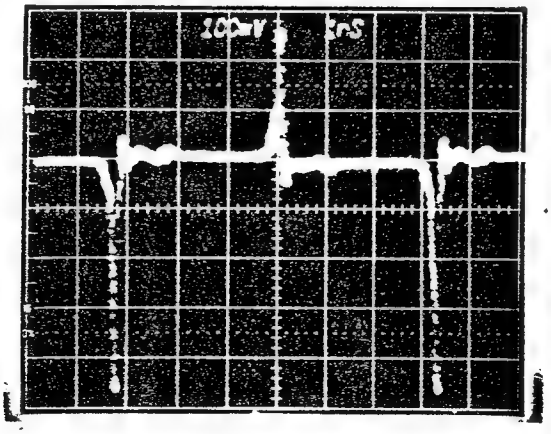

Fig. 10. Experimental relaxation oscillator waveform from hybrid-packaged RTD and transmission line.

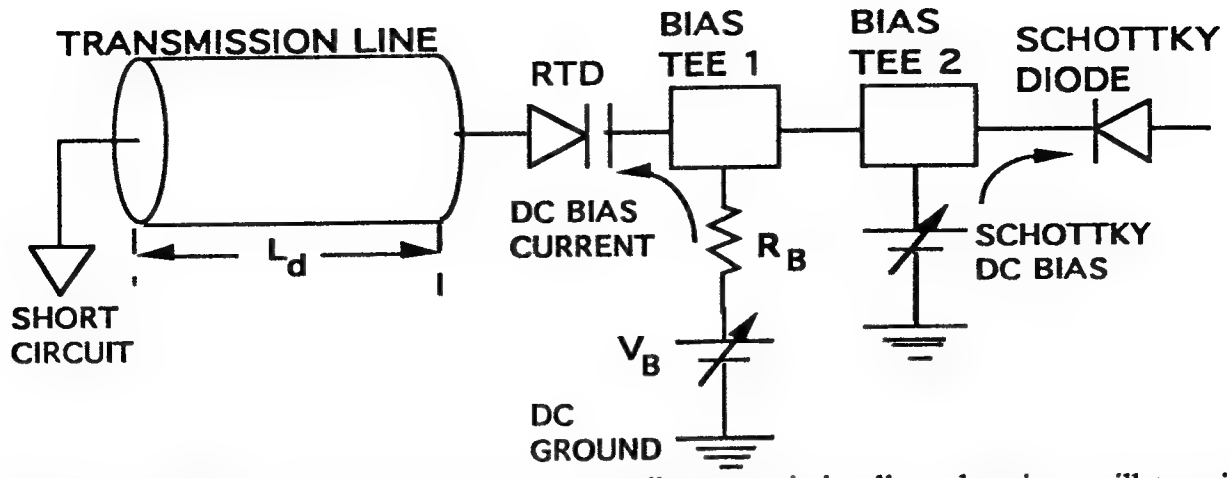


Fig. 11. Schematic diagram of the resonant-tunneling transmission-line relaxation oscillator with external Schottky diode to clip the pulse of one polarity.

Fig. 12 shows an example of the impulse generation achieved with the Schottky-diode loaded RTD relaxation oscillator. The RTD used in this case had three graded quantum wells in order to achieve a wide NDR region in voltage space. Such devices were conceived in the previous phase of this program and are discussed further in Appendix F. The resulting impulse waveform had a negative-going amplitude of approximately 1.2 V and a full width at the 3-dB points of approximately 400 ps. This pulse width is thought to be limited by the risetime limit of the graded-quantum-well RTD. Single-well RTDs showed much narrower pulse width, comparable to the those shown in Fig. 12, but suffered from reduced amplitude.

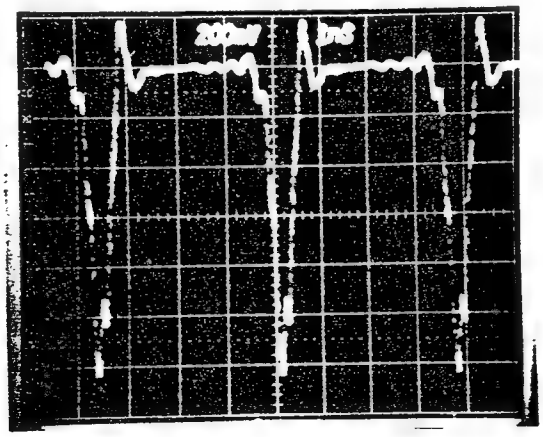

Fig. 12. Experimental clipped pulse train of RTD/transmission-line relaxation oscillator.

### *3.2.4. Monolithic Circuit Fabrication*

The monolithic version of the relaxation oscillator was pursued in large part by a graduate student, Mr. Christopher L. Dennis, as part of his Master's Thesis in Electrical Engineering. The topology of the monolithic RTD and requisite transmission line is shown in Fig. 13. The overall design criteria were presented at the 1993 ISDRS Meeting in Charlottesville, VA, summarized by Appendix G. The RTD is connected in series with the center conductor of a coplanar waveguide (CPW). One end of the CPW is short circuited and the other end (not shown in Fig. 13) makes an abrupt transition to a high-frequency output circuit through a coplanar launching pad. Because the RTD is mesa isolated (see below for more discussion of fabrication), both the center and ground conductor of the CPW abruptly drop in height from a level at the top of the RTD mesa (output side) to a level at the bottom of the RTD mesa (short-circuit side).

The dimensions of the CPW and coplanar pad were chosen to achieve a 50-Ω characteristic impedance. In the RTD and short-circuit section of the structure, the width of the center conductor was nominally 15 μm and the width of the gaps was 11 μm. In the coplanar pad section, the width of the center conductor was nominally 30 μm and the width of the gaps was 21 μm. At the point of transition from the CPW to the launch pad, a longitudinal gap

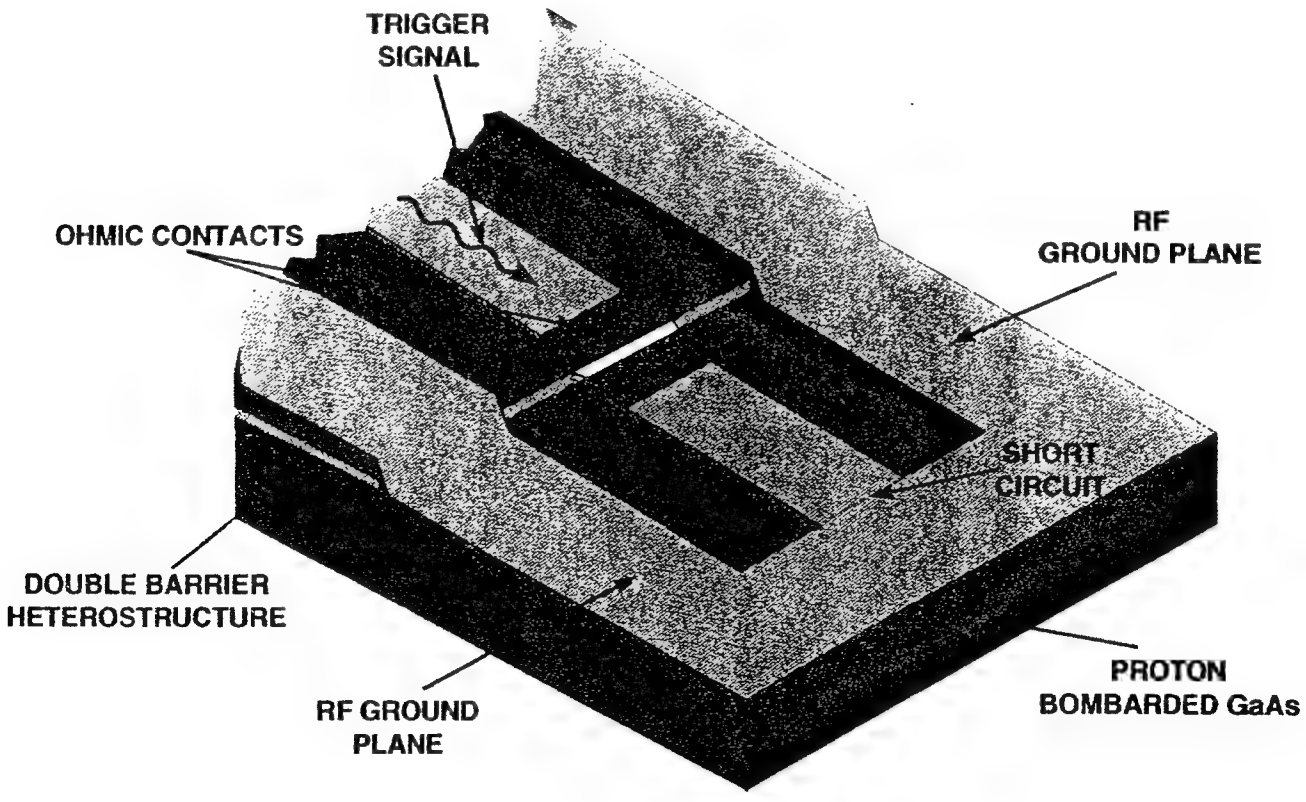


Fig. 13. Topology of monolithic version of RTD/transmission relaxation oscillator.

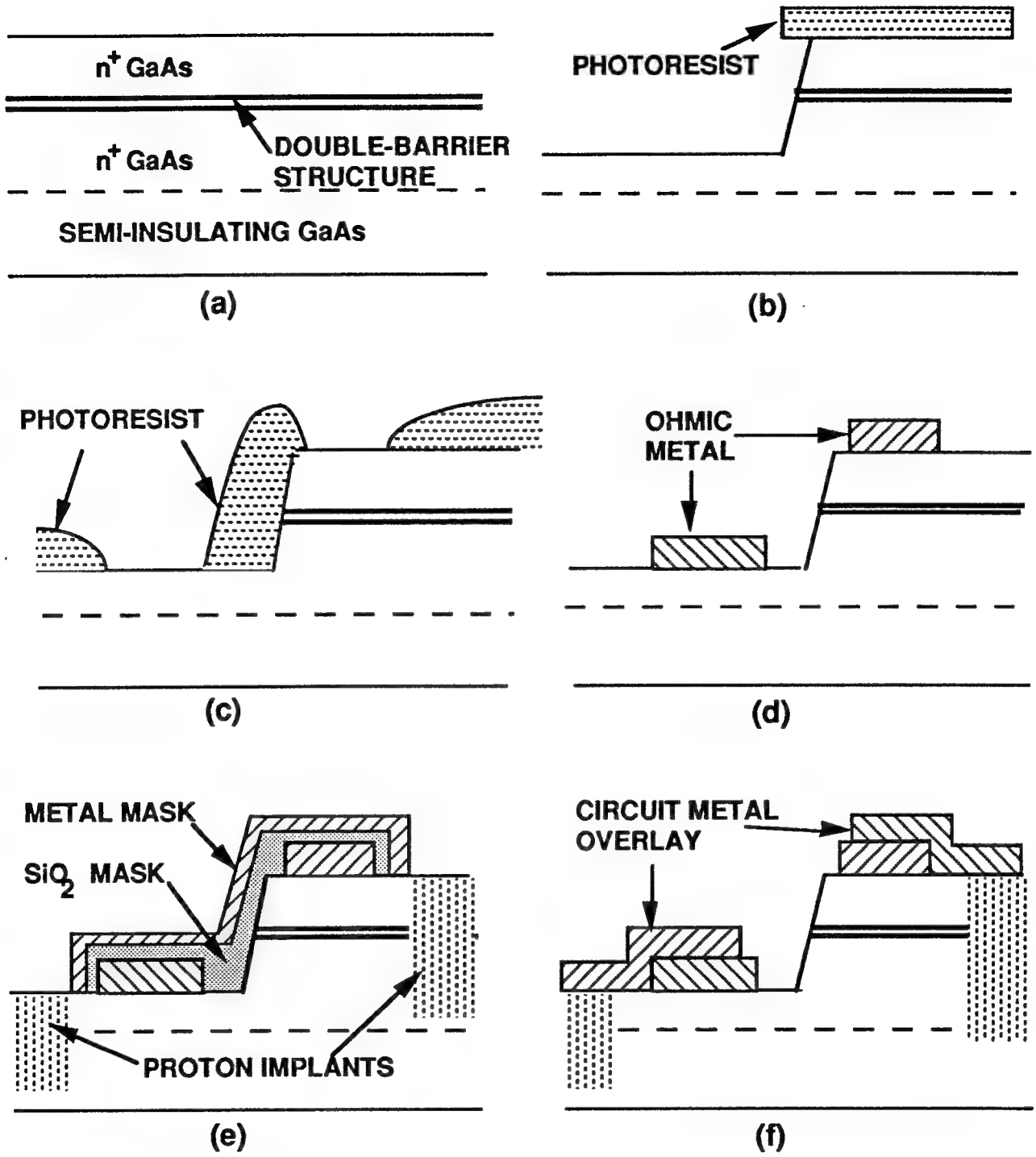


Fig. 14. Fabrication sequence for monolithic RTD/transmission-line relaxation oscillator.

occurred between the center conductors that was 5-μm long. The overall width of the structure (i.e., the separation between the outer edges of the ground conductors of the CPW) was 450 μm, which allowed microwave probing with commercial (i.e., Cascade) probes. The overall length was varied to achieve three different pulse repetition rates. For 5-GHz repetition rate, the RTD-

to-short-circuit length was 5644 μm. For 20- and 100-GHz repetition rate, this length was 1411 and 282 μm, respectively.

The fabrication sequence of the monolithic RTD relaxation oscillator is outlined in Fig. 14. The first step was to grow the RTD epitaxial layers on a semi-insulating GaAs substrate. This was done by molecular-beam epitaxy at a growth temperature of 600°C. The second step, shown in Fig. 14(b), defines the mesa structure. First, a stripe is patterned in positive photoresist by optical lithography. Then PA-11 is used to wet etch through one side of the active region of the RTD using the photoresist as a mask. The etch depth was nominally 1 μm.

The third step, shown in Fig. 14(c), defines the form of the top and bottom ohmic contacts of the RTD. This step was carried out by patterning positive photoresist with a 1.5x30 micron rectangular hole over the top of the RTD mesa and a 3x30 micron hole over the bottom. In the next step of Fig. 14(d), a metallization consisting of 30/40/340 Ni/Ge/Au was deposited over the entire structure by evaporation. Then the photoresist was dissolved, lifting off the metal everywhere except in the rectangular holes.

The fifth step, shown in Fig. 14(e), involved proton bombardment to insulate the GaAs material everywhere except in the current path between the RTD and the bottom ohmic pad. During this step, the active area of the RTD had to be masked off very carefully to avoid damage. The final step entailed the photolithography, deposition, and lift-off of interconnect metal that formed the CPW structure and coupled this structure to the top and bottom ohmic contacts.

One fabrication run was completed with the process outlined above. The fabrication was completed on an RTD having the epitaxial structure shown in Table I. The barriers have an aluminum fraction of 70%, which was found in previous experience to yield very good peak-to-valley current ratio (>4) at intermediate peak current density ($J_P \approx 10^4$ A cm$^{-2}$).

Table I. Material characteristics of RTD structure

| Material | Thickness (nm) | Doping Concentration |
|---|---|---|
| GaAs | 500 | $5\times10^{18}$ cm$^{-3}$ |
| GaAs | 100 | $5\times10^{18}$ cm$^{-3}$ |
| GaAs | 10 | undoped |
| $Al_{0.7}Ga_{0.3}As$ | 2.0 | undoped |
| GaAs | 4.8 | undoped |
| $Al_{0.7}Ga_{0.3}As$ | 2.0 | undoped |
| GaAs | 10 | undoped |
| GaAs | 100 | $5\times10^{18}$ cm$^{-3}$ |
| GaAs | 500 | $5\times10^{18}$ cm$^{-3}$ |
| GaAs | substrate | undoped |

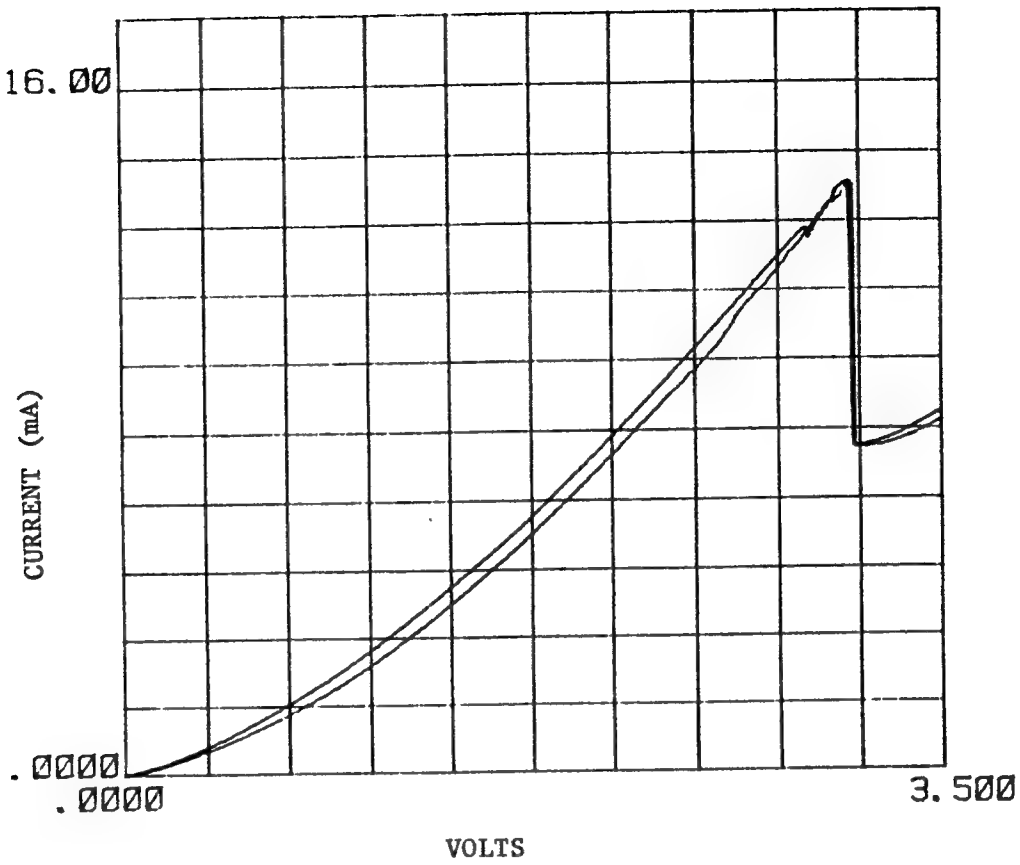


Fig. 15. Experimental I-V curve of RTD in monolithic RTD/transmission-line chip.

### *3.2.5. Monolithic Circuit Testing*

Unfortunately, the project did not run long enough to achieve good results with the monolithic RTD relaxation oscillator. Only one wafer was fabricated, which yielded RTDs having the I-V characteristics shown in Fig. 15. Although the peak current of the device was close to the expectation, the PVCR was only about 2. We believe that this was the result of poor surface morphology in the MBE growth. Consequently, none of the relaxation oscillators worked as designed, although various types of oscillations were observed on external circuitry. For example, by connecting the relaxation oscillator chip to an external bias tee and length of coaxial line, a pulse train was generated having a repetition rate of 294 MHz and an amplitude of 0.1 V.

## 4. REVIEW ARTICLES

During the course of this program, one review article was completed entitled "High-Speed Resonant-Tunneling Diodes." It appears in this report at Appendix H. This article concentrated on the device physics, particularly the high-frequency effects, in RTDs.

## 5. PROFESSIONAL PERSONNEL

During this program, the following personnel were involved to some degree in the research:

| Name | Contribution |
|---|---|
| E. R. Brown | LTG-GaAs photomixer design and testing; RTD relaxation oscillator design and testing |
| F. W. Smith | LTG GaAs growth by MBE |
| A. R. Calawa | RTD growth by MBE |
| M. J. Manfra | MBE support |
| K. B. Nichols | LTG GaAs and MBE growth |
| C. D. Parker | RTD testing |
| K. A. McIntosh | LTG-GaAs photomixer testing |
| L. J. Mahoney | Photomixer and RTD fabrication |
| K. M. Molvar | Photomixer and RTD fabrication |

In addition, a Northeastern student, Christopher L. Dennis, carried out the research for a Master's thesis, entitled "Resonant-Tunneling Transmission Lines," between the period September 1993 and June 1994. In June 1994 he was awarded an MIT Master of Science for this work.

## 6.. INTERACTIONS

### 6.1. CONFERENCE PAPERS

The following is a list of papers given by the above personnel in the period 1 October 1992 through 30 September 1994 on subjects relevant to this program:


[1] "Quasioptical Techniques for Utilizing Resonant-Tunneling Diodes at Frequencies Approaching 1 THz," 1992 Annual Meeting of the Optical Society of America, Albuquerque, NM, 22 Sept., 1992.

[2] "Resonant tunneling relaxation oscillator", OSA Meeting on Ultrafast Electronics and Optoelectronics, San Francisco, CA, January 1993.

[3] "Coherent microwave generation with low-temperature-grown GaAs photomixers," E. R. Brown, F. W. Smith, K. A. McIntosh, M. J. Manfra, MRS Symposium, San Francisco, CA, April 1993.

[4] "High-Speed Resonant Tunneling," International Workshop on Resonant Tunneling, National Cheng Kung University, Tainan, Taiwan, 26-28 July, 1993 (presentation by Prof. H.C. Lin).

[5] " Resonant tunneling transmission lines," C.L. Dennis, E. R. Brown, and S. Prasad, Proceedings of the 2nd International Semiconductor Device Research Symposium, Charlottesville, VA, December 1993.

[6] "Optical-Heterodyne Generation in Low-Temperature-Grown GaAs Photomixers up to 1.2 THz," SPIE Symposium on Nonlinear Optics for High-Speed Electronics, Los Angeles, CA, 25 Jan. 1994.

[7] "Novel Devices for Terahertz Generation and Radiation," Fifth International Symposium on Space Terahertz Technology, Ann Arbor, MI, 10 May 1994.

## 6.2. UNIVERSITY COLLOQUIA

Several university seminars have been given under the support of this program. All were on the subject of either high-speed resonant-tunneling or the physics and technology of LTG-GaAs photomixers. In each case, the host organization requested that the speaker emphasize specific technical aspects of resonant tunneling.

| Host Institution (Location, Date) | Technical Emphasis |
|---|---|
| Northeastern University (Boston, MA, Oct. 1992) | Device Physics of Resonant Tunneling |
| Columbia University (New York, NY, Dec. 1992) | High-Speed Transport in Quantum-Well Structures |
| University of New Mexico (Albuquerque, NM, May 1993) | Applications of Low-Temperature-grown GaAs |
| University of Massachusetts (Amherst, MA, June 1993) | Novel Quantum-Well Infrared Detectors |
| Rennselaer Polytechnic Institute (Troy, NY, Dec. 1993) | High Speed Resonant Tunneling |
| Duke University (Durham, NC, Feb. 1994) | Novel Terahertz Solid-State Sources |
| Massachusetts Institute of Technology (Cambridge, MA, March 1994) | Photomixing in LTG GaAs up to 3.8 THz |

## 6.3. COLLABORATIONS

Over the course of this program, the following collaborations have been established with organizations outside of MIT and Lincoln Laboratory. They included both industrial collaborations and interactions with other government labs and academic institutions:

**LTG-GaAs photomixers**

| *Organization (Time Period)* | *Technology* | *Collaborator* |
|---|---|---|
| NIST Boulder (1994 -) | LTG-GaAs photomixers for frequency metrology | Dr. Leo Hollberg |
| NIST Gaithersburg (1994 - ) | LTG-GaAs photomixers for molecular spectroscopy | Drs. Rick Suenram and Alan Pine |
| NASA Jet Propulsion Lab (1993 -) | THz solid-state local oscillators | Dr. Verendra Sarohia |

**Resonant tunneling devices**

| *Organization (Time Period)* | *Project* | *Collaborators* |
|---|---|---|
| University of Virginia (1992 - 1994) | Schottky-gated resonant-tunneling transistor | Prof. Bill Peatman |
| Rockwell Science Center (1992 - ) | Heterostructure-transistor, resonant-tunneling logic | Dr. K.C. Wang and Peter Asbeck |
| Northeastern Univ. (1992 - 1994) | Resonant-tunneling transmission lines | Prof. Sheila Prasad |

# Coherent millimeter-wave generation by heterodyne conversion in low-temperature-grown GaAs photoconductors

E. R. Brown, F. W. Smith, and K. A. McIntosh
*Lincoln Laboratory, Massachusetts Institute of Technology, Lexington, Massachusetts 02173-9108*

(Received 13 February 1992; accepted for publication 21 October 1992)

An analysis has been carried out of optical heterodyne conversion with an interdigitated-electrode photomixer made from low-temperature-grown (LTG) GaAs and pumped by two continuous-wave, frequency-offset pump lasers. The analytic prediction is in excellent agreement with the experimental results obtained recently on a photomixer having 1.0-$\mu$m-wide electrodes and gaps. The analysis predicts that a superior photomixer having 0.2-$\mu$m-wide electrodes and gaps would have a temperature-limited conversion efficiency of 2.0% at a low difference frequency, 1.6% at 94 GHz, and 0.5% at 300 GHz when connected to a broadband 100 Ω load resistance and pumped at $h\nu=2.0$ eV by a total optical power of 50 mW. The predicted 3-dB bandwidth (193 GHz) of this photomixer is limited by both the electron-hole recombination time (0.6 ps) of the LTG-GaAs material and the RC time constant (0.5 ps) of the photomixer circuit.

## I. INTRODUCTION

Since the development of lasers, optical heterodyne conversion (photomixing) has been very useful for coherent detection in many regions of the electromagnetic spectrum. Photomixing was also proposed as a technique for generating coherent radiation in the microwave and millimeter-wave regions,[1] and interest in this technique has been revived recently by the advances in high-speed III–V device technology.[2,3] Of the two applications, coherent generation has been much less useful than coherent detection, because of the lack of a suitable photomixer. Although difference frequencies have been generated up to 61 GHz,[3] the generated power has been severely limited by at least one of several factors, such as low photomixer bandwidth, poor optical power coupling, impedance mismatch between the photomixer element and the load circuit, and degradation of the photomixer properties at high optical pump power. In this paper, we analyze a photomixer that could alleviate all of these limitations and thereby provide milliwatt levels of continuous-wave (cw) power over a very wide operating bandwidth in the millimeter-wave region.

The physical basis for the proposed photomixer is electron–hole pair generation by photon absorption in low-temperature-grown (LTG) GaAs or InGaAs. The LTG GaAs has recently displayed the remarkable photoconductive properties of subpicosecond electron–hole recombination time[4] $\tau$ and high dc breakdown field ($E_B>1\times10^5$ V cm$^{-1}$).[5] In addition, it displays a high photocarrier mobility ($\mu\approx200$ cm$^2$ V$^{-1}$ s$^{-1}$) relative to semiconductors having a comparable recombination time. Together these properties have led to some impressive optoelectronic results, such as the generation of a 600-V-peak pulse having a full width at half-maximum of 2 ps,[5] and the direct detection of intense subpicosecond laser pulses with a responsivity of 0.1 A/W.[6]

## II. LTG-GaAs PHOTOMIXER

The photomixer consists of two sets of interdigitated metal electrodes deposited on the top surface of the LTG material, as in the direct detector of Ref. 6. A cross-sectional view of the electrode configuration is shown in Fig. 1(a). The band bending at the metal-semiconductor junctions is assumed to be small, so that the photocarrier collection process is photoconductive rather than photovoltaic. This is consistent with the experimental results obtained to date on LTG-GaAs detectors. Therefore, the photomixer can be represented electrically by a photoconductance $G_P$ that is a function of the absorbed optical power. Because the essential photoconductive properties of the LTG GaAs—the absorption strength, mobility, and recombination time—are practically independent of the electrode voltage, $G_P$ can be approximated as an ohmic conductance. In the equivalent circuit in Fig. 1(b), $G_P$ is connected in series with a small (contact) resistance $R_S$. Both elements appear in parallel with a capacitance $C$ that is a function of the electrode geometry and the dielectric constant of the photoconductive material. This capacitance can be derived from electrostatic theory.[7] The electrodes are connected to a planar distributed circuit, such as a broadband spiral antenna, or a coplanar waveguide. In both cases, the planar circuit can be represented electrically over a very broad bandwidth by the resistance $R_L$. The electrical bias for the circuit is supplied by the voltage source $V_B$.

For simplicity, we make the following assumptions concerning the interdigitated photomixer: (1) the electrodes are opaque to the incident radiation and (2) the instantaneous optical power absorbed per unit volume and the bias electric field $E_P$ between the electrodes are both uniform in a volume defined laterally by the area of the gaps and vertically to a depth of $L_a$. Thus, $G_P$ can be approximated as

$$G_P\approx ne(\mu_e+\mu_h)N_g(L_eL_a)/w_g, \tag{1}$$

where $n$ is the instantaneous photocarrier pair density throughout the absorption volume, $\mu_e$ and $\mu_h$ are the electron and hole mobilities, respectively, $N_g$ is the number of gaps, $L_e$ is the length of the electrodes, and $w_g$ is the width


© 1993 American Institute of Physics


APPENDIX A

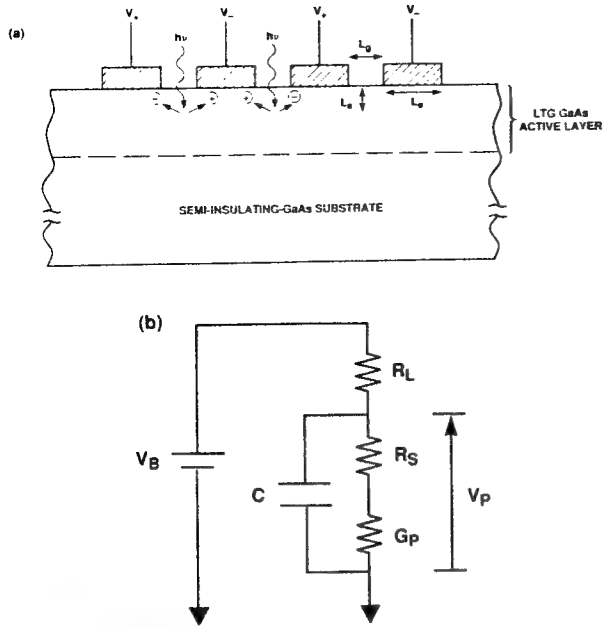


FIG. 1. (a) Interdigitated electrode configuration of photomixer. The bias voltage is applied between adjacent electrodes, such that electrons generated in the gap between them drift toward one electrode and the holes to the other, thus driving a photocurrent in an external circuit. (b) Equivalent circuit of the photomixer and external broadband load circuit.

of the gaps between the electrodes. The photocarrier density is the solution to

$$\frac{dn}{dt}=\frac{\eta_e P_i}{h\nu L_a L_e(N_g w_g+N_e w_e)}-\frac{n}{\tau}, \tag{2}$$

where $\eta_e$ is the external quantum efficiency (number of photocarrier pairs generated per incident photon), $P_i$ is the optical power incident on the detector, $h\nu$ is the photon energy, $w_e$ is the width of the electrodes, $P_i/L_e(N_g w_g+N_e w_e)$ is the incident optical intensity, and $N_e$ is the number of illuminated electrodes. According to the assumptions, we also have the relation

$$\eta_e=\frac{\eta_i t N_g w_g}{N_g w_g+N_e w_e}, \tag{3}$$

where $t$ is the power transmissivity at the top air–GaAs interface and $\eta_i$ is the internal quantum efficiency (number of photocarrier pairs generated per photon entering the photomixer material).

## III. OPTICAL HETERODYNE CONVERSION

The photomixing process occurs by illuminating the interdigitated-electrode region with two single-mode cw laser beams having average powers $P_1$ and $P_2$ and frequencies $\nu_1$ and $\nu_2$, respectively. The instantaneous optical power incident on the photomixer is given by[8]

$$P_i=P_0+2\sqrt{mP_1P_2}[\cos 2\pi(\nu_2-\nu_1)t + \cos 2\pi(\nu_2+\nu_1)t], \tag{4}$$

where $P_0=P_1+P_2$ is the total incident power averaged over a long time period, and $m$ is the mixing efficiency that ranges in value between 0 and 1 depending on the spatial overlap of the two laser beams. In the present analysis, $h\nu_1$ and $h\nu_2$ are greater than the room-temperature GaAs band-gap energy (1.42 eV), but are close enough in magnitude ($\nu_2\approx\nu_1\equiv\nu$) that the difference frequency $f=|\nu_2-\nu_1|$ is in or near the microwave band. In this case, the last term in Eq. (1) varies on a time scale much shorter than $\tau$, and thus does not modulate the photoconductance significantly. By neglecting this term and substituting Eq. (4) into Eq. (2), we obtain the solution

$$n(t)=\frac{\eta_e P_0\tau}{h\nu A L_a}\left(1+\frac{2\sqrt{mP_1P_2}\sin(\omega t+\phi)}{P_0\sqrt{1+\omega^2\tau^2}}\right), \tag{5}$$

where $\omega=2\pi f$, $\phi=\tan^{-1}(1/\omega\tau)$, and $A=L_e(N_e w_e+N_g w_g)$ is the active area. By substituting this expression into Eq. (1) and applying Eq. (3), we obtain the time-dependent conductance

$$G_P\approx\frac{\eta_i t\tau e N_g^2(\mu_e+\mu_h)P_0}{h\nu(N_e w_e+N_g w_g)^2}\left(1+\frac{2\sqrt{mP_1P_2}\sin(\omega t+\phi)}{P_0\sqrt{1+\omega^2\tau^2}}\right) \equiv G_0[1+\beta\sin(\omega t+\phi)]. \tag{6}$$

At low optical power levels $G_0$ is related to the short-circuit external responsivity $S$ by

$$S\approx\frac{G_0 V_B}{P_0}=\frac{\eta_i t\tau e N_g^2(\mu_e+\mu_h)V_B}{h\nu(N_e w_e+N_g w_g)^2}. \tag{7}$$

This expression is useful for relating the intrinsic material properties to the measured responsivity.

The time-dependent conductance modulates the bias current from $V_B$ at frequency $f$ and thus delivers power to $R_L$ at this frequency. This power is found by solving the dynamic current equation for the circuit in Fig. 1(b). From the Kirchoff current law, we write the time-varying voltage $v$ across the photomixer element as the solution to the following differential equation:

$$\frac{dv}{dt}=\frac{V_B-v}{R_L C}-\frac{v}{C[R_S+G_P^{-1}(t)]}. \tag{8}$$

For $G_P$ in the form of Eq. (6), this equation cannot be solved in closed form. However, a useful approximate solution is obtained by assuming that $v$ is harmonic (i.e., $v=D+E\sin\omega t+F\cos\omega t$, where $D$, $E$, and $F$ are constants), by setting $\phi$ to zero, and by neglecting $R_S$. The phase of $v$ can be zero without loss of generality since the phase of the photocarrier density is arbitrary. However, neglecting $R_S$ is valid only if $G_0R_S\ll 1$ and $R_L/R_S\gg 1$. By substituting the harmonic voltage into Eq. (8) and dropping the terms varying with time as $2\omega t$, we find

$$P_\omega=\frac{\frac{1}{2}(V_B G_0\beta)^2 R_L[(1+G_0R_L)^2+(\omega R_L C)^2]}{(1+G_0R_L)^2[(1+G_0R_L)^2+(\omega R_L C)^2-\frac{1}{2}(G_0R_L\beta)^2]^2}. \tag{9}$$

This expression has the following expected properties. First, for fixed $\omega$, $R_L$, and $P_0$, the value of $P_\omega$ is maximized for $m=1$ and $P_1=P_2=P_0/2$. Second, in the small-signal

limit, where $G_0R_L \ll 1$, and under the assumption that $P_\omega$ is maximized as just described, Eq. (9) reduces to

$$P_\omega = \tfrac{1}{2}(V_B G_0)^2 R_L/[1+\omega^2\tau^2][1+(\omega R_L C)^2],$$

which is the result that one would obtain from small-signal photoconductor theory.[8] Third, in the limit of high frequencies, where $\omega\tau \gg 1$ and $\omega R_L C \gg 1$, the above small-signal expression for $P_\omega$ reduces to $\frac{1}{2}V_B^2 G_0^2 R_L/\omega^4(\tau R_L C)^2$. Since the difference-frequency power is dropping at 12 dB/octave in this limit, it is very important for the photomixer to have low $\tau$ and $C$.

A quantity of practical importance is the conversion efficiency, $\epsilon_\omega \equiv P_\omega/P_0$. In the limit $\omega \to 0$, the efficiency $\epsilon_0$ displays a maximum with respect to $P_0$ at $G_0 \cong 0.387/R_L$ and $V_B = V_B^{\max}$, where $V_B^{\max}$ is the maximum voltage that can be applied between adjacent electrodes without electrical breakdown. The resulting maximum conversion efficiency is given by

$$\epsilon_0^{\max} = \frac{0.056(V_B^{\max})^2 \eta_i t \tau e N_g^2(\mu_e+\mu_h)}{h\nu(N_e w_e + N_g w_g)^2}$$

$$\approx \frac{0.056 E_{\max}^2 \eta_i t \tau e(\mu_e+\mu_h)}{h\nu(1+N_e w_e/N_g w_g)^2}, \qquad (10)$$

where $E_{\max}$ is the maximum electric field that the LTG material can withstand in the absence of illumination. An important aspect of Eq. (10) is that in the limit of low contact obscurity (i.e., $w_e/w_g \ll 1.0$), and when $N_e \approx N_g$ (as in a multiple-electrode photomixer), $\epsilon_0^{\max}$ depends only on the intrinsic properties of the LTG material and not on the electrode configuration. Another aspect is that the maximizing value $G_0 = 0.387/R_L$ is substantially smaller than it would be (viz., $G_0 = R_L^{-1}$) in the small-signal limit. This is beneficial for power generation in the millimeter-wave band, where it is difficult to obtain broadband planar antennas or transmission lines having $R_L$ greater than a few hundred ohms.

## IV. COMPARISON WITH EXPERIMENT

We have recently fabricated LTG-GaAs interdigitated photomixers and have measured the output power as a function of pump power with pump photon energies near 1.6 eV and a difference frequency of 200 MHz.[9] The photomixer consisted of ten 1.0-$\mu$m-wide electrodes and nine 1.0 $\mu$m gaps. The electrode length was 20.0 $\mu$m. The 1.0-$\mu$m-thick LTG-GaAs epitaxial layer was grown by molecular-beam epitaxy on a semi-insulating (100) GaAs substrate at a temperature of 195 °C. From previous characterization on material grown under the same conditions, this LTG GaAs is expected to have a $\tau$ of approximately 0.6 ps and an $E_{\max}$ of approximately $5\times10^5$ V cm$^{-1}$. The photomixer was fabricated in the gap of a 50-Ω coplanar waveguide, which was connected to a 50-Ω coaxial transmission line to measure the output power.

Shown in Fig. 2 is the experimental output power at 200 MHz and $V_B = 36$ V for four different pump powers of 25, 50, 100, and 170 mW. The output power increases from $-20.0$ to $-8.4$ dBm as $P_0$ increases from 25 to 170 mW.

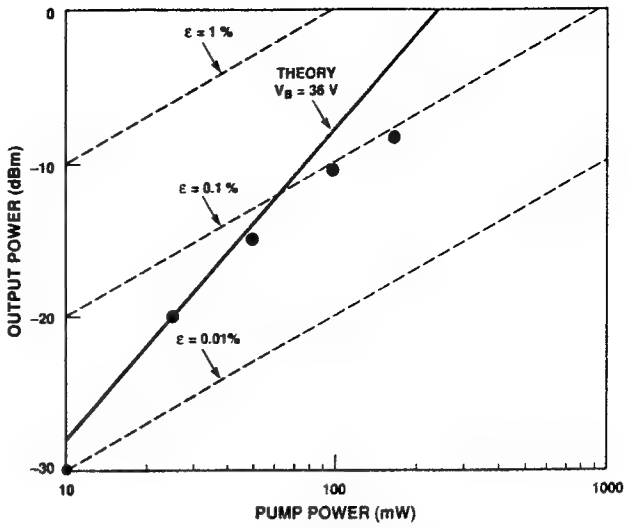


FIG. 2. Comparison of experimental output power (circles) and theoretical prediction (solid line) for a photomixer having ten 1.0-$\mu$m-wide electrodes and nine 1.0-$\mu$m-wide gaps (Ref. 9). The dashed lines represent loci of constant conversion efficiency.

The conversion efficiency increases from 0.040% to 0.085% over the same range. The experimental results are compared to the theoretical curve calculated from Eq. (9) with the parameters $\beta = 1$, $G_0 = SP_0/V_B$, $S = 0.026$ A/W (measured at $V_B = 36$ V), $R_L = 50$ Ω, and $C = 6.1$ fF (calculated from a standard formula[7]). Over the given range the theoretical curve is very nearly quadratic with $P_0$. At the lowest pump power, the theoretical $P_\omega$ is in excellent agreement with the experiment. However, the discrepancy between theory and experiment grows with increasing $P_0$.

When the experimental pump power was increased slightly beyond 170 mW, the photomixer was destroyed because of excessive heating.[9] The increase in device heating with $P_0$ also explains the subquadratic dependence of the photomixer experimental output power. Above room temperature, the photocarrier mobility should decrease with increasing operating temperature because of phonon scattering. We expect that $\eta_i$ and $\tau$ should also vary with temperature, but much more slowly than the mobility. Thus, $G_0$ defined in Eq. (6) will vary sublinearly with $P_0$, leading to a subquadratic dependence of $P_\omega$ on $P_0$ in Eq. (9). This is consistent with the experimental observation that the responsivity decreased with $P_0$ over the range of 25–170 mW. By Eq. (7), the responsivity would be constant if $G_0$ were linear in $P_0$.

A rough estimate of the temperature at the surface of the photomixer is obtained by assuming that the GaAs substrate is semi-infinite and that all of the optical pump power is absorbed in an infinitesimal layer just below the photomixer surface. This leads to a temperature rise at the surface of $\Delta T \approx (P_A + P_E)/2\kappa D$ (Ref. 10), where $P_A$ is the absorbed optical power, $P_E$ is the dissipated electrical power, $\kappa$ is the room-temperature thermal conductivity of GaAs (0.46 W cm$^{-1}$ K$^{-1}$), and $D$ is the width of the active area of the photomixer (assumed to be square). The operating temperature is thus $T_{\rm op} = T_0 + \Delta T$, where $T_0$ is the ambient temperature. With the present assumptions,

we have $P_A = tP_0 N_g w_g/(N_g w_g + N_e w_e)$. At the photon energy of 1.6 eV, $t \approx 0.67$,[11] so that $P_A \approx 0.33 P_0$. For $V_B = 36$ V and $P_0 = 170$ mW, the experimental value of $P_E$ was 104 mW. Thus, at $T_0 = 25$ °C the approximate $T_{op}$ of the given photomixer was 112 °C.

## V. SUBMICRON-GAP PHOTOMIXER

A photomixer having an output power exceeding 1 mW and a conversion efficiency exceeding 1% would be very desirable for millimeter-wave ($f > 30$ GHz) applications. To achieve this level of performance, a photomixer having higher responsivity is required. Of all the photomixer parameters in Eq. (7), the responsivity is most sensitive to the electrode and gap widths. Therefore, we consider the structure studied by Chen *et al.*[6] as a direct detector that had 20 electrodes with $w_e = 0.2$ μm and 19 gaps with $w_g = 0.2$ μm. The electrode length was 6.5 μm. The measured detector parameters at $h\nu = 2.0$ eV and $V_B = 8$ V were $\tau = 0.6$ ps, $t = 0.59$, $\eta_i = 0.68$, and $S = 0.1$ A/W. The electrode capacitance was 4.9 fF. Inserting these parameters into Eqs. (1) and (6), we calculate the photocarrier mobility $\mu_e + \mu_h = 167\ \text{cm}^2\,\text{V}^{-1}\,\text{s}^{-1}$.

Operating as a photomixer, the 0.2-μm-gap structure provides the theoretical performance characteristics shown in Fig. 3. No consideration is given to device heating. In Fig. 3(a), we plot the output power according to Eq. (9) as a function of $P_0$ in the limit $\omega \to 0$ for values of $R_L$ of 50, 100, and 200 Ω. At low values of $P_0$, the photomixer output power increases between $R_L = 50$ and 200 Ω. At high values of $P_0$, this trend reverses for reasons explained by the plots of $\epsilon_0$ vs $P_0$ in Fig. 3(b). For each $R_L$, $\epsilon_0^{\max}$ is 4.6%. However, the pump power required to attain $\epsilon_0^{\max}$, $P_0^{\max}$ varies inversely with $R_L$. This is related to large-signal impedance matching between the photomixer and the load resistance. From the results of Sec. III, we can write $P_0^{\max} = 0.387 V_B/SR_L$. Consequently, within a given set of load resistances, the largest $R_L$ yields the highest conversion efficiency up to the corresponding $P_0^{\max}$. At higher levels of $P_0$, lower values of $R_L$ will yield the highest conversion efficiency and output power.

We include the effect of device heating by constraining the operating temperature to 112 °C, consistent with the estimate derived at the end of Sec. IV. Using the same estimation procedure, we find that the highest total power that can be dissipated in the 0.2-μm-gap photomixer is 57 mW. Using the approximation $P_E \approx SP_0V_B$ and the relation $P_A = 0.33P_0$ (since $w_e = w_g$ for the 0.2-μm-gap photomixer), we find that the highest optical power is 50 mW. As shown in Fig. 3, this optical power yields a temperature-limited output power and conversion efficiency of 0.6 mW and 1.1%, respectively, for $R_L = 50$ Ω; 1.0 mW and 2.0%, respectively, for $R_L = 100$ Ω; and 1.6 mW and 3.2%, respectively, for $R_L = 200$ Ω. In each case the conversion efficiency falls short of the 4.6% maximum because of the temperature constraint.

In Fig. 4 the frequency-dependent conversion efficiency, $\epsilon_\omega$, is plotted for $P_0 = 50$ mW and the same values of $R_L$. For $R_L = 50$ Ω, the 3 dB bandwidth is 235 GHz, which is limited primarily by the effect of $\tau$. For $R_L = 100$ Ω, the 3 dB bandwidth is 193 GHz, which is limited almost equally by $\tau$ and by the time constant $R_L C = 0.5$ ps. For $R_L = 200$ Ω, the bandwidth is 139 GHz, which is limited primarily by $R_L C$. With a bandwidth exceeding 100 GHz, the LTG-GaAs photomixer would be very useful as a millimeter-wave sweep oscillator in diagnostic applications or as a frequency-agile source in millimeter-wave communications systems.

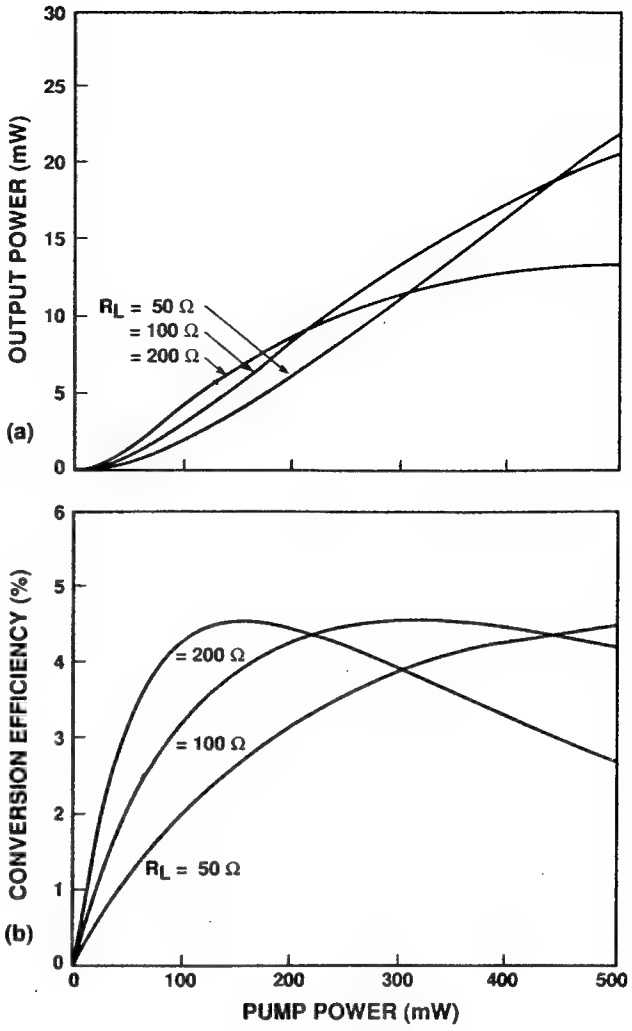


FIG. 3. (a) Calculated photomixer output power versus optical pump power for an interdigitated-electrode configuration having 20 0.2-μm-wide electrodes and 19 0.2-μm-wide gaps (Ref. 6). (b) Calculated heterodyne conversion efficiency vs optical pump power for the same photomixer as in (a).

## VI. MODIFICATIONS OF PHOTOMIXER DESIGN

Two modifications of the basic photomixer structure in Fig. 1(a) would alleviate the heating problem and lead to a substantial improvement in the performance of the LTG-GaAs photomixer. First, the responsivity could be enhanced by increasing the internal quantum efficiency and the transmissivity through the top air–semiconductor interface. Second, the operating temperature of the photomixer could be greatly reduced by increasing the thermal conductance away from the active region. For example, $\eta_i$ would approach unity by embedding a GaAs/AlGaAs di-

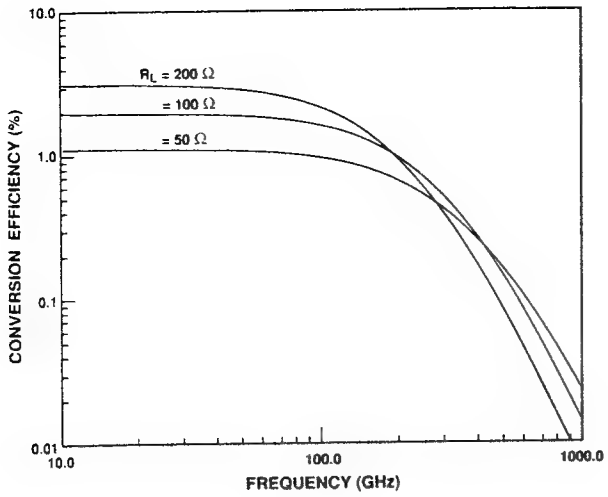


FIG. 4. Calculated heterodyne conversion efficiency versus difference frequency for the photomixer in Fig. 3. The total optical pump power was fixed at 50 mW, consistent with the estimated maximum operating temperature of 112 °C.

electric mirror between the LTG epitaxial layer and the GaAs substrate. The transmissivity would approach unity by depositing a quarter-wave antireflection coating on the top surface made out of a transparent dielectric material such as $Si_3N_4$. To see the effect of these modifications, we have projected the performance of the 0.2-$\mu$m-gap photomixer, assuming $t$ and $\eta_i=1.0$. In this case, we calculate $S=0.25$ A/W and $\epsilon_0^{max}=11.3\%$. The maximum conversion efficiency is attained at $P_0=247$ mW for $R_L=50$ Ω, $P_0=124$ mW for $R_L=100$ Ω, and $P_0=61$ mW for $R_L=200$ Ω. However, inclusion of the temperature constraint of 112 °C reduces the allowable pump power to 24 mW. This yields a temperature-limited output power and conversion efficiency of 0.8 mW and 3.3%, respectively, for $R_L=50$ Ω; 1.4 mW and 5.7%, respectively, for $R_L=100$ Ω; and 2.1 mW and 8.8%, respectively, for $R_L=200$ Ω. Although the heating constraint again precludes the attainment of $\epsilon_0^{max}$, the temperature-limited output power and conversion efficiency are more than doubled over their respective values in Sec. V because of the enhanced responsivity.

An effective way to increase the thermal conductance away from the active region would be to fabricate the photomixer on a substrate having a higher $\kappa$ than GaAs. This could be done by bonding the LTG-GaAs epitaxial layer to the preferred substrate, removing the GaAs substrate, and then fabricating the interdigitated structure. A promising substrate material is SiC, which has a room temperature $\kappa$ that is nearly eight times that of GaAs. The greatest impact of this technique would be on the performance of low-$R_L$ photomixers.

## VII. CONCLUSION

It is important to point out two advantages of the LTG GaAs over alternative photoconductive materials, such as semi-insulating or ion-bombarded GaAs, for the photomixing application. First, in the LTG GaAs the breakdown electric field is approximately $5\times10^5$ V cm$^{-1}$, whereas in the other photoconductive materials it is roughly three times lower. According to Eq. (10), this affects the maximum conversion efficiency quadratically. Second, LTG GaAs has a substantially shorter photocarrier recombination time. This allows the photomixer to operate in the millimeter-wave region and still be below the 3 dB power-conversion frequency. In the alternative GaAs materials, where $\tau$ is of the order of 10 ps, the conversion efficiency begins to fall by at least 6 dB per octave, starting in the microwave region. The shorter $\tau$ also allows the photomixer to withstand much higher optical powers before degradation of the photoconductive properties by high photogenerated-carrier density. This explains the remarkable experimental result that the LTG-GaAs responsivity in direct detection is nearly constant with pulsed optical pump intensities up to $3\times10^8$ W cm$^{-2}$ (Ref. 6). The combination of high breakdown field and short lifetime also means that the LTG-GaAs photomixer has the potential to operate efficiently with pulsed lasers for high-peak-power, low-average-power applications in millimeter-wave coherent radar. A derivation similar to that presented here indicates that pulsed conversion efficiencies in excess of 10% can be achieved with LTG-GaAs photomixers having electrode and gap widths greater than 1 $\mu$m (Ref. 12).

## ACKNOWLEDGMENTS

The authors thank R. A. Murphy and A. L. McWhorter for helpful comments on the manuscript. The work was sponsored by the Lincoln Laboratory Innovative Research Program and by the Department of the Air Force, in part under a program supported by the Air Force Office of Scientific Research.

[1] R. H. Pantell, M. DiDomenico, Jr., O. Svelto, and J. N. Weaver, *Proceedings of the 3rd International Conference on Quantum Electronics*, edited by P. Grivet and N. Bloembergen (Columbia Univ. Press, New York, 1964), Vol. 2, p. 1811.
[2] G. J. Simonis and K. G. Purchase, IEEE Trans. Microwave Theory Technol. **38**, 667 (1990).
[3] D. V. Plant, D. C. Scott, D. C. Ni, and H. R. Fetterman, IEEE Microwave Guided Wave Lett. **1**, 132 (1991).
[4] J. F. Whitaker, J. A. Valdmanis, M. Y. Frankel, S. Gupta, J. M. Chwalek, and G. A. Mourou, Microelectron. Eng. **12**, 369 (1990).
[5] M. Y. Frankel, J. F. Whitaker, G. A. Mourou, F. W. Smith, and A. R. Calawa, IEEE Trans. Electron Dev. **37**, 2493 (1990).
[6] Y. Chen, S. Williamson, T. Brock, F. W. Smith, and A. R. Calawa, Appl. Phys. Lett. **59**, 1984 (1991).
[7] J. B. D. Soole and H. Schumacher, IEEE Trans. Electron Dev. **37**, 2285 (1990).
[8] R. H. Kingston, *Detection of Optical and Infrared Radiation* (Springer-Verlag, Berlin, 1978).
[9] E. R. Brown, K. A. McIntosh, F. W. Smith, and M. J. Manfra (unpublished).
[10] R. A. Murphy (private communication).
[11] J. S. Blakemore, J. Appl. Phys. **53**, R123 (1982).
[12] E. R. Brown and F. W. Smith (unpublished).

# Measurements of optical-heterodyne conversion in low-temperature-grown GaAs

E. R. Brown, K. A. McIntosh, F. W. Smith, M. J. Manfra, and C. L. Dennis
*Lincoln Laboratory, Massachusetts Institute of Technology, Lexington, Massachusetts 02173-9108*

(Received 24 September 1992; accepted for publication 16 December 1992)

A low-temperature-grown GaAs interdigitated-electrode photomixer is used to generate coherent power at microwave frequencies. An output power of 200 $\mu$W (−7 dBm) is generated by pumping the photomixer with two 70-mW modes of a Ti:$Al_2O_3$ laser, separated in frequency by 200 MHz. This represents an optical-to-microwave conversion efficiency of 0.14%, which is within 50% of a prediction based on optical-heterodyne theory. When two lasers are used and the frequency of one is tuned with respect to the other, the output frequency of the photomixer increases smoothly and the output power is nearly constant up to 20 GHz. At higher frequencies the power decays because of parasitic capacitance.

Low-temperature-grown (LTG) GaAs possesses a subpicosecond electron-hole recombination time[1] and a photocarrier mobility ($\mu \approx 200$ cm$^2$ V$^{-1}$ s$^{-1}$) that is very high for a semiconductor having such a short recombination time. In addition to these remarkable properties, it displays a high breakdown field ($E_B > 4\times10^5$ V cm$^{-1}$). Together, these properties have led to impressive optoelectronic device results such as the generation of a 600-V-peak pulse having a full width at half-maximum of 2 ps (Ref. 2) and the direct detection of intense subpicosecond laser pulses with a responsivity of 0.1 A/W.[3] In this letter we present experimental results for LTG-GaAs as an optical-heterodyne converter, or photomixer.

Photomixing was proposed nearly three decades ago as a means of generating coherent radiation in the microwave region.[4] However, useful levels of output power have not been obtained because of the lack of robust photomixers and high-quality tunable lasers. With recent advances in high-speed III-V optoelectronic devices and solid-state lasers, interest in power generation by photomixing has been revived and new methods have been pursued. For example, a GaAs field-effect-transistor photomixer pumped by tunable dye lasers has generated coherent signals up to 61 GHz.[5] However, the output power generated by optical-heterodyne methods has been limited to the 1-$\mu$W level. In this letter, we demonstrate an LTG-GaAs photomixer having an output power of 0.2 mW and a response that is flat out to at least 20 GHz.

The photomixer consists of 10 interdigitated metal electrodes that are defined on the top surface of a LTG-GaAs epitaxial layer. The electrodes were made from gold and fabricated by electron-beam lithography and photoresist lift-off. The electrodes were 1.0-$\mu$m wide, 20-$\mu$m long, and separated by 1.0-$\mu$m-wide gaps. The underlying LTG-GaAs layer was grown by molecular-beam epitaxy on a semi-insulating GaAs substrate at a temperature of 195 °C. The thickness of the layer was approximately 1.0 $\mu$m. From previous characterizations on material grown under the same conditions, this LTG-GaAs layer is expected to have a photocarrier lifetime of approximately 0.6 ps and a breakdown electric field of approximately $5\times10^5$ V cm$^{-1}$. To couple power out of the photomixer at microwave frequencies, the electrodes were located in the gap between the center line of a coplanar waveguide and the ground plane, as shown schematically in Fig. 1. The characteristic impedance of the coplanar waveguide was 50 Ω, so that the output signal could be measured directly with a commercial spectrum analyzer. The coplanar waveguide also has the benefit of a very wide operational bandwidth. In the present configuration, the bandwidth is limited primarily by the parasitic gap capacitance, as discussed below.

The photomixer was optically pumped by two different methods using the arrangement shown in Fig. 2. In the first method, the dependence of photomixer output power on laser pump power at a fixed frequency was measured. The output from a single Ti:$Al_2O_3$ laser oscillating simultaneously on two adjacent longitudinal modes was coupled into a single-mode optical fiber and focused upon the interdigitated fingers using an output lens on the end of the fiber. The frequency difference between these modes was 200 MHz, and the pump power was nearly equally divided between them. In the second method, the dependence of photomixer response upon frequency was measured. The beams from a standing-wave Ti:$Al_2O_3$ laser and a ring Ti:$Al_2O_3$ laser at photon energies $h\nu_1$ and $h\nu_2$, respectively, were fiber optically combined and focused upon the interdigitated fingers. Because the fiber-optic combiner is single mode, the mixing efficiency of the two beams is very close to unity. The difference frequency $|\nu_2-\nu_1|$ was varied by tuning the wavelength of the ring laser relative to the 750-nm ($h\nu = 1.65$ eV) wavelength of the standing-wave laser.

Experimental results in the variable-power mode are given in Fig. 3(a). The output power $P_\omega$ from the photomixer at 200 MHz is plotted against the bias voltage $V_B$ between adjacent electrodes with the total incident optical pump power, $P_o$, as a parameter. $P_\omega$ increases monotonically with $P_o$ and $V_B$. The highest measured value of $P_\omega$ was −7.0 dBm with $P_o = 140$ mW and $V_B = 40$ V. With $P_0 = 170$ mW, $P_\omega = -8.4$ dBm was measured at $V_B = 36$ V. However, increasing $V_B$ toward 40 V led to the destruction of the device. In this sample $V_B$ was limited to 40 V or less to guard against electrical breakdown. In a separate photomixer sample of the same design, 50 V was safely applied



APPENDIX B

© 1993 American Institute of Physics

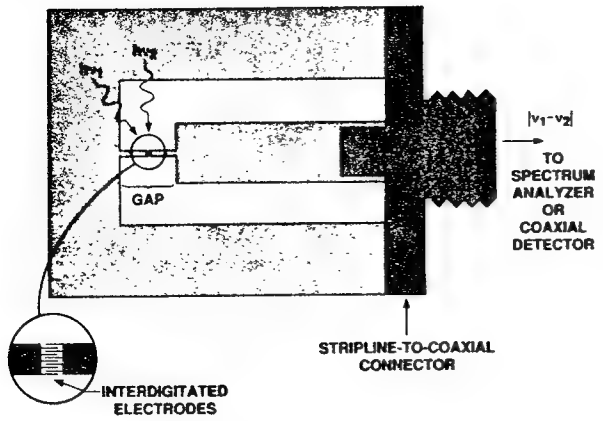


FIG. 1. LTG-GaAs photomixer mounted in coplanar-waveguide structure. The photomixer consists of interdigitated electrodes fabricated in the gap of a coplanar-waveguide transmission line.

in the absence of optical power, but the combination of $V_B=50$ V and high $P_o$ led to the destruction of the photomixer.

In Fig. 3(b) we show the optical-to-microwave conversion efficiency $\epsilon$ (i.e., the ratio of the output power to the pump power) for $P_o=100$ mW. Both $P_\omega$ and $\epsilon$ increase almost quadratically for $V_B$ up to about 20 V, and then increase superquadratically at higher voltages. At $V_B=40$ V, $\epsilon=0.14\%$, which is the highest value obtained to date. Also shown in Fig. 3(b) is a theoretical curve based on the following expression for $P_\omega$ at a circular difference frequency $\omega$,

$$P_\omega=\frac{\frac{1}{2}(V_BG_0)^2R_L}{[1+(\omega\tau)^2][1+(\omega R_LC)^2]}. \tag{1}$$

In this expression, $G_0$ is the time-averaged photoconductance of the photomixer, $R_L$ is the ac load resistance, $C$ is the capacitance of the interdigitated structure, and $\tau$ is the photocarrier lifetime. This expression is valid under the small-signal conditions $G_0R_L\ll1$, which is the case in the present experiments. For example, at $V_B=40$ V and $P_o=100$ mW, we measured a $G_0$ of approximately 50 $\mu$S, resulting in $G_0R_L=0.0025$. The expression in Eq. (1) can be understood by noting that the perfect mixing of two

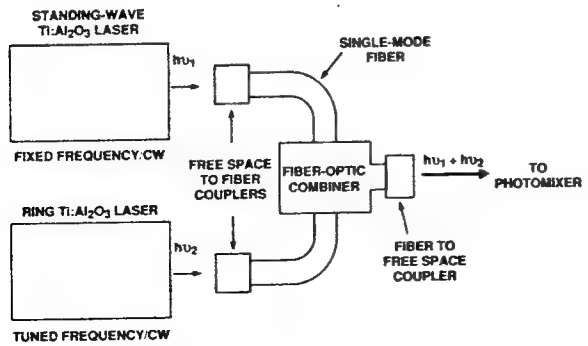


FIG. 2. Optical arrangement used to pump the LTG-GaAs photomixer. The Ti:$Al_2O_3$ standing-wave laser operates on two adjacent longitudinal modes, and the Ti:$Al_2O_3$ ring laser operates on a single mode whose wavelength is fine tuned by an internal etalon. The center wavelength of both lasers is approximately 750 nm.

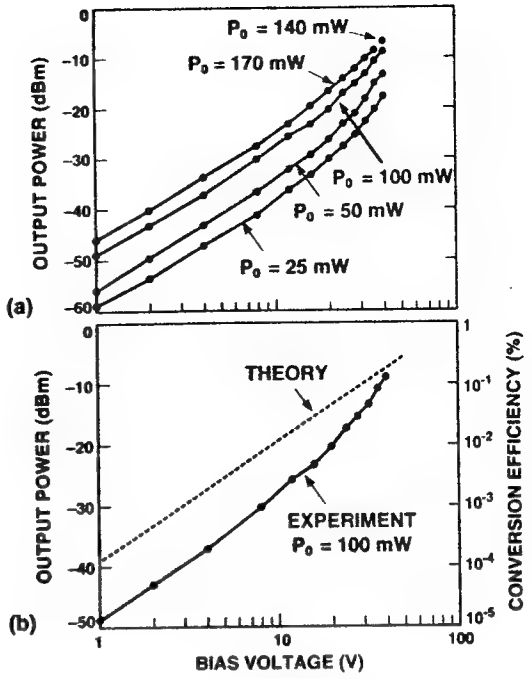


FIG. 3. (a) Output power from photomixer at 200 MHz as a function of bias voltage at five pump powers from the Ti:$Al_2O_3$ standing-wave laser. (b) Comparison of the experimental results from (a) at $P_o=100$ mW with small-signal photomixer theory.

laser lines of equal power generates a photoconductive response consisting of a dc component and a sinusoidal difference-frequency component, both of amplitude $G_0$.[6] If the photoconductor is connected to the series combination of the bias supply and $R_L$, the sinusoidal component gives rise to a nearly sinusoidal current through $R_L$ of amplitude $V_BG_0$ when $G_0R_L\ll1$. The power delivered to $R_L$ is then approximately $\frac{1}{2}(V_BG_0)^2R_L$. The two terms in the denominator represent a roll off in the power with frequency caused by the finite photocarrier lifetime and the displacement current through the interdigitated-electrode capacitance, which is calculated to be 6.1 fF in this photomixer.[7] At the difference frequencies of the present experiments, $\omega\tau\ll1$ and $R_LC\ll1$, so that the two terms in the denominator of Eq. (1) are very close to unity. A more accurate expression for the output power is derived in Ref. 8.

In Fig. 4 we plot the experimental output power as a function of $P_o$ for $V_B=8$ and 36 V, and we superimpose on this plot loci of constant $\epsilon$. At $V_B=36$ V, $\epsilon$ increases from 0.040% to 0.085% as $P_o$ increases from 25 to 170 mW. A more rapid increase is expected from Eq. (1) since in the small-signal limit $G_0$ should increase linearly with $P_o$ as given by $G_0=SP_o/V_B$, where $S$ is the external responsivity. Using the experimental value of $S=0.026$ A/W measured at $V_B=36$ V and low pump power, we obtain the theoretical output power shown in Fig. 4. At the lowest $P_o$ the experiment and theory are in excellent agreement, but at higher pump powers the experiment deviates on the low side. Also shown in Fig. 4 is the theoretical $P_\omega$ for $V_B=8$ V calculated using the experimental value $S=0.0025$ A/W. In this case the theory exceeds the experiment by over 7 dB at the lowest $P_o$ and the discrepancy grows with

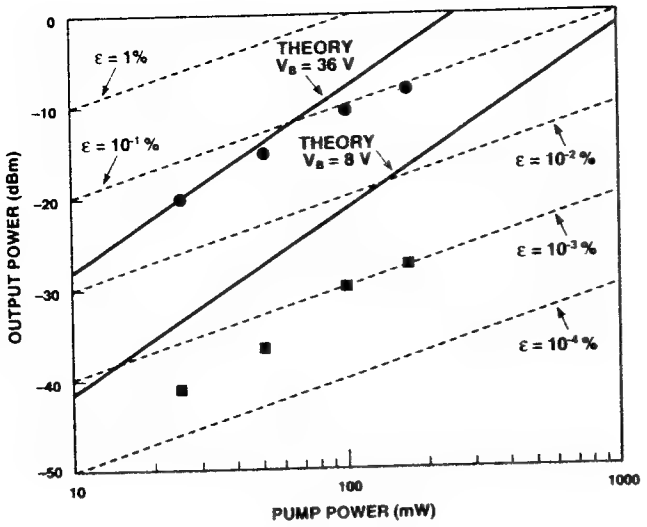


FIG. 4. Output power from photomixer at 200 MHz as a function of pump power at two bias voltages, 8 (squares) and 36 V (circles). Also shown are curves (solid lines) of the theoretical output power for these bias voltages and loci (dashed lines) of constant conversion efficiency.

increasing pump power. Inspection of Fig. 3(b) shows that this discrepancy occurred over the entire range of bias except at the high end. The reason for this trend is not presently understood.

We suspect that the subquadratic dependence of experimental output power on pump power at $V_B=36$ V is a result of device heating. A crude estimate of the temperature at the surface of the photomixer is obtained by assuming that the GaAs substrate is semi-infinite and that all of the optical pump power is absorbed in an infinitesimal thickness just below the photomixer surface. This leads to a temperature rise at the surface of $\Delta T \approx (P_a+P_{dc})/2\kappa D$,[9] where $P_a$ is the optical power absorbed in the photomixer, $P_{dc}$ is the dc electrical power dissipation, $\kappa$ is the room-temperature thermal conductivity of GaAs (0.46 W cm$^{-1}$ K$^{-1}$), and $D$ is the width of the active area of the photomixer (assumed to be square). The operating temperature is thus $T_{op}=T_0+\Delta T$, where $T_0$ is the ambient temperature. From considerations of geometric optics, $P_a$ is given by $P_a=tP_o w_g/(w_g+w_e)$, where $t$ is the optical transmissivity through the air-GaAs interface, $w_e$ is the width of the electrodes, and $w_g$ is the width of the gaps. At our optical wavelength of 750 nm, $t\approx 0.67$,[10] so that $P_a \approx 0.33P_o$. At a bias voltage of 36 V, the values of $P_{dc}$ are approximately 27, 41, 72, and 104 mW for $P_o=25$, 50, 100, and 170 mW. Thus for $T_0=25$ °C, the approximate values of $T_{op}$ are 44, 56, 82, and 112 °C at the respective pump powers.

The dependence of photomixer output power on difference frequency was measured with $P_o=25$ mW and $V_B=36$ V. Back reflection into the ring laser at higher pump powers caused the laser to run multimode and thus precluded accurate measurements. The output power was measured up to 50 GHz with a coaxial diode detector. The output power was practically constant with frequency up to 20 GHz and then rolled off at approximately 6 dB/octave. We attribute this roll off to the parasitic effect of the displacement current through the capacitance of the coplanar-waveguide gap shown in Fig. 1. From the dimensions of the coplanar gap (0.6-mm wide by 0.3-mm long), we estimate its capacitance as 90 fF. Combined with the 50-Ω load, the gap capacitance leads to a 3-dB roll off frequency of 35 GHz in agreement with the experiment. The intrinsic photocarrier lifetime and interdigitated-electrode capacitance are expected to yield 3-dB roll off frequencies of 265 and 522 GHz, respectively. By reducing the width of the center conductor of the coplanar waveguide, we expect that improved photomixer packages will have greatly reduced gap capacitance and will provide nearly constant $P_\omega$ up to at least 50 GHz.

In summary, we have demonstrated a LTG-GaAs interdigitated structure operating as an optical-heterodyne converter, or photomixer. The highest experimental output power was 200 $\mu$W at a frequency of 200 MHz, and the conversion efficiency at this output power was 0.14%. The frequency response of the photomixer was limited to about 25 GHz by parasitic capacitance, but the experimental results are consistent with a much higher intrinsic bandwidth.

The authors thank C. A. Graves and D. L. Landers for technical assistance, P. O. Jarvinen for technical guidance and useful suggestions on fiber-optic coupling, and S. B. Alexander for technical guidance and optoelectronic equipment support. This work was sponsored by the Lincoln Laboratory Innovative Research Program and by the Air Force Office of Scientific Research.

[1] J. F. Whitaker, J. A. Valdmanis, M. Y. Frankel, S. Gupta, J. M. Chwalek, and G. A. Mourou, Microelectron. Eng. 12, 369 (1990).
[2] M. Y. Frankel, J. F. Whitaker, G. A. Mourou, F. W. Smith, and A. R. Calawa, IEEE Trans. Electron. Devices ED-37, 2493 (1990).
[3] Y. Chen, S. Williamson, T. Brock, F. W. Smith, and A. R. Calawa, Appl. Phys. Lett. 59, 1984 (1991).
[4] R. H. Pantell, M. DiDomenico, Jr., O. Svelto, and J. N. Weaver, *Proceedings of the Third International Conference on Quantum Electronics*, edited by P. Grivet and N. Bloembergen (Columbia University Press, New York, 1964), Vol. 2, p. 1811.
[5] D. V. Plant, D. C. Scott, D. C. Ni, and H. R. Fetterman, IEEE Microwave Guided Wave Lett. 1, 132 (1991).
[6] R. H. Kingston, *Detection of Optical and Infrared Radiation* (Springer, Berlin, 1978).
[7] J. B. D. Soole and H. Schumacher, IEEE Trans. Electron Devices ED-37, 2285 (1990).
[8] E. R. Brown, F. W. Smith, and K. A. McIntosh, J. Appl. Phys. 73, 1480 (1993).
[9] R. A. Murphy (private correspondence).
[10] J. S. Blakemore, J. Appl. Phys. 53, R123 (1982).

# Milliwatt output levels and superquadratic bias dependence in a low-temperature-grown GaAs photomixer

E. R. Brown, K. A. McIntosh, F. W. Smith, K. B. Nichols, M. J. Manfra, C. L. Dennis, and J. P. Mattia
*Lincoln Laboratory, Massachusetts Institute of Technology, Lexington, Massachusetts 02173-9108*

(Received 2 September 1993; accepted for publication 6 April 1994)

A cw output power up to 0.8 mW is obtained from a low-temperature-grown (LTG) GaAs, 0.3 $\mu$m gap, interdigitated-electrode photomixer operating at room temperature and pumped by two modes of a Ti:$Al_2O_3$ laser separated in frequency by 0.2 GHz. The output power and associated optical-to-electrical conversion efficiency of 1% represent more than a sixfold increase over previous LTG-GaAs photomixer results obtained at room temperature. A separate LTG-GaAs photomixer having 0.6 $\mu$m gaps generated up to 0.1 mW at room temperature and up to 4 mW at 77 K. Low-temperature operation is beneficial because it reduces the possibility of thermal burnout and it accentuates a nearly quartic dependence of output power on bias voltage at high bias. The quartic dependence is explained by space-charge effects which result from the application of a very high electric field in the presence of recombination-limited transport. These conditions yield a photocurrent-voltage characteristic that is very similar in form to the well-known Mott–Gurney square-law current in trap-free solids.

Low-temperature-grown (LTG) GaAs remains of great interest to materials and device scientists alike because of its remarkable properties of high resistivity, high cross-gap photocarrier mobility relative to semiconductors of comparable resistivity, and very high dc breakdown fields. These properties have been utilized in several electrical and optical devices including field-effect transistors[1] and photon detectors.[2] Recently we have exploited these properties to make an optical heterodyne converter, or photomixer.[3] In previous work, the output power and optical-to-electrical (O-E) conversion efficiency of a photomixer operating at room temperature were limited to 200 $\mu$W and 0.15%, respectively. Here, the performance is enhanced considerably by improving the interdigitated electrode structure and by operating the photomixer at cryogenic temperatures.

The LTG-GaAs material in the present experiment was grown by molecular beam epitaxy (MBE) on a semi-insulating GaAs substrate. The substrate temperature during growth was approximately 195 °C and the ratio of arsenic to gallium fluxes was set at 10:1. The LTG-GaAs epitaxial thickness was approximately 1.0 $\mu$m. After growth, the sample was annealed in the MBE chamber at a temperature of 600 °C for 10 min with an arsenic overpressure. The sample was then characterized by time-resolved photoreflectance and was found to have a photocarrier lifetime of approximately 0.2 ps.

After annealing, interdigitated electrodes were fabricated on the top surface of the LTG GaAs by electron-beam lithography to define the active region of the photomixer.[3] The metal-electrode topography consisted of either forty 0.2-$\mu$m-wide electrodes separated by 0.3 $\mu$m gaps, or twenty 0.4-$\mu$m-wide electrodes separated by 0.6 $\mu$m gaps. The ratio of gap width to finger period in both structures is 20% higher than in our previous photomixer.[3] In principle, this yields a 44% improvement in photomixer output power and O-E conversion efficiency from the increase in external quantum efficiency alone. The final step of the fabrication was the creation of an electrical coplanar waveguide structure around each set of interdigitated electrodes. The coplanar waveguide was defined by optical lithography and Ti/Au metal lift-off. The characteristic impedance of the coplanar waveguide was designed to be 50 $\Omega$ to facilitate the measurement of the photomixer output signal at microwave frequencies.

The photomixer was driven by a single (standing wave) Ti:$Al_2O_3$ solid-state laser operating at a wavelength near 750 nm. The laser was internally adjusted by etalons to operate with equal output power in two adjacent longitudinal modes separated in frequency by 200 MHz. The output beam was focused down to a spot diameter of approximately 20 $\mu$m at the photomixer active region and the total power was varied by changing the power of the argon-ion laser that pumped the Ti:$Al_2O_3$ crystal. For each pump power, the dc bias voltage was increased from zero up to a value just below that which produced catastrophic breakdown.

Shown in Fig. 1(a) are the experimental results for the 0.6 $\mu$m gap photomixer at room temperature and for total optical pump powers of 45 and 75 mW. At both power levels, we observed a nearly quadratic increase in output power with dc bias voltage up to about 8 V, followed by a superquadratic increase at higher voltages. At a fixed bias voltage less than about 5 V, the output power also increased quadratically with pump power between 45 and 75 mW. Both quadratic functions are characteristic of any photomixer in which the photocurrent depends linearly upon bias voltage. The superquadratic dependence on bias voltage is similar to that observed in previous experiments[3] and is discussed below.

For 45 mW pump power, the output power at room temperature approaches a maximum value of −9 dBm at a bias voltage of 30 V. This represents an O-E conversion efficiency of approximately 0.3%. When the optical power or bias voltage was increased beyond this level, the device displayed thermal burnout. Burnout is not surprising under these operating conditions because the thermal conductivity of GaAs decreases rapidly with increasing temperature (ap-



APPENDIX C

© 1994 American Institute of Physics

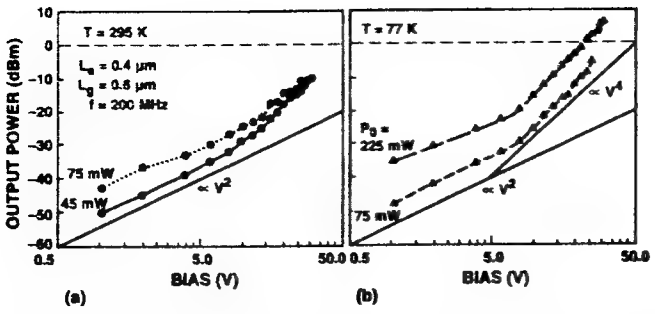


FIG. 1. Output power from 0.6 $\mu$m gap LTG-GaAs photomixer at 0.2 GHz as a function of bias voltage at two different operating temperatures: (a) $T$=295 K, (b) $T$=77 K. The dashed line in both figures denotes an output power of 0 dBm (1 mW).

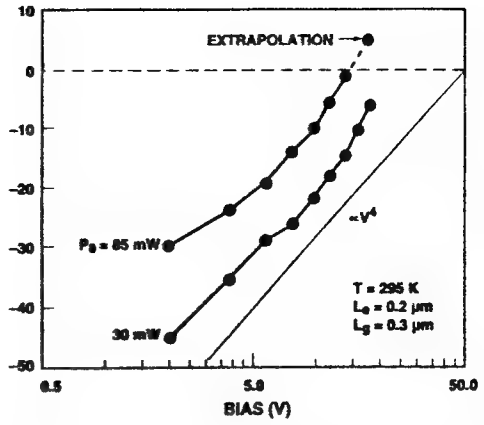


FIG. 2. Output power from 0.3 $\mu$m gap LTG-GaAs photomixer at 0.2 GHz as a function of bias voltage at room temperature. The horizontal dashed line denotes 1 mW. The dashed extrapolation to the curve for $P_0$=85 mW represents the projected output power of this device.

proximately as $T^{-5/4})^5$ up to at least 500 °C. The resulting rapid increase of temperature with optical power causes the resistance of the LTG GaAs to drop significantly, which can cause the electrical current in the LTG GaAs to run away. In the present experiments, the photomixer was biased with a constant-voltage power supply so that current runaway could not be suppressed.

With burnout in mind, we tested a 0.6 $\mu$m gap photomixer at 77 K by mounting the coplanar-waveguide sample on the cold finger of a liquid-nitrogen crystal. The laser pump beam was focused on the photomixer through a glass window on the outer vacuum jacket of the cryostat. Shown in Fig. 1(b) are the experimental results for optical pump powers of 75 and 225 mW. For the 75 mW pump and bias voltages less than 10 V, the output power was slightly less than at room temperature with the same pump power. Above 10 V bias, the dependence on bias voltage became superquadratic, and the output power at 77 K exceeded that at room temperature. The output power for 225 mW pump power was nearly 10 times that obtained with 75 mW, power, consistent with the theoretical quadratic dependence of output power on pump power. Above 10-V bias, the output power increases in a nearly quartic fashion such that +6 dBm (4 mW) was obtained at 30 V bias. The highest O-E conversion efficiency at 77 K was 1.5% under the conditions of 225 mW pump power and 30 V bias.

Shown in Fig. 2 are the experimental results for the 0.3 $\mu$m gap photomixer operating at room temperature with optical pump powers of 30 and 85 mW. For 30 mW pump power, the output power is approximately quartic with bias voltage from 2 up to about 10 V. Beyond 10 V, the output power increases superquartically in contrast to the behavior of the 0.6 $\mu$m gap device. With 85 mW pump power, the output power is quadratic up to about 5 V and then approximately quartic at higher voltages. The highest room-temperature output power was −1 dBm (0.8 mW), obtained with 85 mW pump power and 14 V bias. The highest O-E conversion efficiency was 1%, obtained with 30 mW pump power and 18 V bias. A bias of 18 V could not be applied with 85 mW pump power without destruction of the device, but a linear extrapolation of the curve in Fig. 2 yields a projected output power of +6 dBm (4 mW) under these conditions. We believe that this performance can be achieved by better heat sinking of the device or, perhaps, simply by using a ballast resistor in the bias circuit.

To understand the physical characteristics of the photomixer, we have examined the dc photocurrent and dark current as functions of bias voltage under the same conditions as used above. Shown in Figs. 3(a) and 3(b) are the experimental results for the 0.6 $\mu$m gap device at room temperature and 77 K, respectively. Below 5 V bias, the photocurrent is linear for 45 mW pump power at room temperature, and for both pump powers at 77 K. The linear dependence in these samples is indicative of ohmic transport in the bulk LTG GaAs, and suggests that the bulk resistance limits the current through the device rather than the metal-to-LTG-GaAs contacts. It also explains the quadratic dependence of output power on bias voltage. According to optical-heterodyne theory, the output power at the difference frequency is given by $P_\omega=\langle i^2\rangle Z_0$, where $\langle i^2\rangle$ is the rms average of the ac photocurrent at the difference frequency and $Z_0$ is the characteristic impedance of the load circuit. For moderate optical pump powers, we can write this as $P_\omega=(1/2)S_I^2P_1P_2Z_0$, where $S_I$ is the external current responsivity, and $P_1$ and $P_2$ are the average powers of the two pump lasers. In the case of ohmic transport, $S_I\propto V$, so that $P_0\propto V^2$.

At bias voltages above 5 V in the 0.6 $\mu$m gap device and above 2 V in the 0.3 $\mu$m device, the photocurrent began to increase nearly quadratically. This is indicative of nonohmic transport in the LTG GaAs and it explains the onset of the quartic dependence of output power on bias through the same argument as given above. Because the range of bias voltage over which the superlinear photocurrent occurs is so broad and because this behavior has been observed in all of our LTG-GaAs photomixers measured to date, it becomes an essential factor in explaining the milliwatt-level output of these devices. We have carried out a qualitative analysis of the photocurrent based on the drift and current-continuity equations for electrons and holes, ignoring the effects of carrier diffusion. The electrons and holes were assumed to have the same recombination rate but different lifetimes, $\tau_e$ and $\tau_h$, with $\tau_h>\tau_e$. The interdigitated electrodes were approximated as parallel plates with uniform current density be-

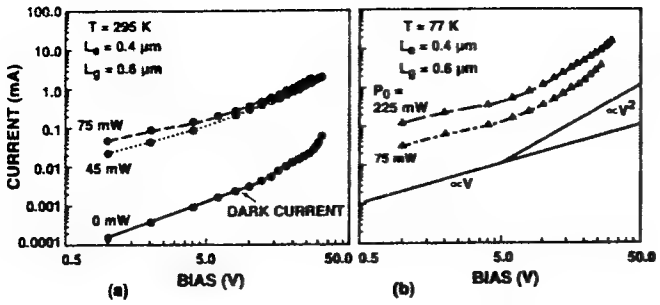


FIG. 3. Current-voltage curves for LTG-GaAs photomixer under the various experimental conditions: (a) $T=295$ K, (b) $T=77$ K. The dark-current curve at 77 K is not shown because it lies below the vertical current scale.

tween them. At low bias, ohmic behavior is displayed with the current density given by $J=e(n\mu_e+p\mu_h)E$, where $n(\mu_e)$ and $p(\mu_h)$ are the photoelectron and photohole densities (mobilities), respectively, and $E$ is the electric field between the contacts. In the low bias limit, $E$ is uniform and equal to $V/L$ where $L$ is the distance between electrodes in the parallel-plate approximation. When $V$ is increased to the point where the quantity $L^2(\mu_e+\mu_h)/\mu_e\mu_h V$ becomes comparable to or less than $\tau_h-\tau_e$, the current density begins to increase quadratically consistent with the expression $J=(9/8)aV^2/L^3$ where $a=e(\mu_e\tau_e+\mu_h\tau_h)\mu_e\mu_h g(\tau_h-\tau_e)/(\mu_e+\mu_h)$ and $g$ is the cross-gap photogeneration rate. For example, if we assume $L=0.6$ μm and the room-temperature values $\mu_e=400$ cm$^2$ V$^{-1}$ s$^{-1}$,[5] $\mu_h\approx100$ cm$^2$ V$^{-1}$ s, $\tau_h\approx5$ ps, $\tau_e\approx0.2$ ps, we find a crossover from ohmic to quadratic behavior at $V\approx16$ V. This is in good agreement with the photocurrent shown in Fig. 3(a).

The above quadratic current-voltage relation is very similar superficially to the Mott–Gurney law for a trap-free insulator in which the current is limited by the buildup of free space charge between the contacts.[6] Our analysis for the LTG GaAs leads to a similar deviation from space-charge neutrality because of the difference between the electron and hole lifetimes and because of the high bias fields in the material which spatially separate the photogenerated electron-hole pairs. This deviation from ohmic behavior has conventionally been called "recombination-limited transport" and has been observed in semiconductors and insulators.[7]

Several other mechanisms have been considered to explain the superlinear behavior of the photocurrent. The first was cross-gap impact ionization. At the highest bias voltages, the electron potential-energy drop between the cathode and anode electrodes is over 10 times the GaAs band-gap energy $E_g$. This may enable photoelectrons generated near the cathode to gain the required kinetic energy, $3E_g/2$, to create a new electron-hole pair. However, when impact ionization occurs in semiconductor devices, it usually leads to avalanche breakdown, which is always characterized by a very rapid increase in current with voltage. Judging from the relatively gradual current-voltage characteristics in Fig. 3, we believe that avalanche breakdown is not occurring in the 0.6 μm gap device. Nevertheless, we cannot rule out the possibility that either the small distance between electrodes or the very short recombination time in these samples is prohibiting avalanche multiplication but allowing for limited impact ionization. This may explain the superquartic dependence at high bias voltages for the 0.3 μm device in Fig. 2.

A second mechanism that we considered was Zener tunneling at the As precipitates that exist in all LTG-GaAs samples annealed after the growth.[8] We were led to this mechanism by an observation made long ago of soft reverse breakdown in Ge $p$-$n$ diodes contaminated by metallic precipitates.[9] We ruled out this mechanism based on the observed variation of the photocurrent with temperature. In comparing Figs. 3(a) and 3(b), we see that the quadratic dependence becomes much more pronounced in lowering the temperature to 77 K. In contrast, Zener tunneling in GaAs would become less pronounced because of the significant increase in $E_g$ that occurs between room temperature and 77 K.[10]

In conclusion, we have demonstrated a LTG-GaAs photomixer having milliwatt output power levels in operation at room temperature and much greater output powers in operation at 77 K. The performance of this device is due in large part to a nearly quadratic dependence of photocurrent on bias voltage. We attribute the quadratic dependence to space-charge effects which result from the application of very high electric fields in the presence of recombination-limited transport. Because of the intrinsic photoconductive speed of the LTG GaAs, the milliwatt output power makes the photomixer very promising as a broadband tunable source operating from dc to frequencies well above 100 GHz.

We acknowledge K. M. Molvar, W. F. DiNatale, and D. J. Landers for expert technical assistance in the fabrication of photomixers, D. C. Look for helpful conversations and R. A. Murphy for useful comments on the manuscript. This research was sponsored by the Air Force Office of Scientific Research, the U.S. Army Research Office, and the Lincoln Laboratory Innovative Research Program.

[1] F. W. Smith, Mater. Res. Soc. Symp. Proc. **241**, 1 (1992).
[2] Y. Chen, S. Williamson, T. Brock, F. W. Smith, and A. R. Calawa, Appl. Phys. Lett. **59**, 1984 (1991).
[3] E. R. Brown, K. A. McIntosh, F. W. Smith, M. J. Manfra, and C. L. Dennis, Appl. Phys. Lett. **62**, 1206 (1993).
[4] J. S. Blakemore, J. Appl. Phys. **53**, R123 (1982).
[5] D. C. Look, D. C. Walters, G. D. Robinson, J. R. Sizelove, M. G. Mier, and C. E. Stutz, J. Appl. Phys. **74**, 306 (1993).
[6] N. F. Mott and R. W. Gurney, *Electronic Processes in Ionic Crystals* (Oxford University Press, London, 1940).
[7] M. A. Lampert and P. Mark, *Current Injection in Solids* (Academic, New York, 1970).
[8] A. C. Warren, J. M. Woodall, J. H. Burroughes, P. D. Kirchner, H. K. Heinrich, G. Arjavalingam, N. Katzenellenbogen, D. Grischkowsky, M. R. Melloch, N. Otsuka, K. Mahalingam, F. H. Pollak, and X. Yin, Mater. Res. Soc. Symp. Proc. **241**, 15 (1992).
[9] A. Goetzberger and W. Shockley, J. Appl. Phys. **31**, 1821 (1960).
[10] S. Sze, *Physics of Semiconductor Devices* (Wiley, New York, 1982).

PROCEEDINGS REPRINT

SPIE–The International Society for Optical Engineering

*Reprinted from*

# *Nonlinear Optics for High-Speed Electronics and Optical Frequency Conversion*

**24–26 January 1994**
**Los Angeles, California**

**Volume 2145**

©1994 by the Society of Photo-Optical Instrumentation Engineers
Box 10, Bellingham, Washington 98227 USA. Telephone 206/676-3290.

APPENDIX D

Invited Paper

# Optical-heterodyne generation in low-temperature-grown GaAs up to 1.2 THz

E. R. Brown, K. A. McIntosh, K. B. Nichols, M. J. Manfra, and C. L. Dennis
*Lincoln Laboratory*
*Massachusetts Institute of Technology*
*Lexington, MA 02173-9108, USA*

**Abstract**

Low-temperature-grown (LTG), nonstoichiometric GaAs is used as an optical mixer to generate coherent output radiation up to a frequency of 1.2 THz. The mixer structure consists of an epitaxial layer of the LTG GaAs material with submicrometer interdigitated electrodes fabricated on the top surface. Terahertz photocurrents are generated in the gaps between the electrodes, and power is radiated by coupling these currents efficiently into a self-complementary spiral antenna. The experimental rolloff in photomixer output power is explained by two time constants – one for the electron-hole recombination time and the other for the photomixer-antenna circuit. The photomixer demonstrates the capability to generate continuous-wave radiation in a spectral region where tunable coherent radiation has been lacking.

## I. Background

The far-infrared spectral region between approximately 1 and 10 THz has long been devoid of solid-state sources. This region is depicted clearly in the diagram of solid-state source technology in Fig. 1. At low-frequencies electronic oscillators have been making incremental gains for many years, but they have not achieved useful operation at 1 THz or beyond. Heterostructure transistors such as high-electron-mobility transistors (HEMTs) or heterojunction bipolar transistors (HBTs) can now operate up to approximately 200 GHz. The maximum oscillation frequency ($f_{max}$) is limited largely by the electronic transit time associated with the middle terminal (i.e., the gate of the HEMT or base of the HBT). Negative-resistance diode oscillators are even more effective in this range because of their simplicity. For example, IMPATT diodes have oscillated at fundamental frequencies up to about 300 GHz [1], and resonant-tunneling diodes up to 700 GHz [2]. In these diodes, the $f_{max}$ is usually limited by a cancellation of the negative resistance at high frequencies by parasitic positive resistance in the device and the connecting circuit. The positive resistance tends to grow with frequency because of the skin effect in metals, radiative losses in transmission lines and interconnects, and dielectric relaxation in semiconductor epitaxial layers, among other factors. To avoid the problems


0-8194-1440-9/94/$6.00

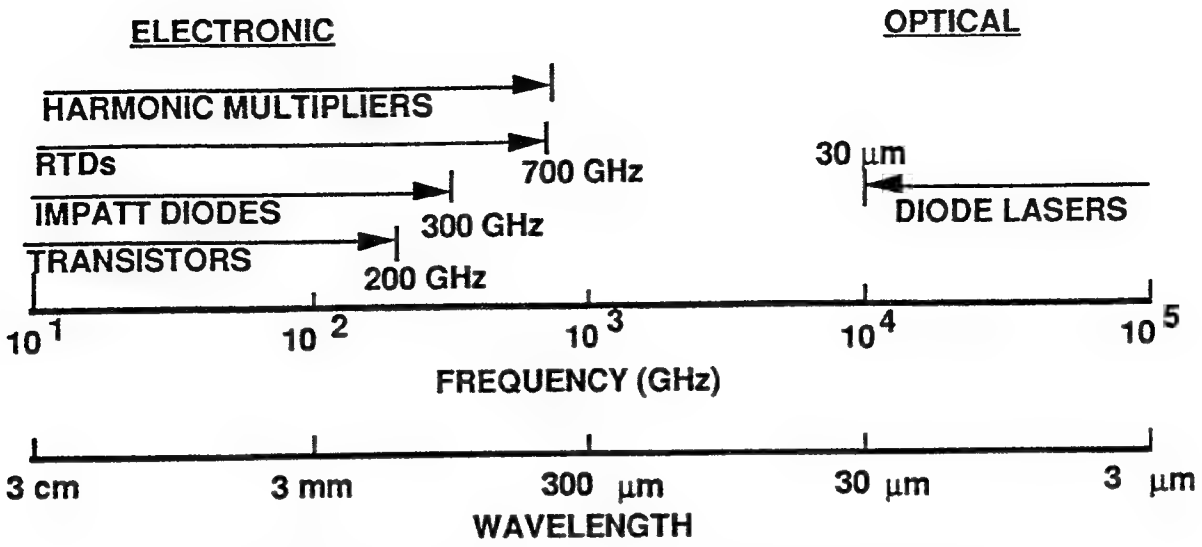


Fig. 1. Solid-state source technology in the far-infrared region.

associated with fundamental-frequency electronic oscillators, harmonic-multiplication techniques have long been applied using powerful pump sources, such as klystrons or Gunn diodes, operating around 100 GHz. While harmonic multiplication can be very efficient in doubling or even tripling, the efficiency falls rapidly at higher harmonic number because of the difficulty in properly terminating the harmonics below the desired one.

At the high-frequency end of the range, narrow-bandgap diode lasers have operated out to approximately 20 μm, but have been prohibited from going to longer wavelengths by Auger and alloy scattering and by free-carrier absorption. More recently, Bloch oscillations have been observed in the Wannier-Stark ladders of quantum wells (see paper by J. Shah in this proceedings). While the Bloch oscillation has the emission strength to support lasing, the short electron nonradiative lifetime in the upper energy levels makes the threshold pump power, be it optical or electrical, very high. To avoid the problems associated with lasers, various forms of optical mixing were explored as far back as the 1970's. For example, three-wave mixing has been carried out using two frequency-offset lasers and nonlinear crystals, such as $LiNbO_3$, having a large $\chi^2$ optical susceptibility. Unfortunately, in converting near-infrared or visible laser light to the far-infrared in conventional nonlinear crystals, three-wave mixing is limited in conversion efficiency to far less than 1% by the Manley-Rowe relation [3]. A second optical mixing technique that has been investigated is optical-heterodyne conversion [4]. The main drawback in this technique has been the lack of a heterodyne converter that has the ruggedness and bandwidth to produce useful levels of power at frequencies in excess of 100 GHz.

The present work deals with a new type of optical-heterodyne converter, or photomixer,

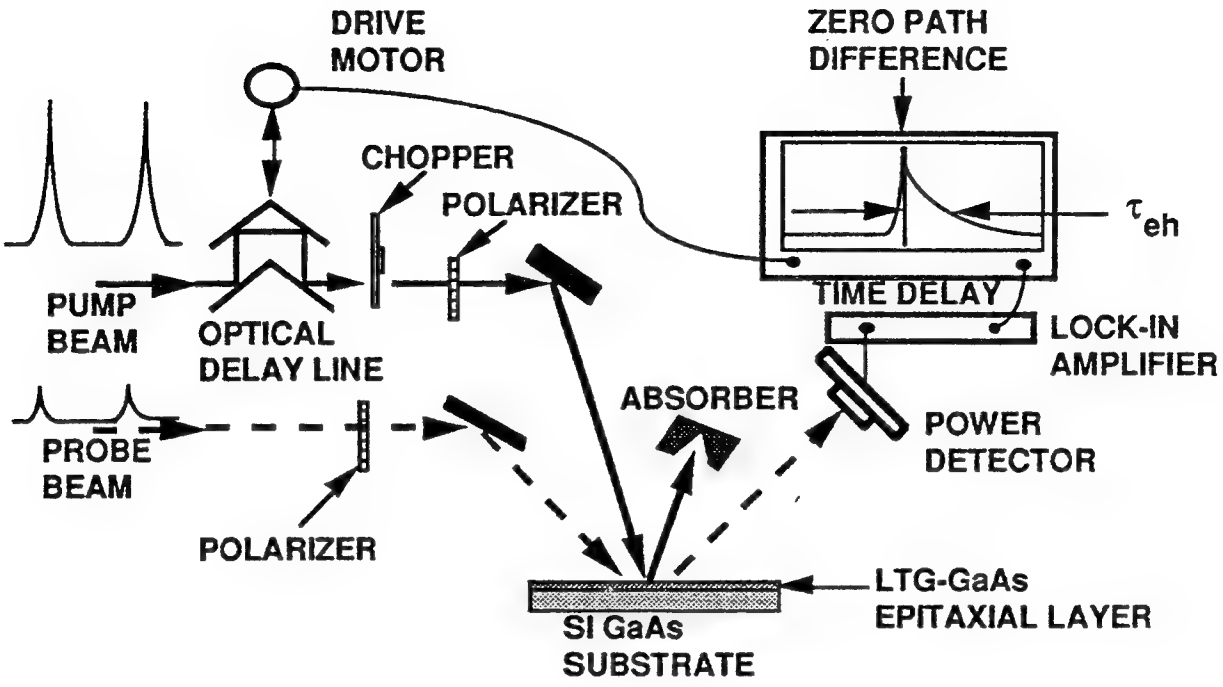


Fig. 2. Time-resolved photoreflectance experiment.

having an electrical bandwidth approaching 1 THz. The basis for the photomixer is a superior type of photoconductive material – low-temperature-grown (LTG) GaAs. LTG GaAs is unique in that it exhibits a very short photoconductive lifetime ($\tau < 1$ ps), a high electrical breakdown field ($E_B > 5X10^5$ V-cm$^{-1}$), and a high photocarrier mobility compared to materials having a comparable lifetime. As such, LTG GaAs is capable of withstanding the optical pump powers and bias voltages required to achieve milliwatt levels of continuous-wave (cw) output power.

## II. LTG-GaAs Growth and Characterization

Our LTG GaAs is grown by molecular-beam epitaxy (MBE) at a temperature in the range of 180 to 250 °C and in the presence of arsenic overpressure in the growth chamber. The resulting material is nonstoichiometric with about 1% excess arsenic. After growing approximately 1 μm of material, the gallium source is closed. A thermal anneal is then carried out at approximately 600 °C in the arsenic flux for a duration of 10 minutes. The thermal anneal causes the large concentration of excess arsenic atoms to rearrange either as antisite defects (i.e., an arsenic atom at a gallium site) or to cluster together as metallic arsenic precipitates. The relationship between the defects and the desirable characteristics (i.e., high resistivity and short photoconductive lifetime) is somewhat controversial. One school of thought attributes these

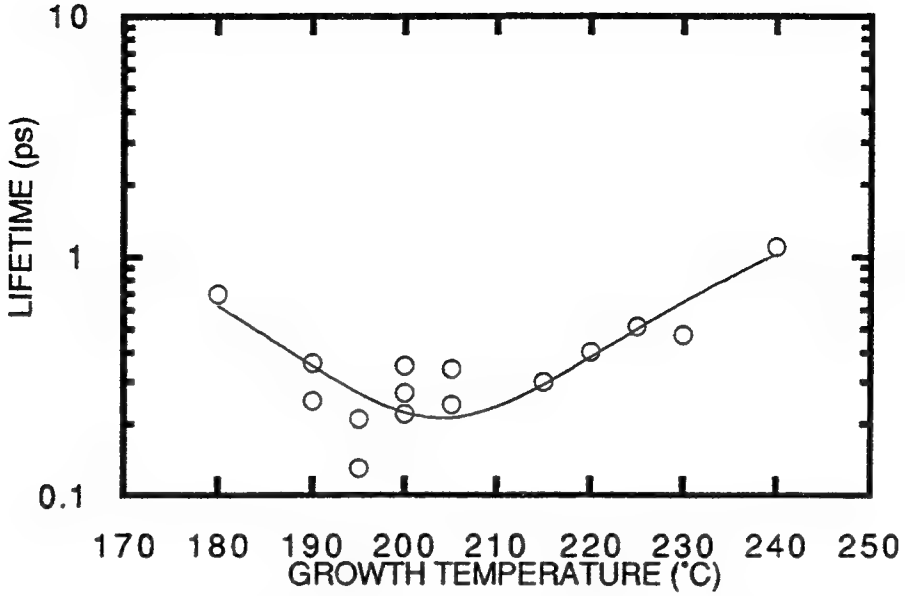


Fig. 3. Experimental results of photocarrier lifetime vs MBE growth temperature.

characteristics exclusively to the high concentration ($\approx 10^{18}$ cm$^{-3}$) of antisite defects, which leads to very low background-carrier concentrations and a high probability of Shockley-Read-Hall-like recombination [5,6]. The other school of thought attributes these characteristics to the short distance between the precipitates, which leads to a depletion of background carriers and a high probability for recombination of photocarriers close to the site of their generation [7].

For the high-frequency photomixer application, the most important characteristic of the LTG GaAs is the electron-hole photocarrier lifetime, $\tau_{eh}$. To determine this quantity, we used the technique of time-resolved photoreflectance depicted in Fig. 2. This is a pump-probe technique in which the optical pulse train from a mode-locked laser is split into two separate beams. The more powerful pump beam is directed through an optical delay line, mechanically chopped, and then focused on the surface of the LTG-GaAs epitaxial layer where it excites electron-hole pairs. The probe beam is focused onto the same spot as the pump beam and the average power of the reflected probe beam is measured with a slow photon detector as the delay line varies the optical path length of the pump beam. The change in path length is equivalent to a time delay of the probe beam with respect to the pump beam. The photon detector is connected to a lock-in amplifier is sensitive only to changes in the reflectivity induced by the pump beam. As the time delay of the pump beam is varied so that the pump and probe pulses arrive at the LTG-GaAs layer simultaneously, the pump has its maximum effect, as shown in the inset of Fig. 2. As the probe beam is delayed further, the signal strength drops off over a time scale directly related to the lifetime of the photocarriers induced by the pump. The accuracy of this method

is limited only by the finite length of the pump and probe pulses, which in our laser is approximately 80 fs.

Shown in Fig. 3 are the experimental lifetimes measured for a variety of LTG-GaAs samples grown between 180 and 240 °C. Over this entire temperature range, $\tau_{eh}$ is below 1 ps. The best samples for photomixers are those grown between about 190 and 210 °C, in which $\tau_{eh}$ is in the range of 0.2 to 0.4 ps. The minimum lifetime that we have observed is 0.15 ps in a sample grown at 195 °C. This temperature defines a rough minimum in the lifetime vs growth temperature represented by the solid curve fit shown in Fig. 3.

## III. Optical Pumping Configuration

A schematic diagram of the laser pumping configuration used in our experiments is shown in Fig. 4. It consists of two Ti:$Al_2O_3$ lasers, each pumped by an argon-ion laser. One of the Ti:$Al_2O_3$ lasers has a standing-wave optical cavity and is kept at a fixed wavelength of about 800 nm over the course of the experiments. The output power of this laser is typically in the range of 0.1 to 0.5 W depending on the ion-laser pump power. The output is divided between, at most, two longitudinal modes separated in frequency by 200 MHz. The other Ti:$Al_2O_3$ laser has a ring cavity with an optical isolator just outside to maintain single-mode, single-frequency operation. The ring laser is tuned continuously in wavelength by a birefringent etalon located inside the cavity. The cw output power of the ring laser is typically in the range of 0.2 to 1.0 W, again depending on the ion-laser pump power.

One of the attractive features of photomixing is that the delicate task of beam combining can now be carried out using fiber-optic components. As shown in Fig. 4, this is done by first transforming the output beams of the Ti:$Al_2O_3$ lasers into single-mode fiber using free-space-to-fiber couplers. The two single-mode fibers are connected to a broadband fiber-optic power combiner. Although the combiner is somewhat inefficient (only about 25% of the total input power gets into the output fiber), it is quite rugged and vibration insensitive compared to any free-space combining technique. After combining, the beams are transformed back into free space and focused on the photomixer active region.

## IV. LTG-GaAs Photomixer

To obtain a photomixer having a sufficiently low capacitance to operate at terahertz frequencies, we have implemented the interdigitated contact structure shown in the electron micrograph at the lower right of Fig. 5. The interdigitated electrodes are fabricated on the top surface of the LTG GaAs by the following steps. First, electron-beam lithography is used to open up channels having the dimension of the desired electrodes in a thin layer of

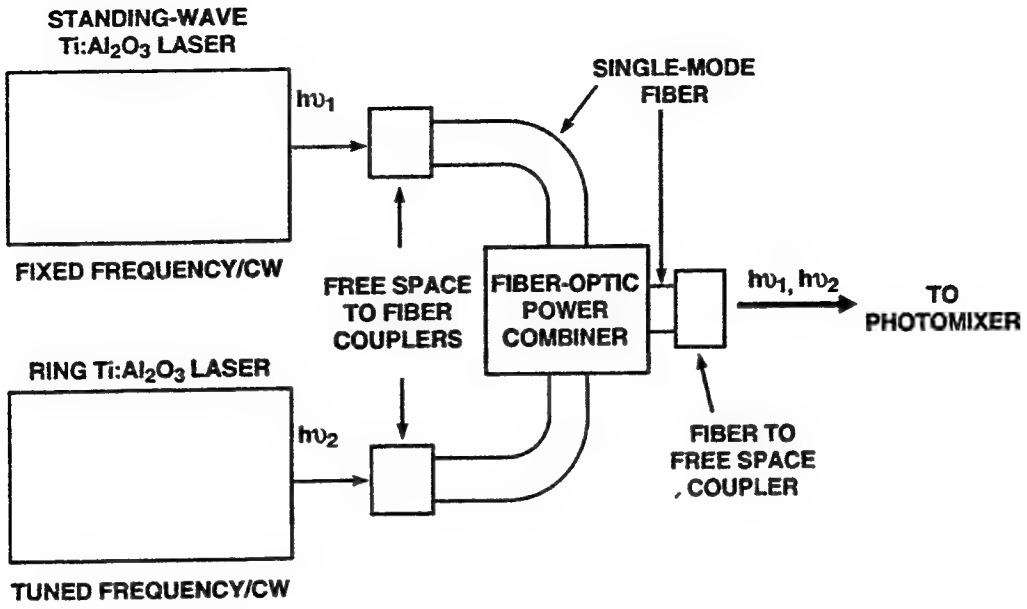


Fig. 4. Experimental configuration for optically pumping the photomixer.

polymethylmethacrylate (PMMA). Then thin layers of titanium and gold are deposited on the entire pattern. Finally, the metal over the grid of remaining PMMA is lifted off using a chemical solvent. The width of the electrodes is typically 0.2 μm and the separation between electrodes is typically 0.6 μm.

In operation, the laser beams are focused on the interdigitated-electrode region, generating electron-hole pairs in the LTG-GaAs gaps between the electrodes. The density of electrons and holes varies in time at the difference frequency between the two lasers. Because of the large dc-bias field applied between electrodes, the photocarriers drift to opposite contacts. This constitutes a time varying photocurrent that can generate power by driving the characteristic impedance of a transmission line or the radiation resistance of an antenna. We use a 50-Ω coplanar waveguide (CPW) as the transmission line for frequencies from 0.2 to 50 GHz [8]. For higher frequencies, we couple the interdigitated-electrode structure to a self-complementary spiral antenna as shown in Fig. 5. The spiral is a type of broadband antenna whose useful range can easily exceed 1 decade of frequency. When lying on a GaAs half-space, its radiation resistance is approximately 72 Ω. The low frequencies radiate from the outer extent of the spiral, and the high ones radiate from the inner extent. At all frequencies the majority of the radiation goes into the GaAs substrate because of its high dielectric constant. The radiation is transformed

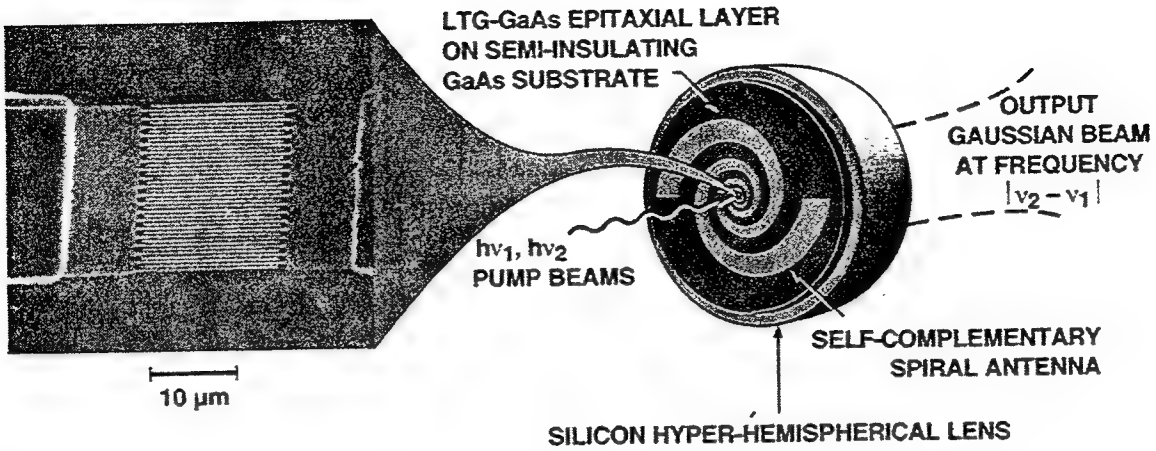


Fig. 5. LTG-GaAs photomixer coupled to broadband self-complementary spiral antenna and silicon hyper-hemispherical lens.

into free space without significant total-internal reflection by abutting the substrate to a silicon hyper-hemispherical lens. The radiation coming out of the lens forms a diverging quasi-Gaussian beam which is easily coupled into other millimeter-wave components and systems.

## V. Experimental Results

Our first high-frequency measurements were carried out on an interdigitated structure having 22 0.2-μm-wide electrodes and 21 0.6-μm-wide gaps. The spiral antenna for the high-frequency measurements had two complete turns in each arm with an inner radius of 30 μm and an outer radius of 1.8 mm. These dimensions correspond to a frequency range of approximately 60 GHz to 1.0 THz. The output power from the spiral antenna was measured with a liquid-helium-cooled composite bolometer having high sensitivity throughout the far-infrared region. The output frequency was determined by separately measuring the frequency of each pump laser using an optical wavemeter with an accuracy of approximately 1 GHz.

Figure 6 is a plot of the photomixer cw output power as a function of laser difference-frequency between 10 GHz and 1.2 THz. The data point at 20 GHz was measured with the

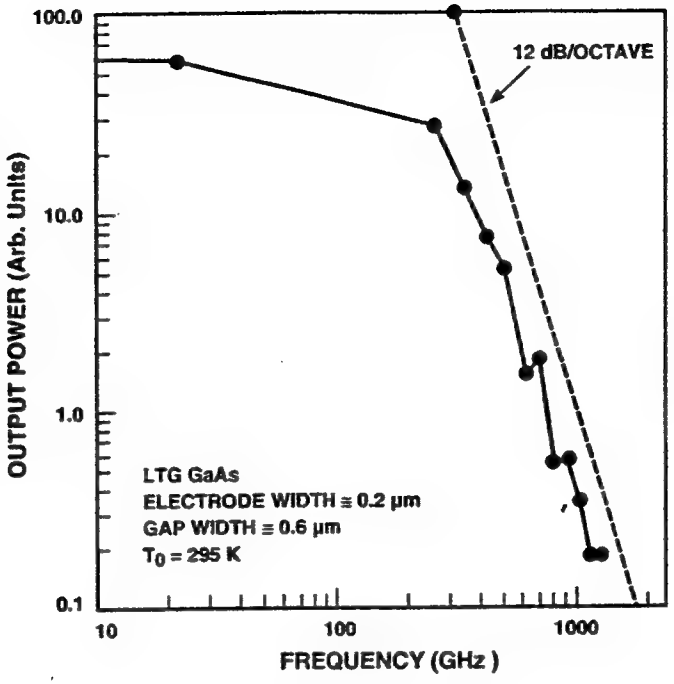


Fig. 6. Experimental results for LTG-GaAs photomixer coupled to a coplanar-waveguide transmission line (20-GHz point) and to a self-complementary spiral antenna.

photomixer coupled to the CPW structure. The data at higher frequencies was obtained with the spiral-antenna structure. Relative to the 20-GHz point the output power is down approximately 3 dB at 250 GHz, and then rolls off at about 6 dB/octave between 250 and 500 GHz. This behavior can be explained by the RC time constant of the load circuit, where R is the 72-Ω radiation resistance of the spiral antenna and C is the interdigitated-electrode capacitance. According to electrostatic theory, the capacitance of this structure is approximately 8.4 fF. Hence, we calculate RC ≈ 0.60 ps and a 3-dB frequency of $(2\pi RC)^{-1}$ = 263 GHz, in good agreement with experiment. Above 500 GHz, the experimental power rolls off at a rate of approximately 12 dB octave. This can be explained by the onset of $\tau_{eh}$ as a second electrical time constant. Our LTG GaAs had a photocarrier lifetime of 0.35 ps as measured by the photoreflectance technique described in Sec. II. Thus, the output power should begin rolling off rapidly at a frequency of $(2\pi\tau)^{-1}$ = 455 GHz, in fair agreement with the experiment.

Another well-understood aspect of the photomixer performance is the output polarization. Up to frequencies of approximately 300 GHz, the output beam from the spiral antenna is nearly circularly polarized as expected. Above approximately 800 GHz, the output becomes linearly

polarized. We believe that this represents a transition from radiation by the spiral to radiation by the dipole-like interconnect metal between the interdigitated electrodes and the inner radius of the spiral. Taking the 60 μm length of the interconnect as the physical length of the dipole, we estimate that a half-wave dipole resonance should occur at a frequency of 950 GHz. Between this point and the full-wave resonance, we expect the interconnect to radiate efficiently because the radiation resistance should increase rapidly with frequency.

## Summary

We have demonstrated the very high electrical bandwidth of an LTG-GaAs photomixer. Using two Ti:$Al_2O_3$ lasers to pump the photomixer and the combination of a CPW transmission line at low frequencies and a self-complementary spiral antenna at high frequencies to produce the output power, we obtained a 3-dB bandwidth of approximately 250 GHz and easily measured power levels out to 1.2 THz. The LTG-GaAs photomixer may fill the need for solid-state coherent radiation at frequencies above 1 THz, where tunable solid-state sources are lacking.

## Acknowledgments

The authors wish to thank Phil Jarvinen for technical support, and K. M. Molvar and C. A. Graves for expert technical assistance. This work was sponsored by the Air Force Office of Scientific Research, the U.S. Army Research Office, and the Lincoln Laboratory Innovative Research Program.

## References

[1]. M. Ino, T. Ishibashi, and M. Ohmori, Jpn. J. Appl. Phys., Suppl. **16-1**, 89 (1977).
[2]. E. R. Brown, J. R. Söderström, C. D. Parker, L. J. Mahoney, K. M. Molvar, and T. C. McGill, Appl. Phys. Lett. **58**, 2291 (1991).
[3]. A. Yariv, *Quantum Electronics* (Wiley, New York, 1975), p. 438.
[4]. D. V. Plant, D. C. Scott, D. C. Ni, and H. R. Fetterman, IEEE Microwave Guided Wave Lett. **1**, 132 (1991).
[5]. F. W. Smith, in *Low Temperature (LT) GaAs and Related Materials,* ed. by G. L. Witt, A. R. Calawa, U. Mishra, and E. Weber, Materials Research Society Symposium Proceedings, vol. 241 (Mater. Res. Soc., Pittsburgh, 1992), p. 3.
[6]. F. W. Smith, "The Device Applications and Characterization of Nonstoichiometric GaAs Grown by Molecular-Beam Epitaxy," Ph.D. thesis, Massachusetts Institute of Technology, 1990.
[7]. A. C. Warren, J. M. Woodall, J. H. Burroughes, P. D. Kirchner, H. K. Heinrich, G. Arjavalingam, N. Katzenellenbogen, D. Grischkowsky, M. R. Melloch, N. Otsuka, K. Mahalingam, F. H. Pollak, and X. Yin, in *Low Temperature (LT) GaAs and Related Materials,* ed. by G. L. Witt, A. R. Calawa, U. Mishra, and E. Weber, Materials Research Society Symposium Proceedings, vol. 241 (Mater. Res. Soc., Pittsburgh, 1992), p. 15.
[8]. E. R. Brown, K. A. McIntosh, F. W. Smith, M. J. Manfra, and C. L. Dennis, Appl. Phys. Lett. **62**, 1206 (1993).

# Resonant-Tunneling Transmission-Line Relaxation Oscillator

E. R. Brown

*Lincoln Laboratory, Massachusetts Institute of Technology, Lexington, Massachusetts 02173-9108*

## Abstract

A new type of resonant-tunneling oscillator is analyzed that does not require dc bias stability in the negative-differential-resistance region. The oscillator consists of a resonant-tunneling diode coupled to a transmission line in such a way that repetitive switching of the diode occurs across the negative-resistance region. The output waveform consists of a sequence of pulses having a repetition rate determined by the electrical delay of the transmission line and a pulse width determined by the switching time of the diode. When the electrical delay is comparable to the switching time, the output is quasi-sinusoidal. Numerical simulations with a prototype resonant-tunneling diode yield a maximum repetition rate of 192 GHz and a pulse width of 2 ps.

## Introduction

The resonant-tunneling diode (RTD) has been one of the most successful quantum-transport devices. The trademark characteristic of the RTD, the negative-differential-resistance (NDR) region, has been observed at room temperature in many different material systems and over a very wide range of current density. The NDR region has been used as the basis for high-frequency oscillations and high-speed switching. For example, double-barrier RTDs made from the InAs/AlSb system have oscillated up to 712 GHz [1], and similar diodes made from the GaAs/AlAs system have switched from the peak point to the valley region in a time near 2 ps [2]. Much of the interest in RTDs stems from the fact that these results are among the highest oscillation frequencies and the lowest switching times reported to date for electronic devices.

In spite of these successes, the double-barrier RTD has one fundamental shortcoming for the oscillator application. The steep slope in the NDR region makes it very difficult to achieve dc bias stability in this region. Consequently, only small-area diodes having a suitably high differential resistance can be used. In the case of oscillators, the small area leads to a low output power relative to other two-terminal negative-resistance devices, such as Gunn and IMPATT diodes. To overcome this shortcoming, one must design either an RTD oscillator that does not require dc stability in the NDR region or a new type of RTD that provides a wider NDR region for greater ease of dc biasing in large-area diodes. The present oscillator approach makes it possible to bias the RTD in a positive-differential-resistance (PDR) region so that dc bias stability can be easily achieved.

## Relaxation Oscillator

The new RTD oscillator is based on the repetitive switching through the NDR region between dc-stable points lying below the peak point and above the valley point. To establish this type of oscillation, we imagine that the RTD is connected to one end of a short-circuited transmission line, as shown in Fig. 1. The transmission line has a characteristic impedance $Z_0$ and an electrical time delay $t_d$. The RTD is biased through a bias resistor $R_L$ with a supply voltage $V_B$. The quiescent operation point is initially just below the peak or just above the valley, and the RTD is induced to switch toward the valley or peak, respectively, by a slowly applied voltage ramp $\Delta V$. Once the first switch occurs, a pulse travels down the line, is reflected from the short with inverted polarity, and arrives back at the RTD after a time $2t_d$. If $2t_d$ is sufficiently greater than the RTD switching time $t_s$, then the return pulse will induce the RTD to switch back to the initial operating point. The subsequent return pulse then induces a switch similar to the first one, and the process repeats at a rate of $(4t_d)^{-1}$. The overall process is classified as a relaxation oscillation because the RTD dwells in either of its PDR regions between switching events.

*OSA Proceedings on Ultrafast Electronics and Optoelectronics, 1993, Vol. 14*
*Jagdeep Shah and Umesh Mishra (eds.)*
*© 1993 Optical Society of America*

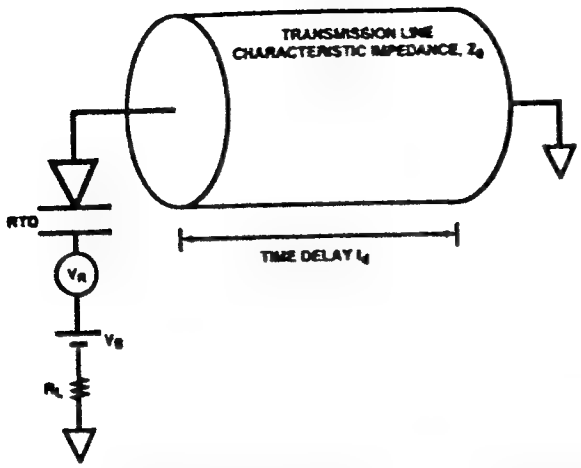


Fig. 1. Schematic diagram of the resonant-tunneling transmission-line relaxation oscillator.

## Device Models

To demonstrate the operational characteristics of the oscillator, we have simulated it numerically using the program SPICE3E. The transmission line is represented by the standard SPICE3 model, which is lossless and dispersionless. The RTD is represented by the parallel combination of a nonlinear voltage-controlled current generator and a nonlinear capacitance. The voltage dependence of the current generator is designed to be an accurate physical representation of the RTD, taking advantage of the transcendental functions available in SPICE3E. The current-voltage (I-V) characteristic of the RTD is assumed to have the form

$$I = c_1 V \left[\tan^{-1}(c_2 V + c_3) - \tan^{-1}(c_2 V + c_4)\right] + c_5 V^m + c_6 V^n ,$$

where the constants $c_1$ through $c_4$ are determined by the turn-on voltage, peak voltage, peak current, and peak differential conductance of the RTD, and the constants $c_5$ and $c_6$ are determined after obtaining $c_1$ through $c_4$ by fitting to the valley current and one arbitrary point beyond the valley. The exponents m and n (n > m) are chosen to obtain a satisfactory fit to the overall I-V curve beyond the valley point. The two $\tan^{-1}$ terms occur in the stationary-state tunneling theory of the RTD, with a Lorentzian form used for the transmission probability and a degenerate electron population assumed on the cathode side of the resonant-tunneling structure. The two polynomial terms account for the excess current, which is the primary current component beyond the valley point. The capacitance of the RTD is represented by the SPICE model for a back-biased junction diode, $C = C_0[1 + V/V_j]^{-1/2}$, where $C_0$ is the zero-bias capacitance and $V_j$ is the built-in potential. The diode reverse saturation current is made negligibly small.

Shown in Fig. 2 is the I-V curve simulated here. It applies to a 4-$\mu m^2$ RTD having a peak current density of $1.8\times10^5$ A $cm^{-2}$ and a specific capacitance at the peak of 1.4 fF $\mu m^{-2}$. The model I-V curve

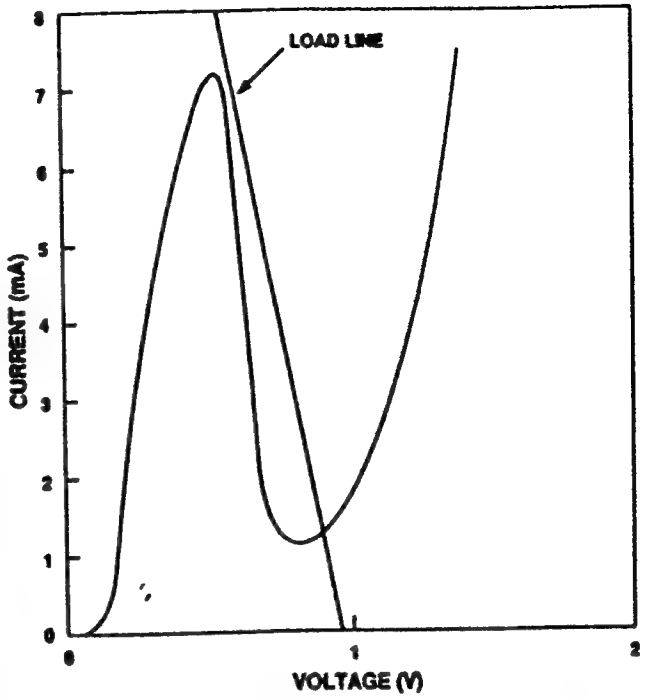


Fig. 2. Current-voltage characteristic of RTD modeled as relaxation oscillator. The straight line shows the dc load line presented to the RTD after the application of the start-up ramp.

has the parameters $c_1 = 0.0052$, $c_2 = 24.5$, $c_3 = 5.0$, $c_4 = 15.0$, $c_5 = 0.0000809$, $c_6 = 0.0014$, m = 1, and n = 5. The resulting peak-to-valley current ratio PVCR is 6.3, which is equal to the highest room-temperature PVCR obtained with GaAs/AlGaAs RTDs (i.e., GaAs quantum wells and AlGaAs barriers) but is sub-standard for $In_{0.53}Ga_{0.47}As/AlAs$ RTDs. The capacitance parameters are $C_0 = 14.0$ fF and $V_j = 0.1$ V, which yields C = 5.5 fF at the peak voltage.

## Numerical Results

The voltage difference across the RTD is shown in Fig. 3 for four different transmission-line delays under the conditions $Z_0 = 50\ \Omega$, $R_L = 50\ \Omega$, and $V_B = 0.75$ V. The amplitude and duration of the start-up ramp are 0.2 V and 10 ps, respectively. In Fig. 3(a), we see that $t_d = 0.9$ ps yields a single switching event followed by ringing around the valley point of the RTD. The smallest $t_d$ for which the switching is persistent is approximately 1.0 ps. In this case the waveform is quasi-sinusoidal, as shown in Fig. 3(b). Oscillatory behavior is also observed with the longer times of 3 ps in Fig. 3(c) and 10 ps in Fig. 3(d). However, it is apparent from the latter waveforms that with increasing delay time the RTD voltage resembles a square wave. The minimum and maximum voltage levels of the square wave represent the dwell of the RTD voltage below and above the peak and valley points, respectively.

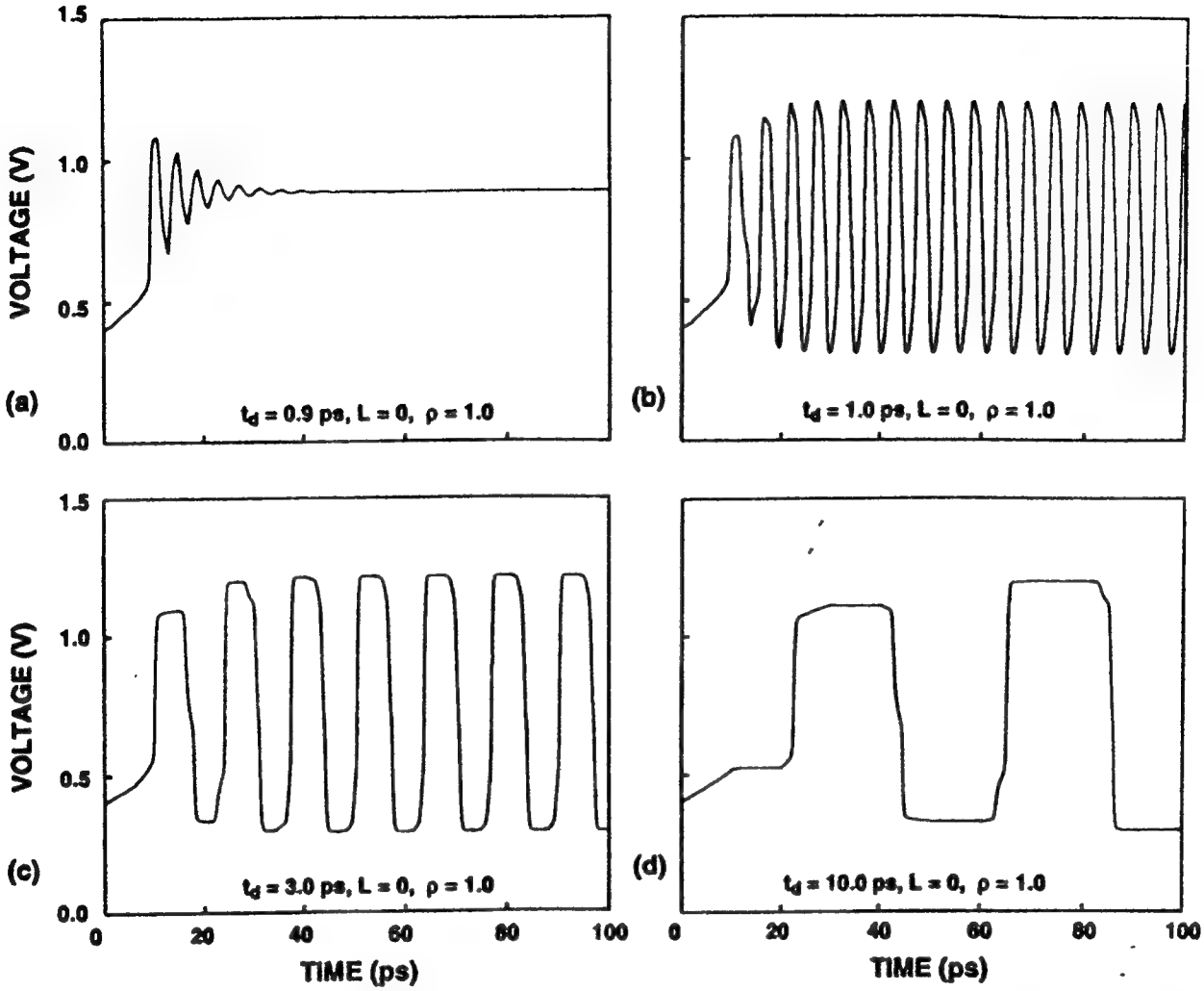


Fig. 3. Relaxation oscillator waveforms of voltage difference across the RTD for various transmission-line delays: (a) $t_d$ = 0.9 ps, (b) $t_d$ = 1.0 ps, (c) $t_d$ = 3 ps, (d) $t_d$ = 10 ps.

The output voltage waveforms across $R_L$ are shown in Fig. 4 for the same electrical delays. For $t_d$ = 1.0 ps in Fig. 4(b), we find a quasi-sinusoidal waveform at a frequency of 192 GHz and a power of 0.5 mW. However, it is apparent from Figs. 4(c) and 4(d) that the oscillator output waveform becomes highly non-sinusoidal with increasing delay time. The waveform consists of a sequence of pulses having a full width at half-maximum of 1.9 ps and repetition time of approximately $4t_d$. During the repetition period two pulses occur having opposite polarities. These pulses represent the two switching events required to complete one cycle around the dynamic load line of the RTD. For both polarities, the pulse width is somewhat greater than the 10-90% switching time $t_R$ of the RTD between the peak and valley points. An analytic expression for $t_R$ is given by $4.4\Delta VC/\Delta I$, where $\Delta V$ is the difference between the valley and peak voltages, C is the capacitance at the peak point, and $\Delta$ I is the difference between the peak and valley currents [3]. For the present RTD we have $\Delta V$ = 0.28, $\Delta I$ = 6.0 mA, and C = 5.5 fF, so that $t_R$ = 1.1 ps. The difference between $t_R$ and the relaxation oscillator pulse width is caused by the fact that the oscillator switches over a wider voltage range, between the peak and a point approximately 0.4 V beyond the valley.

## Non-Ideal Transmission Line

Two important practical issues concerning this oscillator are the degree to which the power reflection from the short-circuited end of the transmission line can deviate from unity and the sensitivity of the oscillator to the form of the start-up ramp. To address the first issue the short circuit was replaced with a load resistor whose resistance $R_T$ was increased up to the point where oscillations were just maintained. This defines a minimal power reflection $\rho = [(R_T - Z_0)/(R_T + Z_0)]^2$. For the 1.0, 3.0, and 10.0 ps delays, the minimal power reflections were 97, 69, and 59%, respectively. To address the second issue,

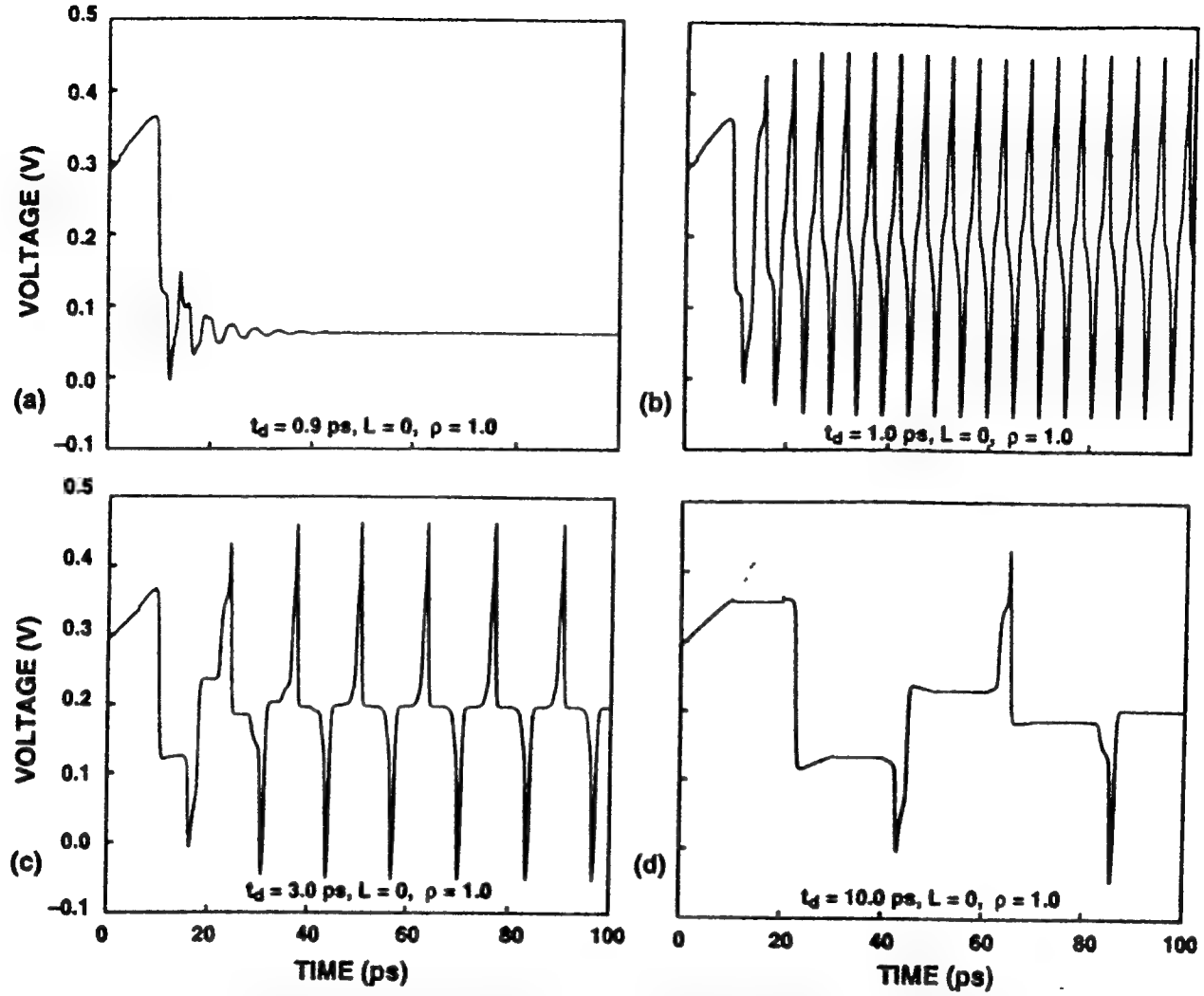


Fig. 4. Relaxation oscillator waveforms of voltage across the load resistor for various transmission-line delays: (a) $t_d$ = 0.9 ps, (b) $t_d$ = 1.0 ps, (c) $t_d$ = 3 ps, (d) $t_d$ = 10 ps.

the start-up ramp duration was increased from 10 ps to 1 ns in several steps. In all cases the steady-state waveforms were practically identical, proving that the only role of the start-up ramp is to trigger the first switching event. No energy is required from the ramp to sustain the oscillations.

## Conclusion

In conclusion, a new oscillator is proposed that entails the repetitive switching of an RTD connected to a short-circuited transmission line. When the electrical delay of the line is much greater than the RTD switching time, the oscillator generates a pulse train having a repetition rate equal to $(4t_d)^{-1}$ and a pulse width equal to $t_s$. When the electrical delay is comparable to the switching time, the oscillator output is quasi-sinusoidal. Consequently, the relaxation oscillator is a compact electrical design that can function either as a picosecond pulse generator or as a high-frequency cw source.

## Acknowledgements

The author thanks J. P. Mattia for assistance with the numerical simulations, R. A. Murphy for useful comments on the manuscript, and C. L. Dennis, M. W. Geis and M. J. W. Rodwell for technical discussion. This work was sponsored by the Air Force Office of Scientific Research.

## References

1. E. R. Brown, J. R. Söderström, C. D. Parker, L. J. Mahoney, K. M. Molvar, and T. C. McGill, *Appl. Phys. Lett.*, 58, 2291 (1991).
2. J. F. Whitaker, G. A. Mourou, T. C. L. G. Sollner, and W. D. Goodhue, *Appl. Phys. Lett.*, 53, 385 (1988).
3. E. R. Brown, C. D. Parker, T. C. L. G. Sollner, A. R. Calawa, M. J. Manfra, C. L. Chen, S. W. Pang, and K. M. Molvar, *Proc. SPIE*, 1288, 122 (1990).

# Resonant tunneling through mixed quasibound states in a triple-well structure

E. R. Brown, C. D. Parker, A. R. Calawa, and M. J. Manfra
*Lincoln Laboratory, Massachusetts Institute of Technology, Lexington, Massachusetts 02173-9108*

(Received 24 July 1992; accepted for publication 15 January 1993)

A triple-well resonant-tunneling structure made from the $In_{0.53}Ga_{0.47}As$/AlAs material system yields a broad negative differential resistance (NDR) region without the precipitous drop in current that occurs in single-well structures. This NDR characteristic is attributed to resonant tunneling through mixed quasibound states. A diode made from this structure is used to generate a nearly constant power of 0.5 mW up to 16 GHz.

Resonant tunneling continues to attract practical interest since it is a transport process that provides a high-speed negative differential resistance (NDR) with very high peak current density $J_P$ and useful peak-to-valley current ratio at room temperature. The device used for the majority of applications has been the single-well (double-barrier) resonant-tunneling diode (RTD). A characteristic shared by nearly all single-well RTDs is the steep NDR region just above the peak voltage. While this characteristic is beneficial in switching applications,[1] it is often detrimental to analog applications such as oscillators. In this letter we demonstrate a triple-well RTD having a more gradual NDR region. Originally we designed this RTD to see if high $J_P$ could be obtained in multiple-well structures and to search for new resonant-tunneling effects. Our numerical simulations showed that high $J_P$ was possible by successively decreasing the well widths between the cathode and anode sides of the structure. This approach was proposed several years ago by Summers and Brennan.[2] In their structures the width of adjacent quantum wells was much different, leading to a distinct peak in the current-voltage ($I$-$V$) curve for each quasibound level in the structure. In the present structure adjacent wells are much closer in width, resulting in a strong interaction, or mixing, between quasibound states.

The diodes were fabricated from a wafer containing epitaxial layers of $In_{0.53}Ga_{0.47}As$ and AlAs on a $n^+$-InP substrate. The layers were grown by molecular beam epitaxy at 500 °C. The $In_{0.53}Ga_{0.47}As$/AlAs material system was chosen in lieu of the more common GaAs/$Al_xGa_{1-x}As$ system because of its superior resonant-tunneling properties. The tunneling structure consists of four undoped, 1.4-nm-thick AlAs barriers separated by three undoped $In_{0.53}Ga_{0.47}As$ quantum wells of graded width. Starting from the bottom (or substrate) side, the widths of the quantum wells are 4.0, 4.6, and 5.2 nm. Outside of the tunneling structure are lightly doped ($N_D = 2\times10^{16}$ cm$^{-3}$) spacer layers of thickness 50 and 10 nm on the bottom and top sides, respectively. Outside of the spacer layers are thick $n^+$ regions doped to $N_D = 1\times10^{18}$ cm$^{-3}$. The latter regions serve as the top and bottom contacts. Mesas were fabricated by defining 8-$\mu$m-square metal pads on the top surface and wet etching to approximately 0.1 $\mu$m below the tunnel structure using a $H_3PO_4$-based solution. Electrical contact was made to the top pad by a fine wire and to the bottom of the wafer by soldering.

The experimental room-temperature $I$-$V$ curve obtained by conventional wafer probing is shown in Fig. 1(a). Negative bias voltage was applied to the top contact, and the solid and dashed lines represent dc-stable and dc-unstable regions, respectively. The $I$-$V$ curve has three current peaks near bias-voltage magnitudes $V_B$ of 1.6, 2.6, and 3.5 V, and labeled A, B, and C, respectively. The current density at peak A is $1.1\times10^4$ A cm$^{-2}$, which is very close to the theoretical value calculated below. At least two closely spaced NDR regions are apparent, containing broad plateaus centered at approximately 1.8 and 2.7 V. A dc-stable positive-resistance region [labeled D in Fig. 1(a)] appears between the A and B current peaks. With positive bias applied to the top contact, the $I$-$V$ curve displays three well-separated current peaks with only the second peak having a substantial NDR region. The positive-biased $I$-$V$ curve is less interesting than the negative-biased curve and thus will not be discussed further.

In double-barrier RTDs, a plateaulike structure in a NDR region is usually indicative of oscillations occurring between the diode and the measurement circuit. To ascertain the nature of the NDR plateaus in the present diode, we mounted an $8\times8$ $\mu$m device in a coaxial package and induced oscillations with a double-stub tuner connected between the diode package and a microwave spectrum analyzer. Oscillations were observed in the NDR plateaus above current peaks A and B that were similar to the oscillations in single-well RTDs, having a power of a few $\mu$W and a frequency that varied greatly with the adjustment of the tuner. However, much more powerful oscillations were observed in the intermediate region D. The most powerful oscillations in this region were 0.44 mW at 4.92 GHz, 0.53 mW at 12.2 GHz, and 0.46 mW at 16.3 GHz. The small change of power with frequency suggests that the maximum frequency at which these oscillations can occur is very high.

The fact that the device oscillates at all values of $V_B$ between 1.6 and 2.9 V indicates that the intrinsic $I$-$V$ curve (i.e., the $I$-$V$ curve measured in the absence of oscillation) of this device may contain a NDR region over this entire range. To investigate this possibility, we replaced the coaxial tuner with an attenuator mounted in close proximity to the device to eliminate the circuit resonances. The resulting $I$-$V$ curve is shown in Fig. 1(b) and displays a nearly continuous NDR region between 1.6 and 2.9 V. The roughness just above the current peak at 1.6 V is thought


© 1993 American Institute of Physics


APPENDIX F

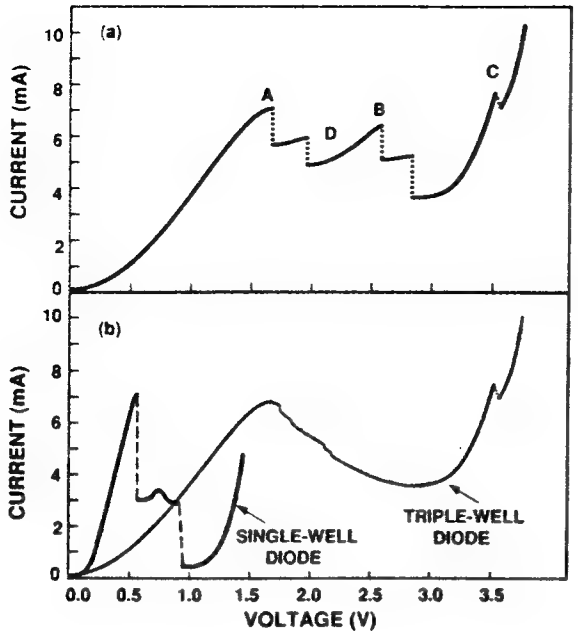


FIG. 1. (a) Room-temperature $I$-$V$ curves of the triple-well RTD. The dashed regions represent discontinuous transitions resulting from self-rectification of oscillations occurring in the NDR regions. (b) $I$-$V$ curve of the same triple-well RTD as in (a) but mounted in a coaxial package configured to suppress oscillations up to at least 22 GHz. The $I$-$V$ curve of a single-well RTD having nearly the same peak current is also shown for comparison.

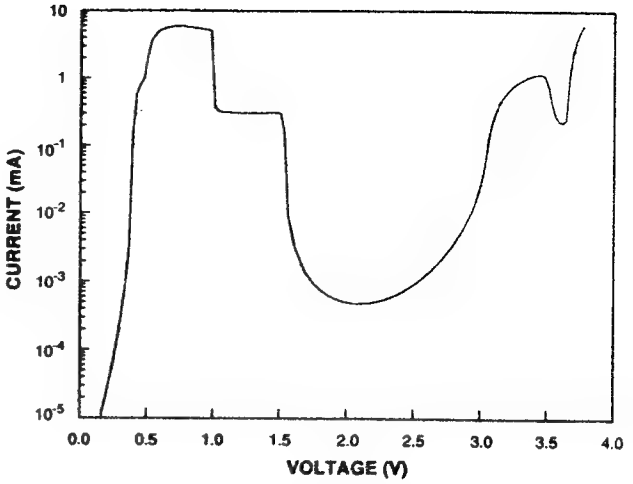


FIG. 2. Theoretical $I$-$V$ curve of the triple-well RTD, as computed from a stationary-state model of resonant tunneling. The chairlike structure between 1.1 and 1.5 V is caused by resonant tunneling through mixed quasibound states of adjacent quantum wells in the structure.

to be caused by oscillations occurring at frequencies well above the 22-GHz frequency limit of the spectrum analyzer. The 1.3-V width of the NDR region in Fig. 1(b) is significantly greater than that of typical single-well RTDs. For example, Fig. 1(b) shows the 0.4-V-wide NDR region of a single-well RTD having nearly the same $J_P$ and cladding-layer doping profile as the present device.

To understand the physical cause of the broad NDR region, we have simulated the electrical current through the triple-well structure using a stationary-state model. In this model the current in each longitudinal energy interval, $\Delta E_L$, is the product of the quantum-mechanical coherent transmission probability $T^*T$ through the structure and the supply function $S(E_L)\Delta E_L$ of electrons on the cathode side.[3] The resulting $I$-$V$ curve for the triple-well structure with negative bias applied to the top contact is shown in Fig. 2. A prominent feature of this curve is the chairlike structure extending between 1.0 and 1.5 V. This behavior is quite unlike anything seen in the theoretical $I$-$V$ curves of single-well RTDs. As discussed next, it can be explained by the effect of resonant tunneling through two closely spaced levels.

The chairlike structure is analyzed by examining separately computed curves of $T^*T$ and $S(E_L)$ vs bias voltage. In computing these quantities, we assumed that the electric field across the tunnel structure is uniform, the zero of energy is at the conduction band edge on the cathode side, and the electron Fermi distribution on the cathode side is degenerate. The dependence of $T^*T$ and $S(E_L)$ upon energy for several values of $V_B$ is shown in Fig. 3. At zero bias [Fig. 3(a)], $T^*T$ displays a triplet of peaks corresponding to the quasibound-state energies for the 4.0-, 4.6-, and 5.2-nm wells of $E_{1,1}=0.143$ eV, $E_{1,2}=0.170$ eV, and $E_{1,3}=0.204$ eV, respectively (the symbol $E_{m,n}$ denotes the $m$th quasibound level in the $n$th quantum well from the cathode side). With increasing bias, $E_{1,3}$ drops most rapidly, followed by $E_{1,2}$ and $E_{1,1}$. With just a small bias of $V_B=0.39$ [Fig. 3(b)], the three states approach a point of minimum energy separation and high combined transmission probability. However, practically no current flows at this bias because of the small overlap between $T^*T$ and $S(E_L)$.

At $V_B=0.96$ V [Fig. 3(c)], corresponding to the current peak in Fig. 2, the overlap between $T^*T$ and $S(E_L)$ is large, and the separation between transmission peaks is much greater than at lower voltages because the bias electric field has caused the levels to interchange their order in energy. The dominant transmission peak associated with

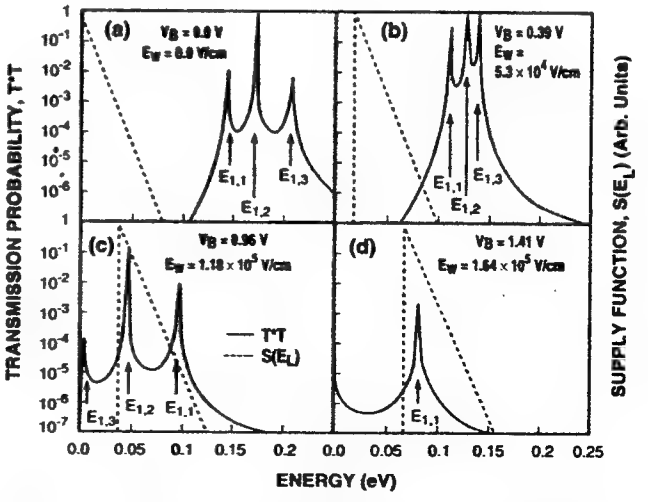


FIG. 3. Transmission probability (solid curve) and supply function (dashed curve) for the triple-well RTD at specific bias voltages across the active region of the device. (a) $V_B=0.0$, (b) $V_B=0.39$ V, (c) $V_B=0.96$ V, and (d) $V_B=1.41$ V. A uniform electric field $E_W$ was assumed to exist across the triple-well structure.

$E_{1,2}$ is approaching the lower edge of the supply function, which explains the sharp drop at 1.1 V in Fig. 2. Between 1.1 and 1.6 V, the transmission through the structure acquires a dual character as mixing between the quasibound states causes the probability of resonant tunneling through $E_{1,2}$ to decrease and the probability through $E_{1,1}$ to increase. The same type of mixing occurs between $E_{1,2}$ and $E_{1,3}$ at a lower bias field [cf. Fig. 3(b)], but the overlap between $T^*T$ and $S(E_L)$ is so slight that there is no discernible effect in the $I$-$V$ curve. At the highest $V_B$ of 1.41 [Fig. 3(d)], the only transmission peak of the triplet that remains within the supply function is $E_{1,1}$. With a further increase in bias, this peak drops below the supply function giving rise to the sharp drop in Fig. 2 at 1.6 V. The sharp drops at 1.1 and 1.6 V result from the narrowness of the quasibound-state transmission resonances for the two levels in the coherent model. Experimentally these resonances are greatly broadened by scattering processes in the structure. The broadening has the effect of smearing out the sharp transitions and rendering a smoother $I$-$V$ curve like the experimental one in Fig. 1(b).

Two other essential features of the theoretical $I$-$V$ curve are explained by the behavior of $T^*T$. The small undulation in Fig. 2 just below 0.5 V is caused by the drop of $E_{1,3}$ below the supply function. A NDR region is not observed because of the small peak magnitude of $T^*T$ through $E_{1,3}$ at this bias. The NDR region between 3.4 and 3.6 V in Figs. 1 and 2 is caused by resonant tunneling through $E_{2,3}$. Although the peak transmission through this level is small, the NDR region is easily observed because of the large transmission width.

An interesting by-product of the analysis is the close agreement between the experimental and theoretical peak currents in Figs. 1 and 2. This is reminiscent of the favorable comparison of these quantities in single-well RTDs. In the single-well case, it was argued that the inelastic scattering neglected by the coherent model greatly reduces the peak transmission but leaves the integrated transmission unchanged.[4,5] This means that the peak current is also unchanged if the width of the transmission probability function in the presence of scattering remains less than the Fermi energy on the cathode side of the structure. The same argument carries over to the multiple-well structures since the physical basis for the argument—the Breit–Wigner formalism of inelastic scattering—also applies to these structures. However, as in the single-well case, the neglect of scattering in the coherent model leads to a significant underestimation of the current at the valley points.

The broadened NDR region of the triple-well RTD is beneficial for oscillator applications because it facilitates dc biasing and allows for greater output power in a given resonant circuit. To demonstrate this, we compared the oscillator performance of the triple-well RTD with that of the single-well RTD of Fig. 1(b). The single-well RTD has the same doping profile below the barriers as the triple-well device, so that the electric field across the barriers at a given bias voltage is nearly the same. The experimental results are shown in Fig. 4. Both devices were mounted in the same 50-Ω coaxial resonator for oscillations up to 20

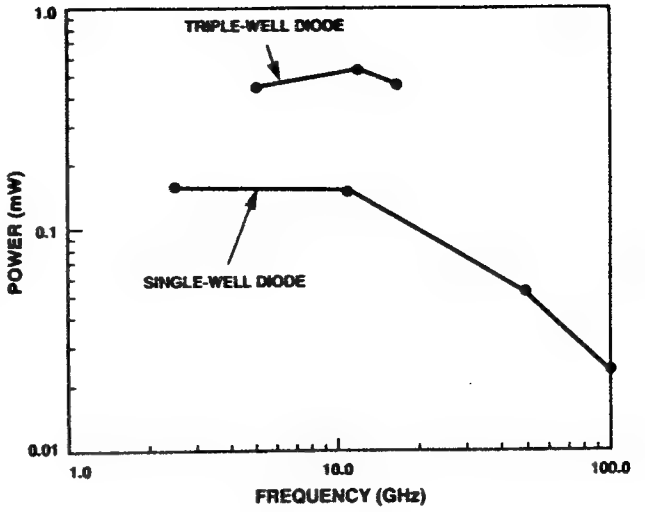


FIG. 4. Oscillation power of the triple-well and single-well RTDs having the $I$-$V$ curves in Fig. 1(b).

GHz, and the results shown for the single-well RTD at higher frequencies were obtained separately in a waveguide resonator. Near 10 GHz the triple-well RTD generates an output power that is nearly 4 times greater. We have also investigated parallel arrays of these diodes to increase the output power to values well above 1 mW. To date, the highest power obtained from such an array is 5 mW near 1.2 GHz.[6]

In conclusion, we have demonstrated an enhanced NDR effect in a triple-well RTD that we attribute to resonant tunneling through mixed quasibound levels. This effect is characterized by a broad NDR region which lacks the precipitous drop in current that occurs in single-well RTDs. This NDR characteristic is useful for oscillators and other analog devices. The keen understanding of resonant tunneling acquired through research on single-well structures combined with the steady improvement in heterostructure materials now makes this type of multiple-well RTD practical at room temperature.

The authors acknowledge K. M. Molvar for assistance in fabrication, D. L. Landers for help in dicing and bonding, R. A. Murphy for helpful comments, and A. L. McWhorter for a thorough critique of the manuscript. This work was sponsored by the Air Force Office of Scientific Research, the Army Research Office, and NASA.

[1] E. Özbay and D. M. Bloom, IEEE Electron Device Lett. **12**, 480 (1991).
[2] C. J. Summers and K. F. Brennan, Appl. Phys. Lett. **48**, 806 (1986).
[3] C. B. Duke, *Tunneling in Solids*, Solid State Physics (Academic, New York, 1969).
[4] T. Weil and B. Vinter, Appl. Phys. Lett. **50**, 1281 (1987).
[5] M. Büttiker, IBM J. Res. Dev. **32**, 63 (1988).
[6] K. D. Stephan, S. C. Wong, E. R. Brown, K. M. Molvar, A. R. Calawa, and M. J. Manfra, Electronics Lett. **28**, 1411 (1992).

# Resonant-Tunneling Transmission Lines

C. L. Dennis, E. R. Brown, and S. Prasad*
Lincoln Laboratory, Massachusetts Institute of Technology
Lexington, MA 02173-9108

*Department of Electrical and Computer Engineering
Northeastern University, Boston, MA 02115

The application of quantum-effect devices in digital circuits is presently of great interest for computing and signal processing. The central principle of these devices is multistable operation by way of negative-differential resistance (NDR). This paper deals with a bistable quantum-effect device consisting of resonant-tunneling structures monolithically integrated with high-frequency transmission lines as a basis for digital logic and waveforming applications. The key advantage of the device over conventional logic approaches is that the nonlinear switching elements couple directly to a quasi-TEM mode of the transmission line. This greatly reduces the deleterious effects of interconnects, which can easily limit the speed of quantum-effect devices in a conventional circuit because of their relatively low current density.

Figure 1 illustrates how bistability is achieved in the proposed structure. Figure 1(a) shows a classic configuration of a resonant-tunneling diode (RTD) and a load resistor. In Fig. 1(b) we see that the loadline intersects the RTD I-V curve at three points. The two points where the RTD has a positive-differential resistance (I and III) are unconditionally stable, while the one in the NDR region (II) is ac unstable. For ease of monolithic integration, a bistable circuit made only of RTDs is desirable. One such configuration, shown in Fig. 1(c), utilizes RTDs of two different sizes, a large one as the switching element and a small one as the load resistor. The theoretical I-V curve is shown in Fig. 1(d). Greater voltage swing and lower static power dissipation are achieved with the configuration shown in Fig. 1(e). In this case, a different supply voltage is chosen, and the theoretical I-V curves are shown in Fig. 1(f).

We seek to construct two very different kinds of circuits, which are illustrated in Fig. 2. The first, shown in Fig. 2(a), is an inherently bistable transmission line which could be used in high-speed digital applications as a low-loss interconnect or possibly for pulse-shaping applications. The results of a SPICE simulation of the bistable transmission line are presented in Fig. 3. A 5-GHz sine wave is transformed into a square wave of the same period and comparable amplitude after passing through ten stages of the transmission line.

The second circuit of interest is shown in Fig. 2(b). It is a relaxation oscillator [1], which depending on its configuration can be used either as a clock for high-speed digital systems, as a coherent source of millimeter wave power, or as a picosecond impulse generator. Because of the variety and scope of the circuits possible, we label all of these structures as resonant-tunneling transmission lines or $RT^2L$.

This paper focuses on modeling and design of $RT^2L$ devices in the GaAs/AlGaAs materials system. Progress will be reported on the fabrication and testing of the $RT^2L$ structures on a 3-inch GaAs substrate.

[1] E. R. Brown, "Resonant-Tunneling Transmission-Line Relaxation Oscillator," OSA Proceedings on Ultrafast Electronics and Optoelectronics, J. Shah and U. Mishra, eds. (Optical Society of America, Washington, DC, 1993), Vol. 14, pp. 91-94.

This work is sponsored by the Lincoln Laboratory Advanced Concepts Program, principally sponsored by the Department of the Air Force.

Fig. 1(a)

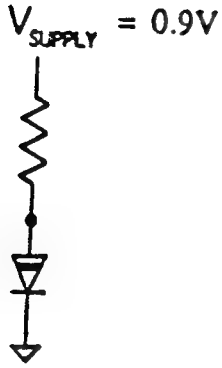


Fig. 1(b)

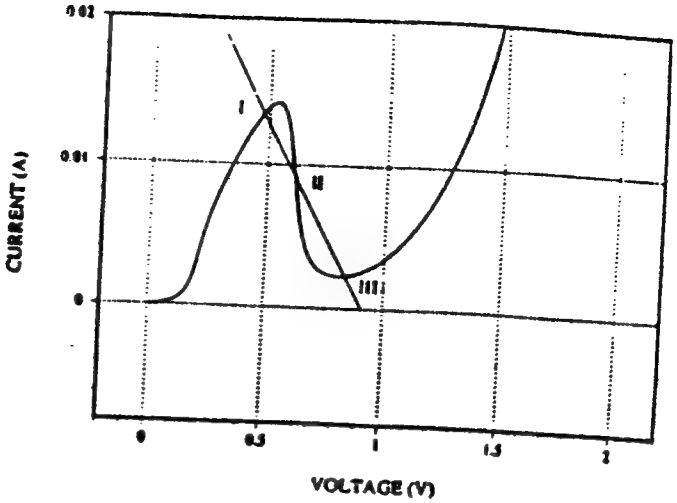


Fig. 1(c)

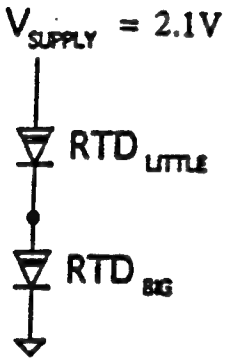


Fig. 1(d)

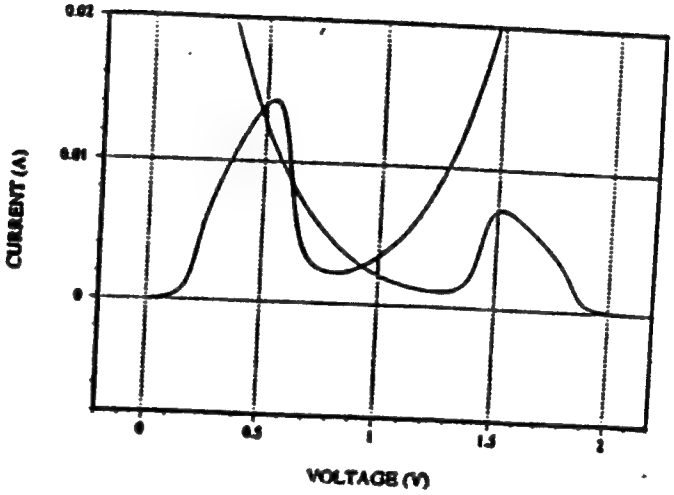


Fig. 1(e)

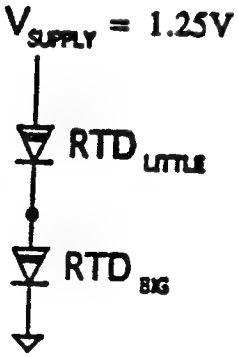


Fig. 1(f)

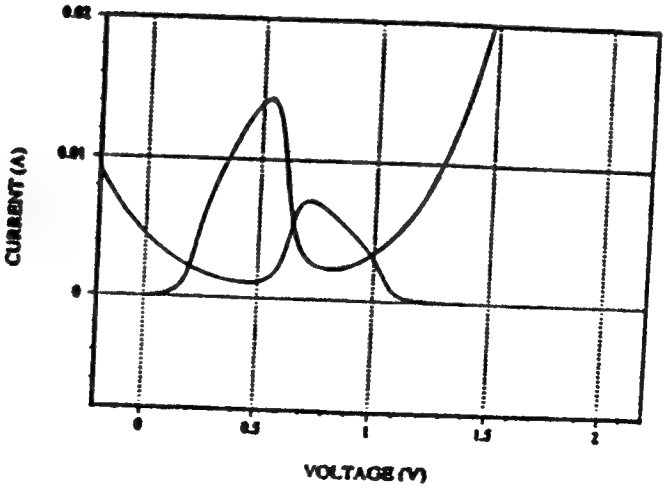


*Figure 1. Circuit configurations and I-V characteristics for achieving bistability with resonant-tunneling diodes.*

Fig. 2(a)

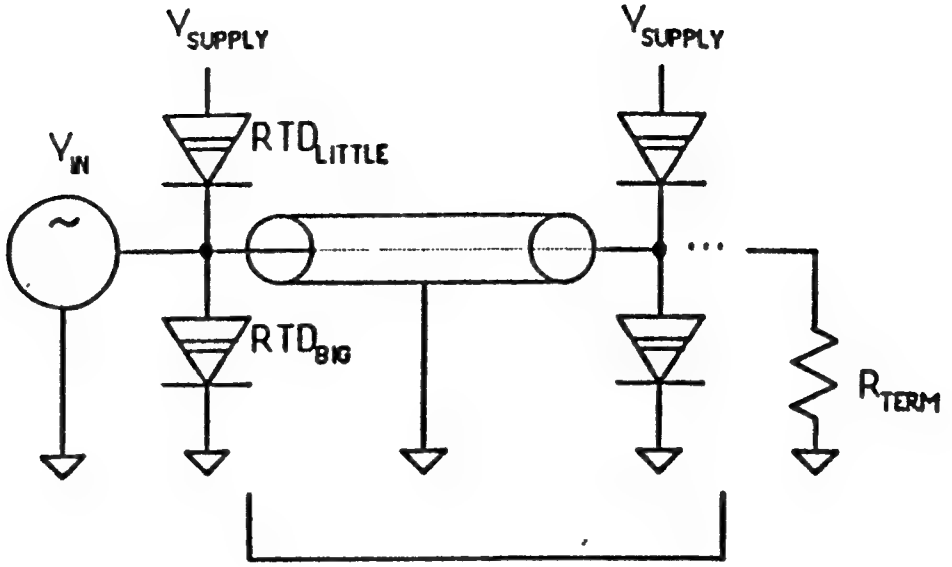


Fig. 2(b)

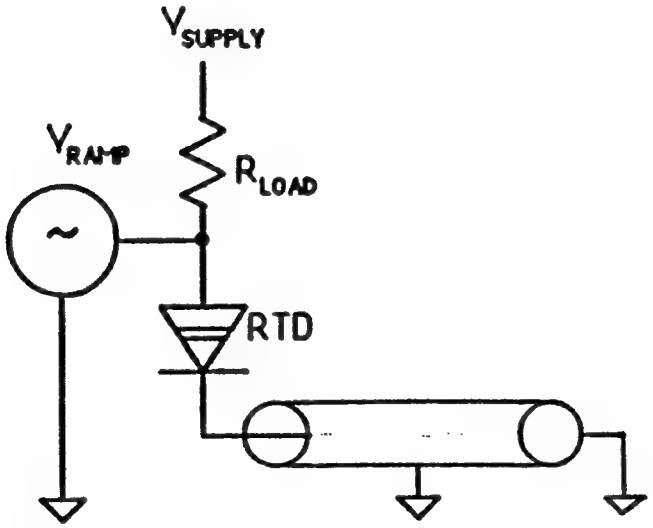


*Figure 2. Circuit schematics for two $RT^2L$ devices. (a)A bistable transmission line suitable for logic interconnect or pulse shaping. (b)A relaxation oscillator whose frequency is determined by the round trip time from the RTD to the short.*

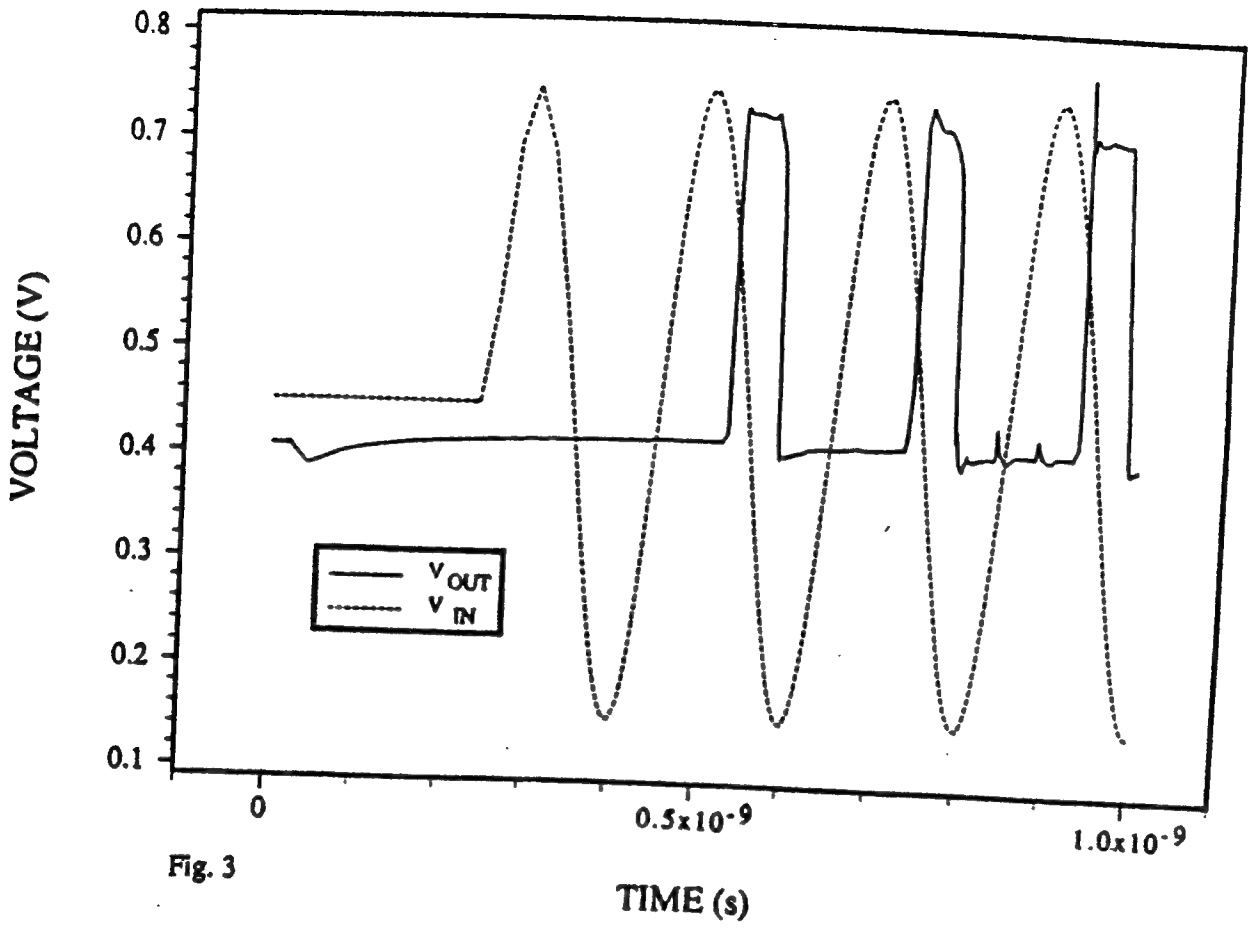


Fig. 3

*Figure 3. A SPICE simulation of an $RT^2L$ transmission line structure showing a pulse shaping application.*

# Chapter 10

# High-Speed Resonant-Tunneling Diodes

E. R. BROWN

Lincoln Laboratory
Massachusetts Institute of Technology
Lexington, Massachusetts 02173-9108

I. Introduction 306
A. Overview 306
B. Historical Background 307
II. Physical Concepts in Resonant Tunneling 308
A. Resonant-Tunneling Conditions 308
B. Transmission Probability 309
C. Electrical Current and NDR 311
III. Resonant-Tunneling Materials 312
A. Material System Properties 312
B. GaAs-Based Structures 314
C. $In_{0.53}Ga_{0.47}As$-Based Structures 315
D. InAs-Based Structures 316
E. GaSb and InSb Structures 318
F. Column IV Material Systems 318
IV. DBRTD Device Physics 319
A. Band Bending and Diode Capacitance 319
B. Current Density 321
C. Quantum Well Charge Storage 323
D. Current Fluctuations 325
E. Excess Current 326
V. Time-Delay Mechanisms 328
A. Fundamental *RC* Limit 328
B. Resonant-Tunneling Traversal Time 328
C. Depletion-Layer Transit Time 329
VI. High-Speed Performance Characteristics 330
A. Small-Signal Impedance Model 330
B. Maximum Oscillation Frequency 332
C. Switching Time 333



Heterostructures and Quantum Devices



Reprinted with permission of MIT Lincoln Laboratory, Lexington, MA.

VII. High-Speed Experimental Results 334
A. Oscillations 334
B. Small-Signal Impedance 337
C. Electro-optic Measurements of Switching Time 337
D. Microwave Noise Power Spectrum 339
VIII. Survey of High-Speed Applications 341
A. Device Qualifications 341
B. DBRTD Quasioptical Oscillator 342
C. DBRTD Pulse-Forming and Trigger Circuits 343
D. DBRTD-Based Waveform Generation and Signal Processing Circuits 344
E. DBRTDs in Memory and Logic Circuits 344
References 347

## I. INTRODUCTION

### A. Overview

Tunneling is a strictly quantum mechanical process that entails the passage of a particle from one classically allowed region to another through a classically forbidden, or tunneling, region. Resonant tunneling is distinguished by the presence within the classically forbidden region of quasibound, or metastable, states of the tunneling particle. In solid-state resonant tunneling, the quasibound states are usually associated with impurities in the tunneling region or with narrow classically allowed regions (i.e., quantum wells) contained within semiconductor heterostructures. The present chapter is concerned with resonant tunneling in the double-barrier heterostructure, which is composed of two layers of a semiconductor material, such as AlAs, embedded in another semiconductor having a smaller bandgap, such as GaAs.

Double-barrier resonant tunneling has attracted considerable attention because it is one of the few solid-state transport phenomena that can provide a fast negative differential resistance (NDR) at room temperature. The NDR region has been used as the basis for high-frequency oscillations and high-speed switching. For example, double-barrier resonant-tunneling diodes (DBRTDs) made from the InAs/AlSb material system have oscillated up to 712 GHz, and DBRTDs made from the GaAs/AlAs system have switched from the peak-current point to the valley-current region in a time near 2 ps. Much of the interest in resonant-tunneling devices stems from the fact that these results are among the highest oscillation frequencies and the lowest switching times reported to date for electronic devices. This has led to the development of DBRTD oscillators

for the terahertz region and DBRTD switches for signal processing and digital applications.

The outline of this chapter is as follows. Section II reviews the fundamental physical characteristics of resonant tunneling. Section III deals with the various resonant-tunneling material systems and the dc $I$–$V$ characteristics obtained from DBRTDs in these systems. These include III–V material systems having type I band offsets, such as the common GaAs/AlAs (GaAs quantum well and AlAs barriers); those having type II offsets, such as InAs/AlSb; pseudomorphic systems, such as $In_xGa_{1-x}As$/AlAs; and column IV systems, such as $Si_xGe_{1-x}$/Si. Section IV covers some of the key issues in the device physics, such as the current density, charge storage in the quantum well, current fluctuations, and excess current mechanisms. Section V analyzes the important time-delay mechanisms operative in high-speed diodes, including the fundamental $RC$ time, resonant-tunneling traversal time, and semiclassical transit time across the depletion region. In Section VI, these time delays are combined to yield the two most important theoretical measures of device performance: the maximum oscillation frequency $f_{max}$ and the switching rise time $t_R$. Section VII summarizes some of the experimental methods, both electronic and optoelectronic, that have been employed to characterize the speed of the DBRTD. Among these methods are oscillator-frequency measurement and switching-time measurement by electro-optic sampling. The last section surveys some promising analog and digital applications of DBRTDs. Each of the applications utilizes the DBRTD as an independent device. The chapter does not address the integration of double-barrier structures into transistors, such as the resonant-tunneling bipolar transistor [1], the resonant-tunneling hot electron transistor [2], or the bipolar quantum-well resonant-tunneling transistor [3].

## B. Historical Background

In a sense the double-barrier structure represented a retreat from more complicated multiple-barrier, or superlattice, structures that initially promised new electronic functions, such as Bloch oscillations, but did not perform as expected [4,5]. The first realization of the double-barrier structure occurred in 1974 with the observation of NDR in a GaAs/AlGaAs DBRTD at low temperatures [6]. Following this pioneering result, most of the work in heterostructures centered around the development of molecular beam epitaxy (MBE), since it was clear that the quality of the materials in these structures would have to be improved in order to observe the NDR or any other quantum transport effect at room temperature. The

primary structures studied during this time were single-heterojunction devices or quantum wells rather than resonant-tunneling structures. The subsequent improvements in materials growth led to the advent of two very important devices: the heterojunction diode laser and the heterostructure field effect transistor (FET). However, the resonant-tunneling structure went relatively unstudied until 1983. At that time, a cooled GaAs/AlGaAs double-barrier structure was used to rectify 2.5-THz laser radiation [7]. This pivotal experiment demonstrated that resonant tunneling was a very fast process, and it spurred the development of improved materials. Within 3 years, several groups had achieved a large room-temperature NDR effect, first in the GaAs/$Al_{0.25}Ga_{0.75}As$ material system [8] and shortly thereafter in the GaAs/AlAs system [9,10].

In the ensuing years, the research has branched in different directions, with much of the effort aimed at developing new material systems or at understanding the dynamic characteristics of resonant tunneling. A key advance in material systems was the development of indium-bearing heterostructures, as discussed in Sections III.C and III.D. The research on the dynamic characteristics has centered around a set of oscillation and switching experiments, described in Section VII, and around the quantum transport theory, described in Chapter 9.

## II. PHYSICAL CONCEPTS IN RESONANT TUNNELING

### A. Resonant-Tunneling Conditions

The fundamental requirement for resonant tunneling in any structure is spatial quantization. This entails the formation of quasibound states whose energy can be found by solving the time-independent Schrödinger equation for the structure. Each state is characterized by a quasibound energy $E_n$ and a lifetime $\tau_n$. These quantities are related to the tunneling process in that $E_n$ is the $n$th peak of the transmission probability $T^*T$ versus longitudinal energy $E_Z$ (the energy along the direction perpendicular to the barriers); $\tau_n \approx \hbar/\Gamma_n$ where $\Gamma_n$ is the full width at half-maximum of the $n$th peak of the $T^*T$ curve. The requirement for spatial quantization is $E_n \gtrsim \hbar/\tau_s$, where $\tau_s$ is the inelastic scattering time for an electron occupying the $n$th state. In the limit of an infinitely deep quantum well where $E_n = (\hbar k_n)^2/2m^* = (n\pi\hbar)^2/2m^*L_W^2$, this inequality becomes $\tau_s \gtrsim 2L_W/n\pi v_g \equiv 2t_w/n\pi$, where $L_W$ is the quantum well width, $v_g = \hbar k_n/m^*$ is the group velocity, $m^*$ is the effective mass, and $t_w$ is the semiclassical traversal time. In other words, spatial quantization requires that the electron traverse the quantum well roughly once or more without scattering.

Resonant tunneling is also characterized by the relative magnitudes of $\tau_n$ and $\tau_s$. If $\tau_n < \tau_s$, the resonant tunneling through the $n$th state is said to be coherent, since under this condition the electron does not scatter during the process and thus the phase of the wave function at each point in space is continuous in time. If $\tau_n \gg \tau_s$, the resonant tunneling is said to be sequential. In this case, the wave-function phase is partially randomized by scattering events that occur in the double-barrier structure. Thus, resonant tunneling can be neatly classified by the three characteristic times, $\tau_n$, $t_w$, and $\tau_s$ [11,12]. Coherent resonant tunneling satisfies $\tau_n < \tau_s > t_w$, and sequential resonant tunneling satisfies $\tau_n > \tau_s > t_w$.

## B. Transmission Probability

Resonant tunneling can be analyzed within the stationary-state formalism of quantum mechanics. One can represent a particle incident on the double-barrier structure as a plane wave having a wave vector $k_z = (2m^*E_Z)^{1/2}/\hbar$ along the $z$ direction. The interaction of the particle with the double-barrier structure is described entirely by the transmission probability $T^*T(E_Z)$. In the situation where the energy in the lateral plane is conserved throughout the resonant-tunneling process, only those particles having $E_Z$ nearly equal to $E_n$ can traverse the structure with a significant probability. For these particles the transmission probability is approximated by the following Lorentzian form [12,13]:

$$T^*T = \frac{\Gamma_n^L \Gamma_n^R}{(E_Z - E_n)^2 + \Gamma_n^2/4}, \tag{1}$$

where $\Gamma_n^L$ and $\Gamma_n^R$ are the partial-width, or transparency, factors for the left and right barriers, respectively. In the presence of certain types of scattering, this expression can be generalized to the form

$$T^*T = \left[\frac{\Gamma_n^L \Gamma_n^R}{\Gamma_n^L + \Gamma_n^R}\right] \frac{\Gamma_T}{(E_Z - E_n)^2 + \Gamma_T^2/4}, \tag{2}$$

where $\Gamma_T = \Gamma_n^L + \Gamma_n^R + \Gamma_S$, and $\Gamma_S$ is a scattering parameter. In this case, $T^*T$ represents the probability for an electron to enter the structure at $E_Z$ and to exit at any energy. The scattering causes the energy of the particle to be uncertain after entering the structure. However, the integrated probability, $\int_0^\infty T^*T(E_Z)\, dE_Z$, is independent of $\Gamma_S$. This is analogous to the sum rule for oscillator strengths in the quantum theory of radiative transitions. Analytic expressions have been derived for the first-quasibound-state partial widths, $\Gamma_1^R$ and $\Gamma_1^L$, under the following conditions [13]: (1) the

potential energy is everywhere flat except for the step discontinuities at the heterojunctions, and (2) the dispersion relations for the particle are parabolic in all regions, including the barriers.

In many practical situations, such as double-barrier structures under large bias, the analytic expressions for $T^*T$ are inadequate and one must rely on numerical solutions. Under the condition of lateral momentum conservation, one solves the longitudinal effective-mass Schrödinger equation,

$$\mathbf{E}(P_Z/\hbar)F(z) + V(z)F(z) = EF(z), \tag{3}$$

where $P_Z$ is the longitudinal momentum operator, $\mathbf{E}(P_Z/\hbar)$ is the energy-dispersion functional, $V(z)$ is the electron potential energy including both compositional and electrostatic contributions, $F(z)$ is the envelope function, and $E$ is the energy eigenvalue. Near the conduction band edge of any semiconductor, the dispersion relation along a given direction of momentum space is parabolic, so that $\mathbf{E}(P_Z/\hbar) = P_Z^2/2m^*$ where $m^*$ is the local effective mass. In this case, Eq. (3) is a second-order linear differential equation that is solved uniquely by applying the boundary conditions of the continuity of $F$ and the continuity of the electron flux $(1/m^*)\,dF/dz$ at each heterojunction in the structure [14]. $T^*T$ through the structure is obtained by connecting the solutions across the heterojunctions using the transfer matrix technique [15].

If the particle energy is not near a band edge or is near the edge of degenerate bands, then the effective-mass equation does not apply straightforwardly. The common approach in this case is to employ the so-called envelope function approximation [16]. The tunneling wave function is represented as a combination of conduction- and valence-band envelope functions, and the dispersion relations are formulated within the context of multiple bands. For example, two-band models ($\Gamma$-point electron and light hole) have been successful in describing energy levels in type II band structures (defined in Section III.A) [16]. Two-band models have also been applied in tunneling problems [17]. A useful simplification of this formalism for electron tunneling results from assuming that the wave vectors and effective masses are everywhere determined by nonparabolic dispersion but that the wave function has only a conduction band component. The barrier dispersion is determined by connecting the conduction band to the light-hole band [18]. This results in an analytic expression of $E$ versus $K$ where $K$ is the attenuation coefficient, or the imaginary part of the complex wave vector. Associated with this expression is a branch point where $K$ reaches a maximum value in the bandgap. In the classically allowed regions, it often suffices to model the electron dispersion relation by the expression obtained from two-band $\mathbf{k} \cdot \mathbf{p}$ per-

turbation theory [19], $E(k) = (\hbar k)^2(1 - Ak^2)/2m^*$, where $A$ is a constant that depends on the material.

Some questions arise regarding the validity of the effective-mass equation, or envelope function approximation, in problems of heterobarrier tunneling. It is often asked, for example, how effectively a heterojunction couples the envelope function of an incident electron to components of the wavefunction in the barrier at different points in the Brillouin zone. One study of this issue has shown that when the barriers are sufficiently thin, the coupling is weak [20]. This situation applies to at least the lower end of the range of barrier thicknesses used in high-speed DBRTDs, which is roughly 1.0 to 3.0 nm. Thus, one can assume that the Brillouin zone character of the envelope function is preserved upon tunneling through thin bariers. Another question is whether it is valid to neglect the cell-periodic part of the wave function in the presence of the abrupt change of potential at a heterojunction. The answer is that the envelope function alone be adequate if it varies slowly over a unit cell [21]. This is generally true in semiconductor heterostructufes, where the electron energy usually lies within 1 eV or so of the closest band edge and thus the de Broglie wavelength (i.e., the inverse crystal wave vector) is much larger than a unit cell.

### C. Electrical Current and NDR

The electrical current through the first quasibound state of a double-barrier structure is understood from the diagram given in Fig. 1. As the bias voltage is increased from zero, the quasibound level in the quantum well drops relative to the band edge on the emitter or cathode side. When the quasibound level approaches alignment with the quasi-Fermi level $E_F^c$, the electron current begins to increase rapidly. This rise can be explained by the number of electrons in the cathode Fermi sphere that have $E_Z = E_1$ [22]. The current eventually approaches a peak near the voltage that aligns the quasibound level with the conduction band edge in the neutral region on the cathode side. This is the bias voltage depicted in Fig. 1. At higher voltages there are no electrons with $E_Z = E_1$, so the current decreases precipitously and an NDR region occurs. This NDR region is the basis for all of the high-speed oscillations and switching observed to date in DBRTDs.

The quality of a DBRTD is usually given by the peak current density $J_P$ and the peak-to-valley current ratio PVCR $\equiv J_P/J_V$, where $J_P$ and $J_V$ are the peak and valley current densities, respectively, associated with the NDR region. Other quantities of importance are the peak-to-valley volt-

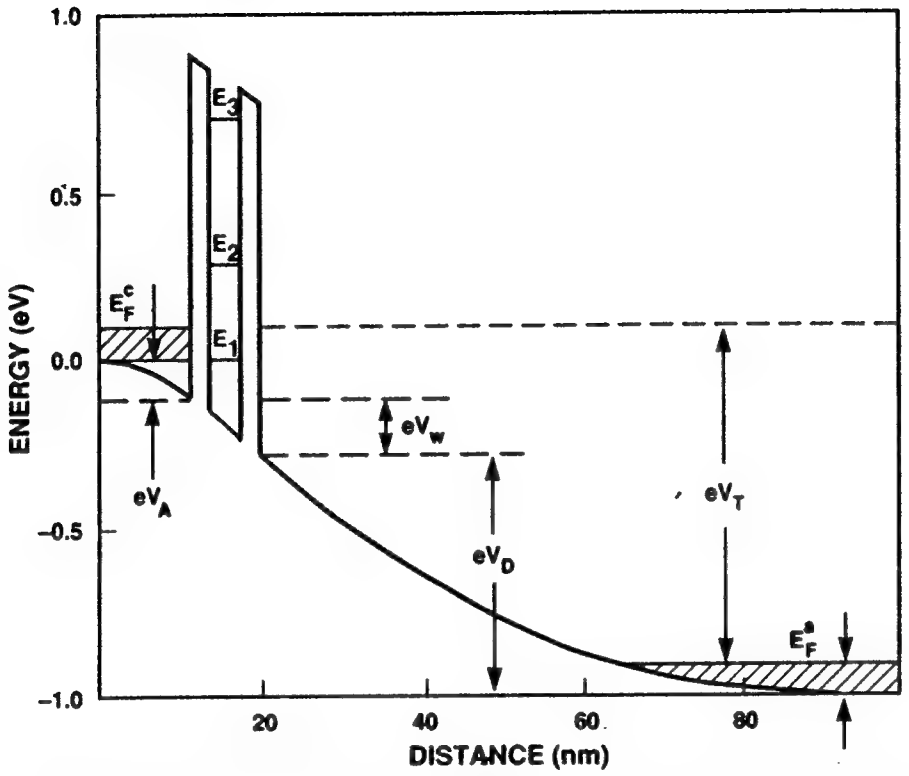


**Fig. 1.** Conduction-band bending diagram of a GaAs/AlAs DBRTD at a bias voltage corresponding to the peak of the resonant-tunneling current through the first quasibound state.

age ratio PVVR $\equiv V_V/V_P$, where $V_V$ and $V_P$ are the valley and peak voltages, respectively, and the available current $\Delta J \equiv J_P - J_V$. For high-speed operation the current density should be relatively large ($J_P \gtrsim 1 \times 10^4$ A cm$^{-2}$) for the same reason as in any other high-speed electronic device: high current density is required for fast charging and discharging of the device and circuit capacitance. The relationship between current density and device speed is addressed in Section VI.

## III. RESONANT-TUNNELING MATERIALS

### A. Material System Properties

It is a testament to the resonant-tunneling phenomenon that its trademark, the NDR region, has been observed at room temperature in several different material systems under a variety of crystalline conditions. In this section the constitutive properties of these material systems are summarized. One such property is the nature of the band alignment that occurs at a heterojunction between two materials of different bandgap. The well-

known type I alignment is one in which the bandgap of the narrower-gap material is contained entirely within the bandgap of the other on an energy diagram. In type II alignments, the bandgap of the narrower-gap material does not overlap the gap of the other material at all and usually lies well below it. In type II staggered stystems, the bandgap of the narrower-gap material overlaps the wider gap partially, usually in the bottom portion of the wider bandgap. Thus the wider-gap material appears as a barrier to electrons but a well to holes. Independent of band alignment, each of the systems is designated here by A/B, where A and B are the two constituent materials and B is the material with the wider bandgap.

A second constitutive property is the crystalline state of the semiconductor layers in and around the double-barrier structure. In the most desirable (lattice matched) case, all layers are made of materials having the same lattice constant as the substrate. One variation is to lattice match the quantum well and cladding layers but use a material having a different lattice constant in the barriers. If the barriers are sufficiently thin, their lattice will conform by compression or tension to the surrounding layers in the lateral plane, and will deform in an opposite sense along the longitudinal axis. This is called a pseudomorphic match. Another variation is to lattice match the barriers but use a material of a different lattice contant in all or part of the quantum well, or some portion of the cladding layers. Again, if the layers are sufficiently thin, a pseudomorphic match results. Finally, if the lattice constant of a layer is so different from the substrate, or if the difference is small but its thickness exceeds a critical (pseudomorphic) limit, this layer will relax to its intrinsic lattice constant and dislocations will form in abundance.

The diversity introduced by the different resonant-tunneling material systems is exemplified in Fig. 2, which shows the theoretical first-quasi-bound-state electron lifetime, $\tau_1 = \hbar/\Gamma_1$, as a function of barrier thickness for a fixed quantum well thickness of 4.6 nm. Nonparabolic effects are included. All of the materials represented in Fig. 2 have type I band offsets except InAs/AlSb, which is type II staggered. The important aspect of this plot is the broad range of lifetimes offered by different material systems at a given barrier thickness. This is a result of the strong dependence of the lifetime on the barrier attenuation coefficient, $\tau = \hbar/\Gamma_1 \propto \exp(KL_B)$, where $L_B$ is the barrier thickness. The difference in $K$ between the material systems arises from differences in the bandgap or band alignment. For example, the smaller lifetimes of the GaAs/$Al_{0.42}Ga_{0.58}As$ structure compared with the GaAs/AlAs structure are caused primarily by the smaller bandgap, and hence barrier height, of $Al_{0.42}Ga_{0.58}As$. In contrast, the much smaller lifetimes of the InAs/AlSb structure compared with the GaAs/AlAs structure are caused by the type II

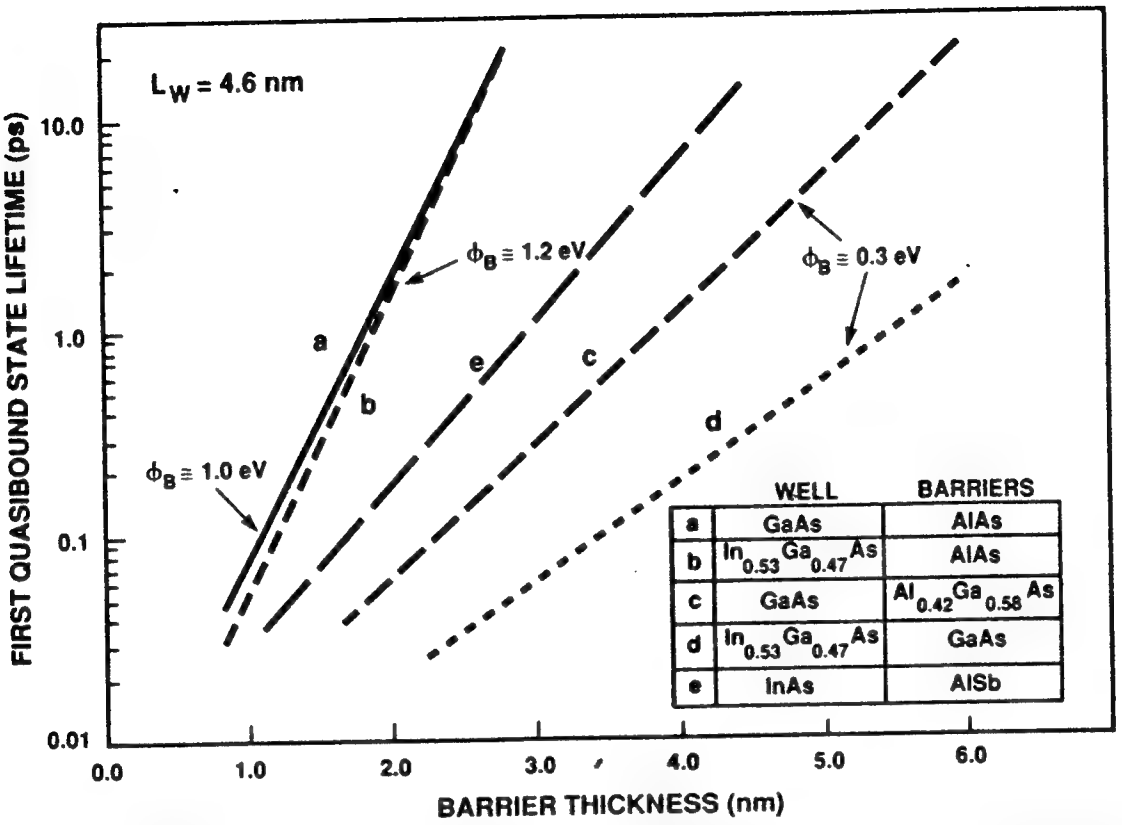


**Fig. 2.** Lifetime of the first quasibound state in double-barrier structures made from five of the material systems discussed in the text. In each structure the quantum well width is fixed at 4.6 nm.

staggered band alignment of InAs/AlSb, which is discussed in Section III.D.

## B. GaAs-Based Structures

The GaAs quantum well with $Al_xGa_{1-x}As$ barriers was the first material system to yield an NDR effect at low temperatures [6] and at room temperature [8]. With $x \approx 0.4$, this system provides useful PVCR at values of $J_P$ up to about $1 \times 10^4$ A cm$^{-2}$ [23]. At higher values of $J_P$ the PVCR is usually degraded by large thermionic current over the top of the barriers. Consequently, much better PVCR at high $J_P$ is obtained from GaAs/AlAs structures. In GaAs/AlAs DBRTDs having $J_P$ in the range from $10^4$ to $10^5$ A cm$^{-2}$, the best observed room-temperature PVCRs are about 4. Above this range, the PVCR degrades significantly. For example, PVCRs of 1.4 and 2.5 have been achieved in DBRTDs having $J_P$ of $1.5 \times 10^5$ A cm$^{-2}$ [24] and $1.3 \times 10^5$ A cm$^{-2}$ [25], respectively. The best reported PVCR with $J_P \gtrsim 10^5$ A cm$^{-2}$ is 3.0 at $J_P \approx 1.2 \times 10^5$ A cm$^{-2}$ [26]. This degradation is a drawback of GaAs/AlAs DBRTDs for high-speed applications, which

usually require $J_P \gtrsim 10^5$ A cm$^{-2}$. The $J$–$V$ curve of a high-$J_P$ GaAs/AlAs DBRTD is shown in Fig. 3 in comparison with the curves for DBRTDs made from alternative material systems.

Several clever structures have been implemented to improve the PVCR of lattice-matched GaAs DBRTDs, at least at low current densities. For example, anode- and cathode-side AlAs barriers have been grown with $Al_xGa_{1-x}As$ layers just outside to form "chair barriers" [27]. This has resulted in a DBRTD having a PVCR of 6.3 at room temperature [28]. Another structure contained an $In_xGa_{1-x}As$ layer either as a prewell on the cathode side [29] or in place of the GaAs quantum well [30]. An improved PVCR resulted in both cases.

### C. $In_{0.53}Ga_{0.47}As$-Based Structures

The first useful DBRTDs fabricated in a system other than GaAs/$Al_xGa_{1-x}As$ were made from the $In_{0.53}Ga_{0.47}As/In_{0.52}Al_{0.48}As$ system [31]. Both of these ternary alloys are lattice matched to InP substrates. The initial $In_{0.53}Ga_{0.47}As/In_{0.52}Al_{0.48}As$ DBRTDs yielded a PVCR of 2.3 at room temperature. This was subsequently improved to about 7 at room temperature and 40 at 77 K [32,33]. Shortly thereafter, superior results were

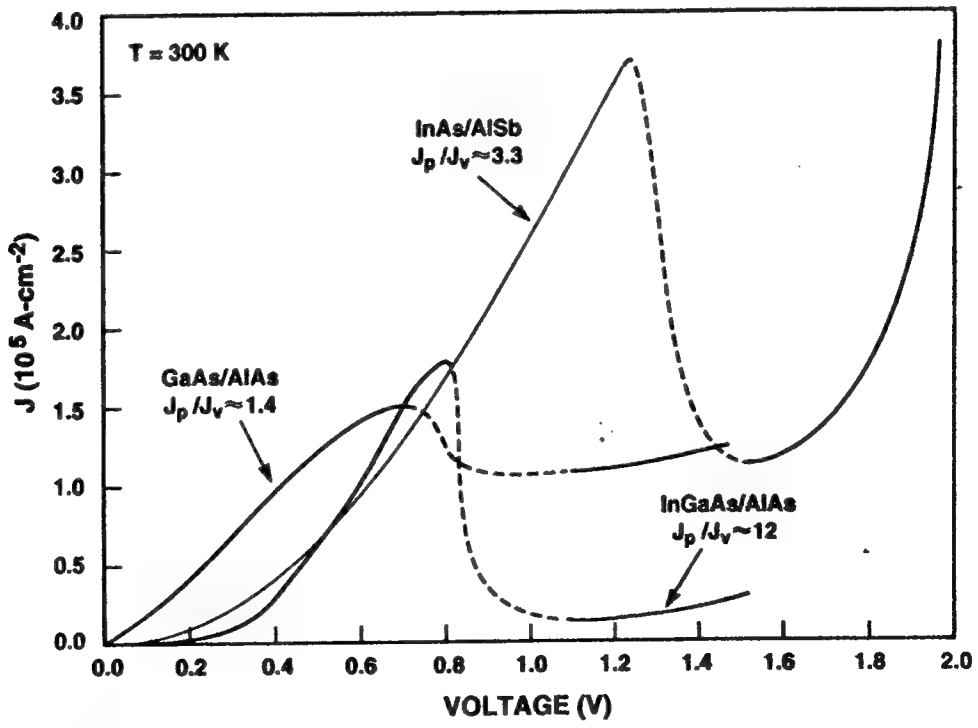


**Fig. 3.** Room-temperature current density vs. voltage curves for high-speed DBRTDs made from three different material systems.

obtained by replacing the $In_{0.52}Al_{0.48}As$ barriers with AlAs, which in the relaxed state has a 3.5% smaller lattice constant than $In_{0.53}Ga_{0.47}As$. In spite of this difference, the AlAs is pseudomorphic if the barrier thickness is limited to approximately 3.0 nm or less. The resulting DBRTDs yielded an unprecedented PVCR of 14 at room temperature [34]. Further improvement followed with the achievement of a PVCR of 30 at room temperature in a DBRTD having a thin InAs layer embedded in the $In_{0.53}Ga_{0.47}As$ quantum well [35].

A second $In_{0.53}Ga_{0.47}As$-based system of interest contains GaAs rather than AlAs barriers. Because of its low electronic and light-hole effective masses, the GaAs barrier has a maximum attenuation coefficient in the gap that is about a factor of 2 smaller. However, the bandgap difference between the constituent materials is small, so a low barrier height (~0.3 eV) is obtained. Consequently, the NDR region is observed only at about 77 K or lower operating temperatures [36].

A third $In_{0.53}Ga_{0.47}As$-based DBRTD has been fabricated with InP barriers by low-pressure metalorganic chemical vapor deposition [37]. The structure contained a 10-nm-thick $In_{0.53}Ga_{0.47}As$ quantum well and 10-nm-thick InP barriers. It displayed a 77-K PVCR of 1.2 for resonant tunneling through the first quasibound level and a PVCR of 3.0 through the second level. Although these results are inferior to those discussed above, the thick barriers of the $In_{0.53}Ga_{0.47}As$/InP sample probably hindered the performance greatly, just as they do in other material systems. This DBRTD with much thinner InP barriers could ultimately provide competitive performance with the other $In_{0.53}Ga_{0.47}As$-based devices, since it has the advantage over $In_{0.53}Ga_{0.47}As$/AlAs of lattice matching and the advantage over $In_{0.53}Ga_{0.47}As/In_{0.52}Al_{0.48}As$ of no alloy scattering in the barriers.

### D. InAs-Based Structures

High-quality DBRTDs have been fabricated from the InAs/AlSb material system, whose band offset is shown in Fig. 4. This is a type II staggered offset in which the valence band edge of the AlSb lines up in the bandgap of the InAs. Consequently, an electron tunnels into the AlSb from the InAs at an energy well below the branch point, and $K$ is approximately 0.6 times the maximum value. In contrast, an electron tunnels into a type I offset barrier, such as the AlAs barrier depicted in Fig. 4, much closer to the branch point. Since $\Gamma_1$ and $J_P$ both depend on this attenuation coefficient roughly as $\exp(-KL_B)$, the difference in $K$ corresponds to a difference of approximately two times in $J_P$ at the typical barrier thickness

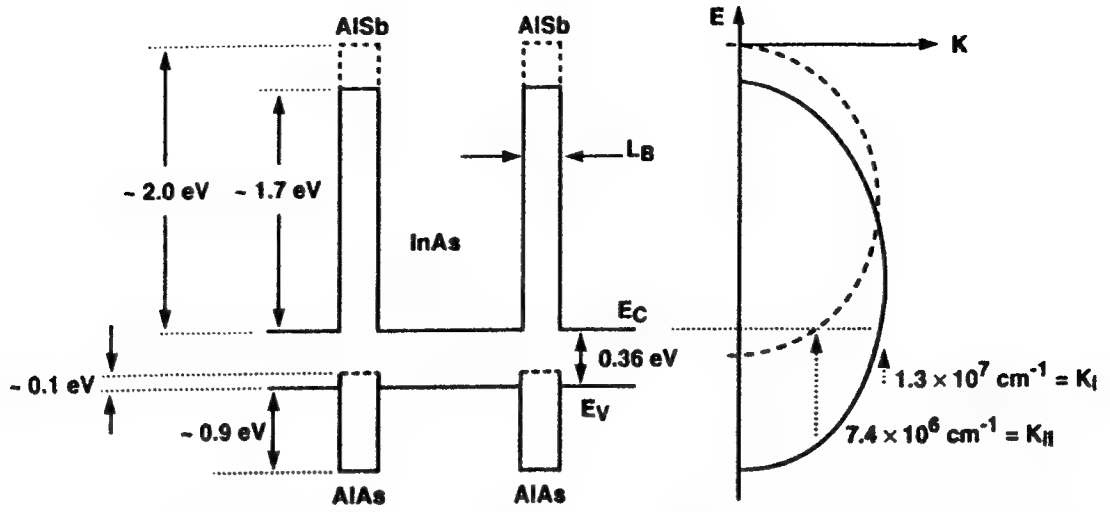


**Fig. 4.** Band alignment of the type II staggered InAs/AlSb material system in contrast to that of the type I InAs/AlAs system. It is assumed for simplicity that the latter system is lattice matched and that 65% of the difference between the AlAs and InAs Γ-point bandgap appears as a barrier in the conduction band. AlSb is shown as a dashed line in the barrier regions and AlAs as a solid line. $K_I$ and $K_{II}$ are the approximate attenuation coefficients of an InAs electron (at the conduction band edge) in the AlAs and AlSb barriers, respectively.

of 1.5 nm. The superior current capability of the InAs/AlSb structure is displayed in Fig. 3. The $J$–$V$ curve was obtained on a diode having 1.5-nm-thick AlSb barriers and a 6.4-nm-thick InAs quantum well [38]. The measured values of $J_P = 3.7 \times 10^5$ A cm$^{-2}$ and $\Delta J = 2 \times 10^5$ A cm$^{-2}$ are comparable to the best results achieved in the $In_{0.53}Ga_{0.47}As$/AlAs system and are considerably better than those of GaAs/AlAs DBRTDs.

In addition to the superior current density, the InAs-based material systems have two advantages over GaAs-based systems for high-speed device performance [38]. First, electrons will drift across a given depletion layer in InAs much more rapidly than in GaAs provided that this layer is sufficiently thin ($\lesssim 0.1$ $\mu$m) or the voltage drop is sufficiently small that there is little probability of impact ionization [39]. The higher drift velocities compared with GaAs are due to the weaker electron LO-phonon interaction strength in InAs and the much larger separation in energy between the conduction band edge and the first upper valley. A short depletion layer transit time is necessary to maximize the device speed, as discussed in Section V. A second advantage is that InAs DBRTDs have a significantly lower series resistance $R_S$. This stems primarily from the ultralow specific resistance $R_C$ of ohmic contacts to InAs. Values of $R_C$ as low as $5 \times 10^{-8}$ Ω cm$^2$ have been measured by transmission line model measurements made on nonalloyed InAs ohmic contacts [40]. The $R_S$ is further reduced by the higher mobility of electrons in InAs compared to GaAs at all practical $n$-type doping concentrations.

Each of these advantages also applies to a lesser extent in comparing $In_{0.53}Ga_{0.47}As$ to GaAs.

### E. GaSb and InSb Structures

A type II DBRTD is obtained by replacing the InAs quantum well in the preceding structure by GaSb. This is the basis for a type of resonant tunneling through quasibound levels in the valence band, which is called resonant interband tunneling (RIT) [41]. The RIT structure has demonstrated a very high PVCR of approximately 20 at room temperature. A complementary structure having an InAs quantum well and GaSb cladding layers has also been demonstrated [42,43]. Unfortunately, in both types of structures the peak current density is not yet sufficient to be useful in high-speed circuits. However, the type II alignment between GaSb and InAs allows for new types of vertical transistor structures [44,45].

A DBRTD has also been fabricated in the InSb/InAlSb system [46]. The PVCRs measured at room temperature and 77 K were 1.4 and 3.9, respectively. The appeal of this material system is that InSb has the excellent transport properties of very low electronic effective mass ($m^* = 0.0139m_0$) and high mobility resulting from low electron–phonon scattering cross sections. A disadvantage is the narrow bandgap ($E_G = 0.17$ eV at $T = 300$ K), which magnifies the effects of impact ionization and Zener (i.e., cross-gap) tunneling.

### F. Column IV Material Systems

In the preceding sections, the material systems have consisted of some combination of column III (Ga, Al, or In) and column V (As, Sb, or P) materials. Most high-speed DBRTDs have been made from one of these combinations. However, because of the success and pervasiveness of silicon in electronic devices, efforts have been expended to develop Si-based resonant-tunneling structures. Two interesting material systems are $Si_xGe_{1-x}$/Si and Si/SiC. Although the band alignment in $Si_xGe_{1-x}$/Si is type I, most of the bandgap difference appears in the valence band of the SiGe. This results in a Si barrier in SiGe that is too low for strong electronic resonant tunneling. Therefore, researchers have studied hole resonant tunneling [47,48]. The best result reported to date is a PVCR of 2.0 at 77 K [49]. NDR has not yet been observed at room temperature. The relatively poor performance of $Si_xGe_{1-x}$/Si DBRTDs is apparently not caused by lattice mismatch, but instead is the consequence of the undesirable trans-

mission characteristics associated with resonant tunneling through quasi-bound levels in the valence band. The mixing that occurs between the light- and heavy-hole subbands smears out the transmission probability such that the ground-state peak is not well isolated from the next higher peak, and hence the PVCR is degraded.

The Si/SiC system alleviates the difficulties of SiGe/Si by offering a much larger conduction band offset and thus the possibility of strong electronic resonant tunneling [50]. Unfortunately, the poor crystalline quality of epitaxial SiC has precluded good experimental results. However, if SiC epitaxial growth techniques were to advance significantly, Si/SiC could become an important material system, particularly for applications of DBRTDs in large-scale Si integrated circuits.

## IV. DBRTD DEVICE PHYSICS

### A. Band Bending and Diode Capacitance

An external bias voltage applied across a DBRTD modifies the equilibrium band profile in the active region. In order to analyze the current density, one must determine the modified band profile, or band bending, to a satisfactory degree of accuracy. A first estimate is obtained by modeling the device as a semiconductor–insulator–semiconductor (SIS) diode. Unless the current density is very high, one can then assume that the diode is in a condition of quasiequilibrium. Under this condition, the electron concentration on each side is characterized by a uniform quasi-Fermi level [i.e., $E_F^c$ on the cathode (or emitter) side and $E_F^a$ on the anode (or collector) side], as shown in Fig. 1. The band bending is obtained by solving Poisson's equation on each side and connecting the solutions with a uniform field across the double-barrier structure. Shown in Fig. 5 is the band bending obtained by this method for a DBRTD containing 5.0-nm-thick $Al_{0.42}Ga_{0.58}As$ barriers, a 5.0-nm-thick GaAs quantum well, and 50-nm-thick lightly doped spacer layers on either side.

The capacitance of the DBRTD in this model is what one expects from an analogous SIS diode. That is, $C \approx \varepsilon A(L_D + L_W + 2L_B + L_A)^{-1}$, where $A$ is the area, $L_D$ is the length of the depletion region, and $L_A$ is the length of the accumulation region (i.e., the distance over which band bending occurs) on the cathode side. For the device in Fig. 5, $L_D \approx 60$ nm, $L_W + 2L_B = 15$ nm, and $L_A \approx 25$ nm, leading to $C/A \approx 1.1$ fF $\mu m^{-2}$. This is a typical specific capacitance for high-speed DBRTDs and is considerably lower than that of most other tunneling devices such as $p$–$n$ (Esaki) di-

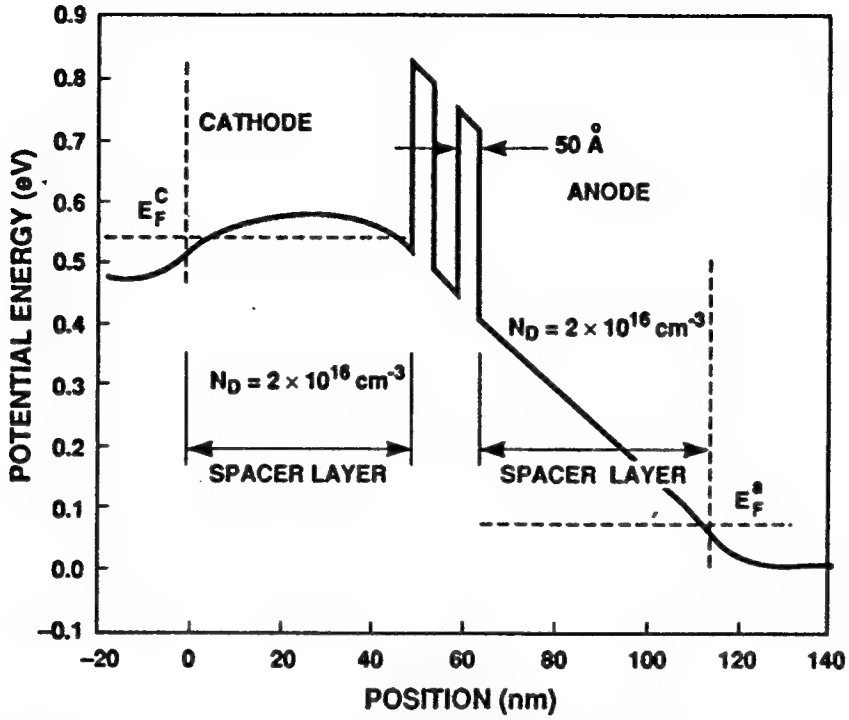


**Fig. 5.** Solution to Poisson's equation in a GaAs/$Al_{0.42}Ga_{0.58}As$ DBRTD at room temperature assuming that no charge is stored in the quantum well and that there is no spatial quantization outside the double-barrier structure.

odes or Josephson junction devices. The latter two devices require degeneration electron concentrations on both sides of the junction in order to achieve high current densities. In that case both $L_D$ and $L_A$ are 10 nm or less, and the specific capacitance is at least five times that of the DBRTD.

A more accurate estimate of the band bending maintains the assumption of quasiequilibrium in the cladding layers but accounts for at least one of the following effects: (1) spatial quantization in the accumulation layer or (2) charge storage in the quantum well. To deal properly with the first effect, one must carry out self-consistent calculations of the Poisson and Schrödinger equations. Such calculations made on DBRTDs indicate that the electron states in the accumulation layer consist of a continuum at energies above the neutral band edge on the cathode side and quasibound states at lower energies [51]. In many DBRTD structures, the binding energy of the lowest quasibound state (relative to the neutral band edge) is only a small fraction of the total potential drop across the accumulation layer, $V_A$. The presence of these quasibound levels has been correlated experimentally to undulations in the $I$–$V$ curve at voltages below the first peak [52]. The charge storage in the quantum well can have a profound effect on the $I$–$V$ curve and is addressed in Section IV.C.

### B. Current Density

The current density $J$ is estimated quantitatively by employing the well-known stationary-state transport model in which the traversal through the double-barrier structure is analyzed by the stationary-state formulation discussed in Section II.B and the transport in the cladding layers is analyzed with semiclassical theory [53]. The magnitude of $J$ is the difference between the cathode-to-anode and anode-to-cathode electron fluxes in each $E_Z$ interval multiplied by the transmission probability in that interval, all integrated over $E_Z$ [15]:

$$J = \beta \mathrm{kT} \int_0^\infty dE_Z \, T^*T \log\left[\frac{1 + \exp(E_F^c + eV_A - E_Z)/kT}{1 + \exp(E_F^c + eV_A - eV_T - E_Z)/kT}\right], \quad (4)$$

where $\beta = em^*/2\pi^2\hbar^3$, and $V_T$ is the total applied voltage across the device defined in Fig. 1. It is useful to evaluate this integral in conjunction with the Breit–Wigner form for $T^*T$ in Section II.A. When the temperature is low enough that the Fermi distribution on the cathode side is degenerate and the bias voltage is high enough that the anode-to-cathode current can be neglected, one obtains

$$J \approx \frac{2\beta\Gamma_1^L\Gamma_1^R}{\Gamma_1}(E_F^c + eV_A - E_P)\left[\tan^{-1}\left(\frac{2(E_F^c + eV_A - E_P)}{\Gamma_T}\right) - \tan^{-1}\left(\frac{2(eV_A - E_P)}{\Gamma_T}\right)\right] + \frac{\beta\Gamma_1^L\Gamma_1^R\Gamma_T}{2\Gamma_1}\log\left[\frac{\Gamma_T^2/4 + (eV_A - E_P)^2}{\Gamma_T^2/4 + (eV_A + E_F^c - E_P)^2}\right], \quad (5)$$

where $E_P$ is the peak energy of $T^*T$ relative to the conduction band edge on the cathode side. The lower limit of integration has been taken as $V_A$ based on the assumption that a negligible fraction of the electrons occupy spatially quantized states in the accumulation layer. In DBRTDs containing thin barriers, the major effect of the bias voltage on $T^*T$ is simply to displace $E_P$ downward. At low bias voltages consistent with $E_F^c + eV_A < E_P$, both $\tan^{-1}$ factors are approximately $-\pi/2$, and the current is determined largely by the second term in Eq. (5) (with the logarithmic factor). At bias voltages consistent with $eV_A < E_P < eV_A + E_F^c$, the two $\tan^{-1}$ factors sum to approximately $\pi$ and the second term (with logarithmic factor) is negligible provided that $E_F^c > \Gamma_T$. From the prefactor for the first term, the current increases monotonically with bias voltage in this range up to the point $eV_A \approx E_P$ where the second $\tan^{-1}$ factor changes sign to positive. For just a small variation in bias voltage about this point, the sum of the two $\tan^{-1}$ terms goes from $\pi$ to 0. This rapid change defines the precipitous drop in current associated with the NDR region. For a bias

voltage slightly less than that yielding $eV_A = E_P$, the current density reaches its peak value. Under the condition $E_F^c \gg \Gamma_T$, one finds $J_P \approx 2\pi\beta\Gamma_1^L\Gamma_1^R E_F^c/\Gamma_1$. The fact that $\Gamma_S$ does not appear in this expression illustrates the important point that $J_P$ is independent of scattering processes in the double-barrier structure that can be represented by the Breit–Wigner formalism and are weak enough to satisfy $E_F^c \gg \Gamma_S$. This conclusion was first drawn by Weil and Vinter [54] in their analysis of sequential resonant tunneling.

Figure 6 compares the theoretical and experimental current density for one of the best DBRTDs (in terms of room-temperature PVCR) fabricated in the GaAs/AlGaAs material system. It is the same diode whose band bending appears in Fig. 5. The peak currents agree within a factor of 2, but the valley currents differ by about a factor of 100. The discrepancy in valley currents reflects the predominance of excess-current mechanisms not addressed by the Breit–Wigner model. Several of these mechanisms are discussed in Section IV.E. Another experimental aspect not explained by the model is the small undulation in the experimental $I$–$V$ curve at approximately 0.3 V. This is an indicator of quantum size effects in the accumulation layer on the cathode side. The distorted form of the experi-

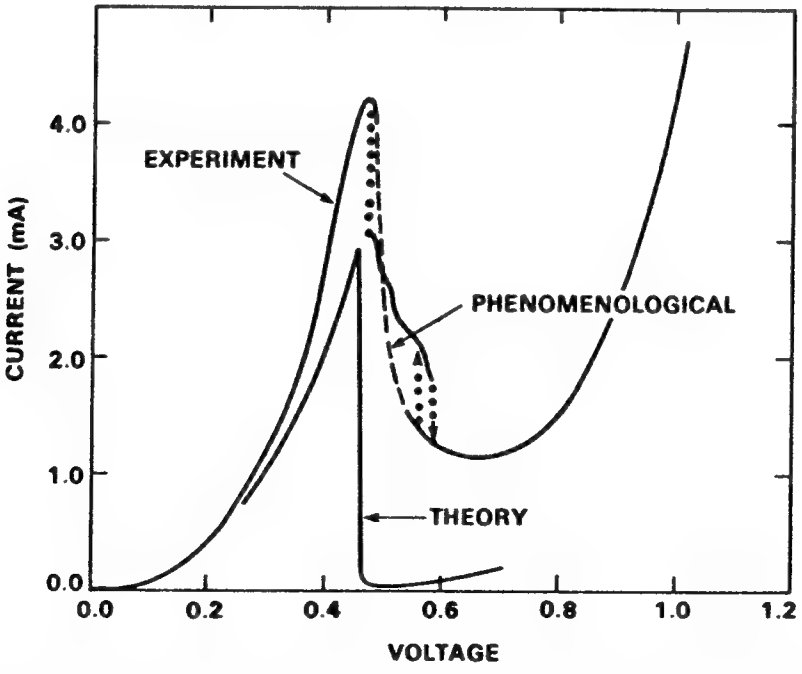


**Fig. 6.** Comparison of the room-temperature experimental and theoretical $I$–$V$ curves for the DBRTD in Fig. 5. The dotted lines in the NDR region represent discontinuous jumps in the current caused by switching into or out of the oscillation region shown by the solid line in the middle of the NDR region. The dashed line is a phenomenological fit that represents the expected form of the $I$–$V$ curve in the absence of oscillations. The theoretical curve is based on the stationary-state model of Section IV.B.

mental $I$–$V$ curve in the NDR region is attributed to the rectification by the DBRTD of its own electrical oscillations in the measurement circuit. The rectification can result in a hysteresis loop in the $I$–$V$ curve (denoted by arrows in Fig. 6), which is known as *extrinsic bistability* [55].

Although there are several shortcomings with the stationary-state model, the fact remains that in high-quality structures it does a good job of predicting $J_P$. Thus, it is useful in designing DBRTDs for high-speed applications, where $J_P$ is one of the most important device characteristics.

### C. Quantum Well Charge Storage

Like any quantum well system, the double-barrier structure can harbor mobile sheet charge. Intuitively, one expects that the sheet charge density $\sigma_w$ is proportional to the product of the current density and the quasibound lifetime (i.e., $\sigma_w = J\tau$). Detailed treatments of this effect in the sequential [56] and coherent [57] limits have resulted in the following expression for $\sigma_w$ in the first quasibound level:

$$\sigma_{w,1} = \frac{J\hbar}{\Gamma_1^R}. \tag{6}$$

An important effect of the sheet charge is to alter the electrostatic potential across the double-barrier structure from the linear form assumed in Sections IV.A and IV.B. The altered potential affects the resonant-tunneling current because of the strong dependence of this current on the level of the quasibound state in the well. Because the sheet charge is proportional to the current density by Eq. (6), the net current density becomes self-dependent. This mechanism is known as *electrostatic feedback* [58,59]. Shown in Fig. 7a are $I$–$V$ curves for a typical double-barrier structure computed by demanding self-consistency between Eqs. (5) and (6). With $\Gamma_S$ set equal to zero, the current is multiple valued between the peak and valley voltages, an effect known as *intrinsic bistability* [58]. This effect has not been observed unambiguously in any double-barrier structure containing symmetric barriers (i.e., the same barrier materials and thicknesses). Instead, such structures typically display *extrinsic* bistability as defined in Section IV.B. Intrinsic bistability has been observed clearly only in a highly asymmetric structure biased so that the more transparent barrier is adjacent to the cathode (i.e., $\Gamma_1^L \gg \Gamma_1^R$) [59,60].

One possible reason for the rarity of experimental intrinsic bistability is the broadening of $T^*T$ by scattering. This effect can be modeled by making $\Gamma_S$ nonzero in the self-consistent $I$–$V$ calculations. For example, when $\Gamma_S = 4.0$ meV, the bistability in Fig. 7a disappears. At a much larger $\Gamma_S$ of

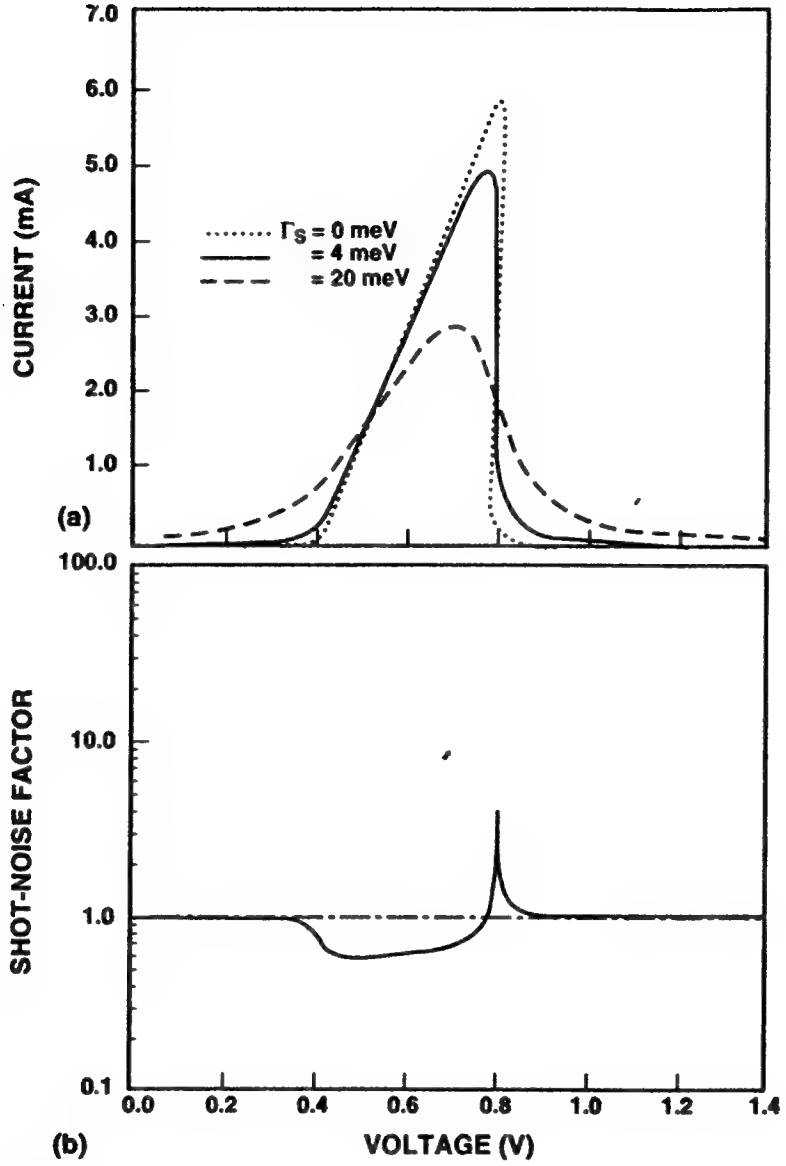


**Fig. 7.** (a) Theoretical $I$–$V$ curves for a GaAs/$Al_{0.42}Ga_{0.58}As$ DBRTD at 77 K based on the stationary-state model with three different scattering parameters: $\Gamma_S$ = 0.0, 4.0, and 20.0 meV. (b) Theoretical shot-noise factor for same device as in (a) with $\Gamma_S$ = 4 meV.

20 meV, which is approaching $E_F^c$ in the device of Fig. 7a, the peak current decreases and the peak region broadens. A $\Gamma_S$ of 4 meV is consistent with the results of a recent experimental study on a variety of double-barrier structures [61]. Another reason for the lack of bistability may be quantum size effects in the accumulation layer. Self-consistent calculations of the $I$–$V$ curve in symmetric DBRTDs generally do not display intrinsic bistability if spatial quantization is accounted for in both the quantum well and accumulation layer [62,63].

### D. Current Fluctuations

As in all electronic devices, the fluctuations of current in DBRTDs arise from fluctuations in the population of electronic states or, equivalently, fluctuations in the energy and momentum of electrons in specific regions of the device. These fluctuations give rise to electrical noise at the terminals of the device and are important in DBRTDs for the following reasons. First, in a practical sense the electrical noise sets the limit on the performance of the DBRTD in certain device applications such as oscillators. Second, the measured noise can reflect underlying physical processes that are difficult to detect by other experimental techniques.

The current fluctuations in a DBRTD are quantified in the standard way by a power spectrum $S_I(f)$, which represents the mean-square current measured at frequency $f$ per hertz of bandwidth by an ideal current meter connected across the terminals of the device. At low frequencies, the power spectrum has a $1/f$-type behavior arising from a number of mechanisms, such as trap states in the barriers. Well above the $1/f$ knee and up to frequencies approaching the speed limits of the device, the current fluctuations are dominated by thermal and shot noise mechanisms. The thermal noise is dominant when little or no bias voltage is applied, so that the device is near thermal equilibrium. The shot noise dominates at high bias voltages, where the current is large and is limited by the double-barrier structure. The shot noise power spectrum measured between the anode and cathode contacts is expressed by $S_I = 2\gamma eI$, where $\gamma$ is the shot noise factor [64]. For devices containing single barriers whose transmission properties do not depend on the current density (e.g., $p$–$n$, Schottky, and single-heterobarrier diodes), it is generally found that $\gamma = 1.0$. The DBRTD can display deviations from $\gamma = 1.0$ because $T^*T$ is a function of the current through the electrostatic feedback mechanism.

To model the shot noise mechanism in DBRTDs, one supposes that the total current arises from a superposition of electron fluxes incident on the double-barrier structure in all longitudinal energy intervals. Fluctuations occur in each flux because of thermalization processes on the cathode side. These fluctuations have two effects on the total current. First, they contribute directly to a fluctuation in the transmitted flux on the anode side. Second, they vary the charge in the quantum well, which alters the energy level of the quasibound state electrostatically. This process modulates the transmission in other energy intervals, thereby decreasing or increasing the current in those intervals. A detailed calculation of the shot noise factor based on these considerations has been carried out in the limit of degenerate Fermi statistics on the cathode side [65]. The theoreti-

cal results are shown in Fig. 7b for the same DBRTD as in Figs. 5 and 6. At bias voltages below the current peak, the shot noise is suppressed, the minimum $\gamma$ being approximately 0.5. At the peak voltage, $\gamma$ crosses unity and stays greater than 1.0 throughout the NDR region, representing shot noise enhancement. Both of these predictions are in good agreement with the experimental results described in Section VII.D.

### E. Excess Current

Excess current is defined here as the current measured through the RTD, near the valley point and beyond, that is not explained by Eq. (4). It does not include the potentially large current components that traverse the double-barrier structure through upper quasibound levels or thermionically over the top of the barriers. The latter two components are properly predicted by Eq. (4) provided that an accurate form of the transmission probability is obtained at all longitudinal energies.

One of the most important sources of excess current in RTDs is transport associated with upper valleys, particularly the $X$-valley in AlAs barriers. Early on, the superiority of the $In_{0.53}Ga_{0.47}As$/AlAs diodes over GaAs/AlAs diodes was attributed in large part to the greater energy separation, ~0.65 eV, between the $\Gamma$ conduction band minimum in the $In_{0.53}Ga_{0.47}As$ and the $X$ conduction-band minimum in the AlAs barrier [34]. In contrast, this separation is estimated to be 0.13 eV in the GaAs/AlAs system and has been experimentally correlated with the excess valley current in these devices through hydrostatic pressure experiments [66].

The $X$-valley-related excess current in both single- and double-barrier structures has been studied theoretically by a number of techniques including a Fowler–Nordheim model [67], the transfer matrix technique [68], a pseudopotential method [69], and an empirical tight-binding formalism [70]. Although there is not a consensus, a commonly described transport mechanism in double-barrier structures is one whereby the incident $\Gamma$ electron transfers to $X$ at the first heterojunction, maintains an $X$ character throughout the double-barrier structure, and subsequently transfers from $X$ back to $\Gamma$ at the last heterojunction. Material systems having a large $\Gamma$–$X$ offset greatly suppress this mechanism by making the initial $\Gamma$–$X$ transfer much less probable.

Another important source of excess current, inherent to all RTD materials, is LO-phonon scattering. In the sequential picture, this scattering allows electrons to transfer from the cathode side into the quantum well at bias voltages past the point of alignment between the quasibound level

and occupied states on the cathode side [71]. Once in the quantum well, the electrons can tunnel to the anode side by elastic means. In the coherent picture, the LO-phonon scattering introduces sidebands on the transmission probability curve separated by an integral number of phonon quanta, $\pm n\hbar\omega_{LO}$, from the central peak [72]. In either picture, a large excess current arises in the vicinity of the valley voltage in most RTDs. Materials having lower effective mass tend to have less of this scattering, which is another advantage of the indium-bearing materials, $In_{0.53}Ga_{0.47}As$ and especially InAs, over GaAs.

Acoustic phonon scattering and alloy scattering have been analyzed by the same sequential mechanism as used for the LO phonons [71]. The conclusion reached for acoustic phonons is that they play a much smaller role than optical phonons in generating excess current. However, the analysis was not carried out for polar-mode (i.e., piezoelectric) acoustic phonon scattering, which is known to be very strong in narrow-band-gap, low-effective-mass materials. Alloy scattering in ternary compound barriers can also give rise to a significant excess current component that is nearly independent of temperature. This component can explain the inferior PVCR of the $In_{0.53}Ga_{0.47}As/In_{0.52}Al_{0.48}As$ RTDs relative to those made from $In_{0.53}Ga_{0.47}As/AlAs$, since the AlAs barriers are presumably pseudomorphic and, therefore, introduce neither alloy nor dislocation scattering.

More recently, the excess cufrent due to scattering off of interface defects has been studied [73]. This is an important mechanism because it is generally believed that the heterobarriers in all heterojunction devices, including RTDs, fluctuate in thickness in the lateral plane by at least one monolayer. This imperfection breaks down the conservation of lateral momentum during tunneling, leading to a scattering mechanism that, like alloy scattering, has a very broad transmission characteristic. An interesting prediction is that the strength of this scattering mechanism depends heavily on which interfaces of the RTD barriers are assumed to be rough [73].

A final excess current mechanism inherent to all RTDs arises from scattering in the cladding layers. This is, perhaps, the most fundamental of all scattering mechanisms, but one of the most difficult to deal with, since it transcends the stationary-state model outlined in Section IV.B. The stationary-state model separates the quantum mechanical transport in the barrier structure from the semiclassical transport in the cladding layers. A proper description of this mechanism requires the quantum transport theory discussed in Chapter 9. The latter theory has yielded excellent agreement with experiment at the valley point of GaAs/AlAs RTDs [63].

## V. TIME-DELAY MECHANISMS

### A. Fundamental *RC* Limit

Like any electronic device in which the current flow is limited by a barrier, a fundamental speed limit of the DBRTD is set by the time required to charge or discharge the space charge layers in the active region of the device. This is known as the *RC* limit, where $R$ is some combination of the DBRTD differential resistance and the external load resistance and $C$ is the capacitance associated with the active region of the device. A great advantage of the DBRTD over most other tunneling devices is that the intrinsic *RC* time constant can be made very small in most applications, with values below 1 ps being possible in optimized devices. This is because $R$ and $C$ are determined by different factors, so they are essentially independent quantities. The component of $R$ associated with the device differential resistance is inversely related to $J_p$, which depends on the carrier concentration on the cathode side (through the quasi-Fermi level $E_F^c$) and on the area (in energy space) under the transmission resonance (see Section IV.B). $C$ is inversely related to the depletion length on the anode side, which depends on the doping distribution on that side. Two mechanisms that reduce the speed of the DBRTD below that associated with the *RC* time are the finite resonant-tunneling traversal time and the finite transit time across the depletion layer.

### B. Resonant-Tunneling Traversal Time

The effect of the resonant-tunneling traversal time can be analyzed by a number of techniques with widely varying degrees of sophistication. One analysis has applied linear-response theory to determine the equivalent electrical admittance of the double-barrier structure [74]. The analysis starts by calculating the response of the conduction current through the $n$th quasibound level, $i(t)$, to an applied voltage step $\Delta V$. It is reasonable to assume that the step response is exponential in time with time constant $\tau_n$ [74],

$$i(t) = I_1\theta(-t) + [I_2 + (I_1 - I_2)\exp(-t/\tau_n)]\theta(t), \tag{7}$$

where $I_1$ and $I_2$ are the initial and final dc currents, respectively, and $\theta(t)$ is the unit step function. In the small-signal limit where $I_2 = I_1 + G_S\,\Delta V$ and $G_S$ is the differential conductance of the double-barrier structure, the impulse response function is given by $h(t) = (\Delta V)^{-1}\, di(t)/dt = [1 - \exp(-t/\tau_n)]\delta(t)G_S + \exp(-t/\tau_n)\theta(t)G_S/\tau_n$. Finally, the admittance is ob-

tained by Fourier transformation,

$$Y_S(\omega) = \int_{-\infty}^{\infty} h(t) \exp(-i\omega t)\, dt = \frac{G_S}{1 + i\omega\tau_n}. \tag{8}$$

The reciprocal impedance function, $Z_S(\omega) = Y_S^{-1}(\omega)$, has the form $G_S^{-1} + i\omega L_S$, where $L_S = \tau_n/G_S$ is the "quantum well inductance." Intuitively, an inductive reactance might be expected in any model of resonant tunneling because the time required for the buildup or decay of the wave function in the quantum well leads to a delay of current with respect to voltage.

An inductive character of the resonant-tunneling admittance has also been predicted by more rigorous quantum transport treatments [63,75]. In at least two such treatments the magnitude of the inductance was comparable to that derived here, but the sign was opposite, that is, $L_S = -\tau_n/G_S$. The sign is important because the high-frequency admittance behaves very differently when the inductance is negative than when it is positive. The result derived here would change sign if the argument of the exponential in Eq. (8) was positive. However, $\exp(-i\omega t)$ is the correct form, because the Fourier transform is a special case of the Laplace transform, and to obtain a bounded result the Laplace transform must weight the time-varying waveform by $\exp(-st)$, where $s$ is the complex frequency.

One shortcoming of the analysis is the assumption of an exponential approach to steady state. It is thought that the actual conduction current displays a much richer behavior on short time scales. Time-dependent quantum mechanical solutions yield an oscillatory component with an exponentially decaying envelope [75]. This is similar to the well-known *ringing* phenomenon of classical resonant systems. For resonant tunneling through the first quasibound level, the oscillatory component has a period close to the traversal time $t_w$ across the quantum well of a wave packet centered at energy $E_1$. The effect of the ringing on the admittance is to cause the imaginary part to increase as $\omega$ approaches $t_w^{-1}$. This increase will be most observable experimentally in structures designed with very thin barriers so that $\tau_1 \lesssim t_w$.

### C. Depletion-Layer Transit Time

The effect of a finite depletion layer transit time can be understood by thinking of the double-barrier structure as an electron injector. As such, the electrons will have an initial kinetic energy that is close to an $E_n$ in the quantum well. Most double-barrier structures have $E_1 \gtrsim 100$ meV to satisfy the spatial quantization condition given in Section II.A. Such a kinetic energy corresponds to a very high group velocity $v_g$ in the common

III–V materials. For example, a 0.1-eV kinetic energy in GaAs corresponds to $v_g \approx 7 \times 10^7$ cm$^{-1}$ according to the theoretical Γ-valley dispersion curve [76]. One expects this velocity to be maintained over some distance roughly equal to the ballistic mean free path, which depends strongly on the applied electric field, the upper-valley separation, and the strength of the optical phonon interaction. After drifting this distance, the electron rapidly decelerates and then crosses the remaining depletion region at a velocity much closer to the saturated value. For example, in GaAs the small upper-valley separation of 0.28 eV limits the ballistic mean free path to about 30 nm. In the indium-bearing materials, $In_{0.53}Ga_{0.47}As$ and InAs, the ballistic mean free path is significantly higher because of the larger upper-valley separation, ~0.5 and 0.9 eV, respectively, in these materials.

In a DBRTD having a very large depletion length, one expects the transit time to be given by $t_T \approx L_D/v_s$, where $v_s$ is the saturation velocity in the depletion layer material. In GaAs, $v_s \approx 0.6 \times 10^7$ cm s$^{-1}$, so that an electron suffers a delay of over 1 ps in a distance of 100 nm. Because of this fact, DBRTDs have usually been designed with $L_D$ somewhat less than 100 nm to maintain a short transit time. However, a long $L_D$ can lead to an enhancement in the magnitude of the terminal NDR, which is the basis for a device called the quantum well injection and transit time diode [77].

## VI. HIGH-SPEED PERFORMANCE CHARACTERISTICS

### A. Small-Signal Impedance Model

The fundamental *RC* time constant, the resonant-tunneling time, and the transit time can be combined into a small-signal impedance model of the DBRTD that is very useful in characterizing high-speed devices. To construct this model, one starts with the double-barrier structure alone, noting that a time-varying potential induces a displacement current in addition to the resonant-tunneling conduction current analyzed in Section V.B. The time-varying potential is assumed to be unaffected by the charge storage in the quantum well. This assumption allows one to neglect the contribution to the impedance of the so-called quantum well capacitance [78], which has a significant effect only in relatively wide quantum wells [79,80]. The displacement current through the double-barrier structure is represented by a capacitance $C_S = \varepsilon A/(L_W + 2L_B)$ in shunt with the complex tunnel admittance $Y_S(\omega)$ of Eq. (8), where $\varepsilon$ is the permittiv-

tial drop in the space charge regions outside of the double-barrier structure, it is assumed for the moment that the conduction current traverses these regions with no transit time delay. The circuit elements $G_S$ and $C_S$ are then simply scaled by the factor $dV_W/dV_D$ and $L_S$ by the inverse to form the lumped-element circuit shown in Fig. 8a. The series resistance $R_S$ in Fig. 8a arises from ohmic dissipation outside the active region of the device, so that $R_S$ is not involved in the scaling. The element $G$ is the differential conductance measured across the terminals of the diode (with $R_S$ properly subtracted), $C$ is the total space charge capacitance, and $L_{QW}$ is the terminal quantum well inductance. The same circuit topology has been derived by two separate theoretical treatments [81,82].

To include the effect of the depletion layer transit time, the electron is assumed to have a constant drift velocity $v_d$ that is an average between the initial group velocity and the terminal velocity. This assumption allows one to apply the small-signal transit time theory that has been successful in describing a variety of fast devices such as IMPATT diodes [83]. In this theory the real part of the admittance of the double-barrier structure is represented as an injection conductance, $\sigma = dJ/dF_W \approx (L_D + 2L_B + L_W + L_A)A^{-1}G(1 + i\omega\tau_n)^{-1}$, where $F_W$ is the electric field (implicitly uniform) across the double-barrier structure. This leads to a total impedance of [24,77]

$$Z_{TT} = \frac{L_D}{i\omega\varepsilon A}\left[1 - \frac{\sigma}{\sigma + i\omega\varepsilon}\frac{1 - \exp(-i\theta_d)}{i\theta_d}\right] + \frac{(L_W + 2L_B + L_A)}{A(\sigma + i\omega\varepsilon)} + R_S(\omega), \tag{9}$$

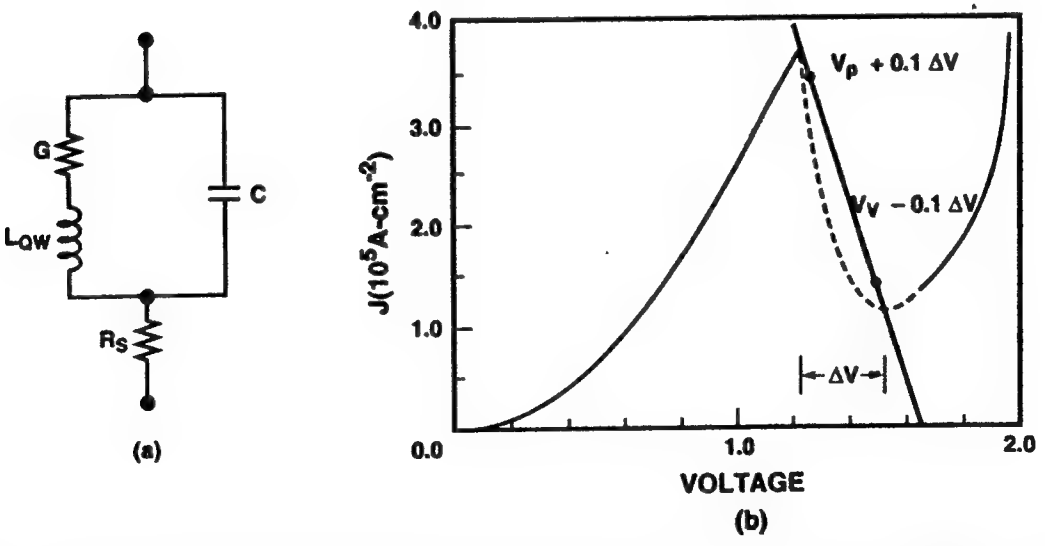


**Fig. 8.** (a) Small-signal equivalent circuit of the DBRTD. (b) Load-line diagram of a DBRTD used to compute the 10 to 90% rise time for switching from the peak point to the valley point.

where $\varepsilon$ is the permittivity of the double-barrier region, and $\theta_d = \omega L_D/v_d$ is the transit angle. The term in square brackets arises from the finite transit time. In the limit of zero frequency, this and the second term reduce to the combination of the space charge resistance $R_{SC} \approx L_D^2/2A\varepsilon v_d$ and the differential resistance. The space charge resistance is associated with mobile charge storage in the depletion layer. In the limit of zero transit angle, these terms reduce to the lumped-element *RCL* model shown in Fig. 8a.

## B. Maximum Oscillation Frequency

Provided that it can be dc biased in the NDR region, the DBRTD is capable of oscillating up to a frequency $f_{max}$ at which the real part of the terminal impedance equals zero. In the limit of infinitesimal transit angle, $f_{max}$ is derived from Fig. 8a:

$$f_{max}^{RCL} = \frac{1}{2\pi}\left\{\left[\frac{1}{L_{QW}C}\left(1 - \frac{C}{2L_{QW}G^2}\right)\right] \times \left[1 - \sqrt{1 - \frac{(GR_S + 1)/GR_S}{(C/2L_{QW}G^2 - 1)^2}}\right]\right\}^{1/2}. \quad (10)$$

In the limit that $L_{QW} \to 0$ or equivalently $\tau_n \to 0$, this solution reduces further to the *RC*-limited result $f_{max}^{RC} = (2\pi C)^{-1}\sqrt{-G/R_S - G^2}$. A real solution to Eq. (10) always exists provided that $|G|R_S < 1$, $G < 0$, and $L_{QW} < 0$. The first condition defines the NDR-region dc-bias provision mentioned above, and the next two are automatically satisfied in the NDR region. Also note that in the NDR region the imaginary part of the impedance of this circuit is always less than zero because $L_{QW}$ is negative. This means that the equivalent circuit in Fig. 8a cannot self-oscillate; i.e., it cannot oscillate by an internal resonance.

Listed in Table I are the theoretical values of $f_{max}^{RCL}$ for some of the fastest DBRTDs fabricated to date. The highest $f_{max}$ values for GaAs/

**TABLE I**

Theoretical Oscillator Characteristics for DBRTDs

| $J_P$ (A cm$^{-2}$) | $G/A$ (mS $\mu$m$^{-2}$) | $C/A$ (fF $\mu$m$^{-2}$) | $\tau_1$ (ps) | $f_{max}$ (GHz) | Reference |
|---|---|---|---|---|---|
| | | $In_{0.53}Ga_{0.47}As/AlAs$ | | | |
| $2.5 \times 10^5$ | −11 | 1.3 | 0.2 | 932 | [107] |
| $5.0 \times 10^5$ | −15 | 1.5 | 0.1 | 1280 | [85] |
| | | GaAs/AlAs | | | |
| $1.5 \times 10^5$ | −6 | 1.5 | 0.1 | 555 | [24] |
| $1.3 \times 10^5$ | −5 | 1.3 | 0.3 | 468 | [25] |

AlAs and $In_{0.53}Ga_{0.47}As$/AlAs diodes are 555 and 1280 GHz, respectively. The superiority of the $In_{0.53}Ga_{0.47}As$/AlAs diode is attributable to a lower magnitude of NDR per unit device area and to a lower specific series resistance.

### C. Switching Time

The NDR region is also the basis for switching from the peak to the valley region of the DBRTD and vice versa. The switching process occurs by dc biasing the device near the peak point through a load resistance $R_L$ that is consistent with two possible dc bias quiescent points (i.e., one above and one below the NDR region). This resistance must satisfy $R_L > \Delta V/\Delta I$. With the device biased initially at the quiescent point near the peak, a slight increase in the bias voltage will then cause a switch to the quiescent point at the valley point or beyond.

A useful estimate of the switching time is obtained by analyzing only the *RC* components without accounting for the resonant-tunneling traversal or transit time delays. The difference in voltage between the initial quiescent point and the final one is assumed to be small enough that the diode capacitance is constant at the peak voltage value. The *I–V* curve in the NDR region is represented by the parabolic form

$$I = \frac{\Delta I}{\Delta V^2}(V - V_V)^2 + I_V, \tag{11}$$

where $\Delta I = I_P - I_V$ and $\Delta V = V_V - V_P$. This expression increases in slope monotonically as the voltage is decreased from the valley point to the peak point. It is thought to be a good approximation to the stable *I–V* curve at all voltages except those just above the peak. For a load resistance equal to $\Delta V/\Delta I$, as shown in Fig. 8b, the time required for the diode voltage to increase from a value 10% above the peak voltage to a value 10% below the valley voltage is given by

$$t_R = \int_{V_P+0.1\Delta V}^{V_V-0.1\Delta V} \frac{C\,dV}{-\Delta I/\Delta V(V - V_V) - \Delta I/\Delta V^2(V - V_V)^2}. \tag{12}$$

Evaluation of this "rise time" integral yields $t_R \approx 4.4\ \Delta V/S$, where $S = (J_P - J_V)/C$ is called the speed index [84].

Theoretical results for the fastest GaAs/AlAs and $In_{0.53}Ga_{0.47}As$/AlAs DBRTDs are given in Table II. The highest *S* and lowest $t_R$ values, by far, are predicted for the diodes having the highest current density [85]. This results in part from a high $\Delta J$ and in part from a small $\Delta V$. A comparison with the oscillator characteristics in Table I leads to the following impor-

**TABLE II**
Theoretical Switching Time for DBRTDs

| $J_P$ (A cm$^{-2}$) | $J_P - J_V$ (A cm$^{-2}$) | $V_V - V_P$ (V) | $S$ ($10^{12}$ V s$^{-1}$) | $t_R$ (ps) | Reference |
|---|---|---|---|---|---|
| | | $In_{0.53}Ga_{0.47}As/AlAs$ | | | |
| $2.5 \times 10^5$ | $2.2 \times 10^5$ | 0.60 | 1.7 | 1.5 | [107] |
| $5.0 \times 10^5$ | $3.3 \times 10^5$ | 0.25 | 2.2 | 0.5 | [85] |
| | | GaAs/AlAs | | | |
| $1.5 \times 10^5$ | $4.3 \times 10^4$ | 0.30 | 0.29 | 4.5 | [24] |
| $1.3 \times 10^5$ | $7.8 \times 10^4$ | 0.40 | 0.60 | 2.9 | [25] |

tant point regarding DBRTDs. The best oscillator diodes are not necessarily the best switching diodes and vice versa. Increasing $\Delta J$ tends to increase oscillator power and decrease switching time in the same manner. Increasing $\Delta V$ also enhances oscillator power, but it increases the switching time because a greater $\Delta V$ requires a greater change of charge stored in $C$.

In considering the subpicosecond value given in Table II, it is important to realize that the neglected resonant-tunneling traversal and transit time delays could have a significant effect. It is expected that the depletion layer transit time will increase $t_R$, but the effect of the quantum-well traversal time [86] is not yet clear.

## VII. HIGH-SPEED EXPERIMENTAL RESULTS

### A. Oscillations

Oscillations can be made to occur in the NDR region at any frequency up to $f_{max}$. One requirement for oscillation is that the device have a dc bias quiescent point in the NDR region so that $R_L < \Delta V/\Delta I$, where $R_L$ is the real part of the dc load impedance. Another requirement for oscillation is that the total impedance be resonant in the sense that the imaginary part equals zero at some frequency. A variety of resonant circuits have been made with DBRTDs, but a waveguide resonator has been the most useful and has yielded the highest-frequency results to date. Waveguide oscillators operating around 50, 100, 200, 350, and 650 GHz have been studied extensively [87].

One of the useful results of oscillator measurements is the determination of $f_{max}$. The comparison between experiment and theory for two diodes is given in Fig. 9. The lower-frequency results are for a diode

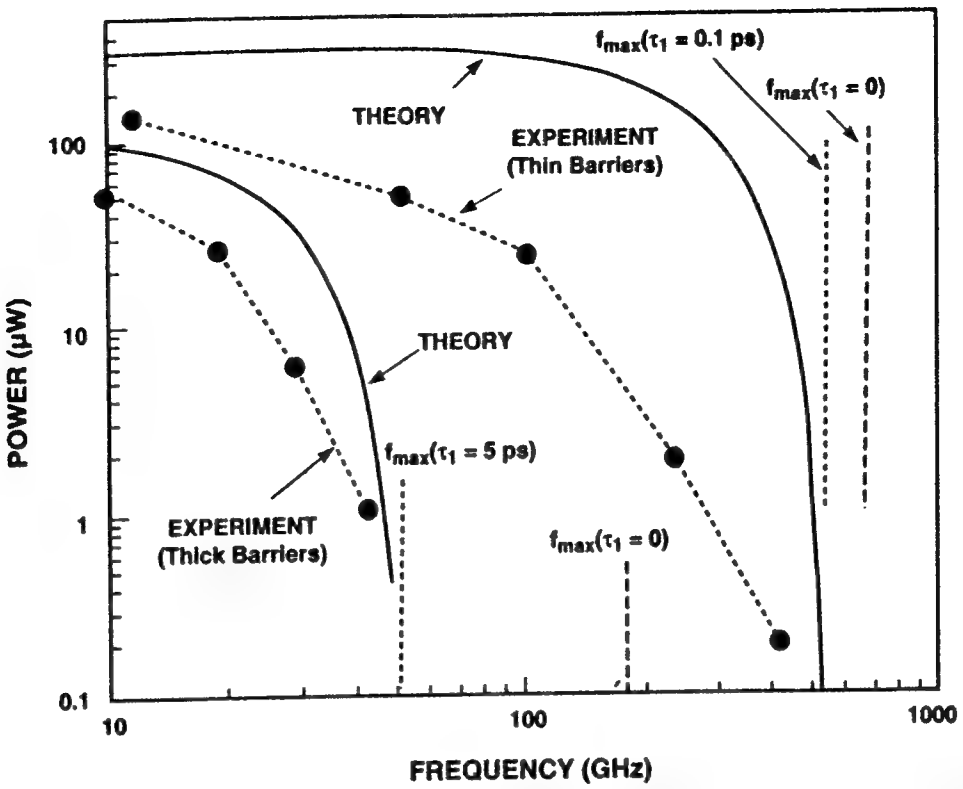


**Fig. 9.** Comparison of experimental and theoretical oscillation results for two DBRTDs. The thick-barrier device has two 5.0-nm-thick $Al_{0.42}Ga_{0.58}As$ barriers and a 5.0-nm-thick GaAs quantum well. The thin-barrier device has two 1.4-nm-thick AlAs barriers and a 4.5-nm-thick GaAs quantum well.

having thick (4.8 nm) $Al_{0.42}Ga_{0.58}As$ barriers, so that $\tau_1 \gg \tau_{RC}$ and $\tau_1 \gg t_T$. This allows one to observe the effect of the quantum well inductance. It is clear from the results that the $f_{max}$ with the quantum well inductance included ($\tau_1 = 5$ ps) provides better agreement with the observed rolloff of oscillation power of this device. The $f_{max}^{RCL}$ of this device is calculated to be 50 GHz, while $f_{max}^{RC}(\tau_1 = 0)$ is 180 GHz. Figure 9 also compares the experiment and theory for the fastest GaAs/AlAs oscillator tested to date. The results are, again, consistent with theory in that the maximum measured oscillation frequency of 420 GHz is below $f_{max}^{RCL}$, which is 520 GHz. The theoretical calculation has a $G$ equal to the maximum slope in the NDR region. A more detailed analysis shows that a threefold reduction in $R_S$ with the same $G$ would increase $f_{max}^{RCL}$ to approximately 900 GHz [24].

The oscillation results for the fastest diodes made to date in all three material systems are presented in Fig. 10. The relatively poor PVCR of the GaAs/AlAs diode limits the power density to a maximum low-frequency value just over $1 \times 10^3$ W cm$^{-2}$. The typical absolute power obtained from a 4-$\mu$m-diameter diode from the fastest GaAs/AlAs mate-

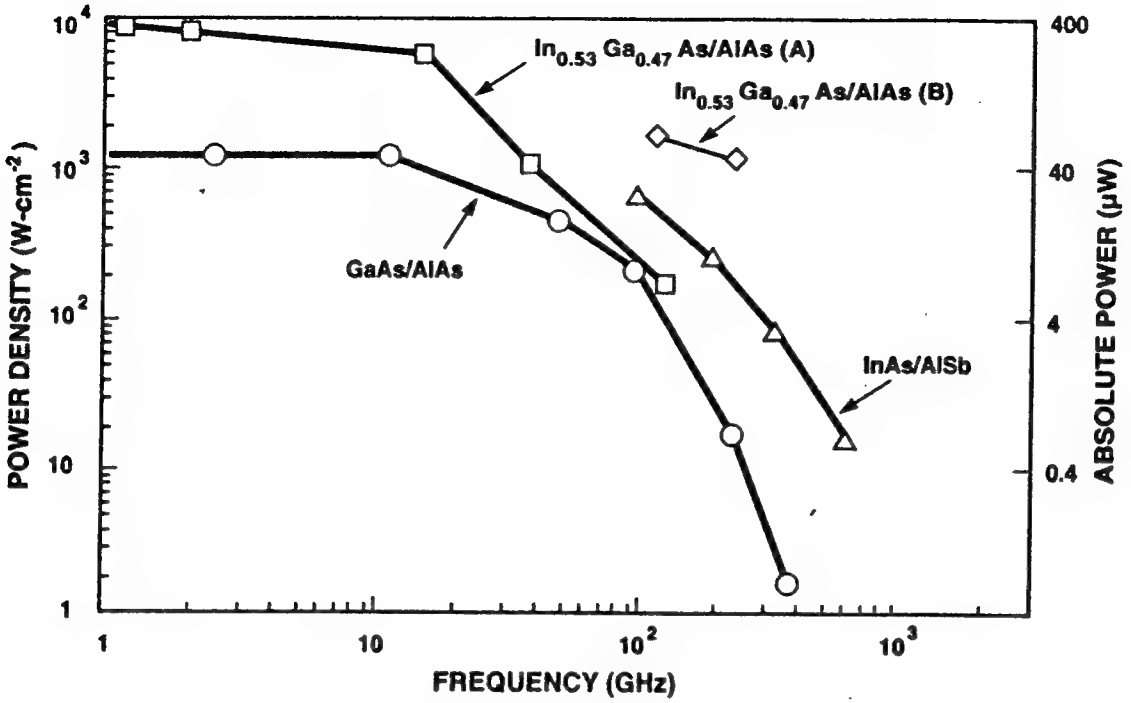


**Fig. 10.** Experimental oscillation results for some of the fastest DBRTDs fabricated from three different material systems.

rial is 15 $\mu$W at 112 GHz and 0.2 $\mu$W at 360 GHz. The superior PVCR of the $In_{0.53}Ga_{0.47}As/AlAs$ diodes provides a low-frequency power density of $1 \times 10^4$ W cm$^{-2}$, which is comparable to that generated by microwave IMPATT diodes. For the $In_{0.53}Ga_{0.47}As/AlAs$ results labeled (A) in Fig. 10, such power densities were maintained up to only 10 GHz because of high device capacitance. A superior $In_{0.53}Ga_{0.47}As/AlAs$ diode, labeled (B) in Fig. 10, was demonstrated with a power density of $1.2 \times 10^3$ W cm$^{-2}$, an absolute power of 50 $\mu$W at 110 GHz, and approximately half of these power levels over 200 GHz. These are the highest oscillation powers obtained from a DBRTD to date above 100 GHz.

DBRTDs made from InAs/AlSb are very promising for submillimeter-wave ($f > 300$ GHz) oscillator applications. The power density of the InAs/AlSb RTD at 360 GHz is about 50 times greater than that of the GaAs/AlAs RTD at the same frequency. The absolute power of a 2-$\mu$m-diameter InAs/AlSb diode at 360 GHz was measured to be 3 $\mu$W, which is about 12-fold more power than obtained from a GaAs/AlAs diode having four times the area. The highest frequency measured to date from InAs/AlSb diodes is 712 GHz [88]. The power density and absolute power at this frequency were measured as 20 W cm$^{-2}$ and 0.5 $\mu$W, respectively. The InAs/AlSb DBRTD should be capable of oscillating up to about 1 THz.

### B. Small-Signal Impedance

Network analysis entails the measurement of the small-signal impedance or admittance of the DBRTD and is most easily done in the positive differential resistance (PDR) region, where the device is inherently ac stable. The first network analysis measurements found that the imaginary part of the impedance contained an inductive component that was practically independent of bias voltage [89]. The physical origin of this inductance was not clear. A second study also found an inductive component in the DBRTD impedance and has shown qualitative agreement between experiment and the small-signal impedance model derived in Section VI.A [90].

More recently, small-signal impedance measurements have been carried out in both the PDR and an ac-stable NDR region by network analysis [80]. The measurements were conducted on a specially designed DBRTD made from the $In_{0.53}Ga_{0.47}As/AlAs$ material system, which had a very low $J_P$ ($\approx$100 A cm$^{-2}$) and a sufficiently high PVCR ($\approx$3.0) at room temperature that the electron transport through the structure was primarily resonant tunneling through the first quasibound state. The experimental $I$–$V$ and $G$–$V$ curves are shown in Fig. 11a. The low $J_P$ allowed the DBRTD to be stabilized against all oscillations in the NDR region, so that an accurate admittance measurement could be made in this region. The results are summarized in Fig. 11b and c for bias voltages of 1.40 and 1.72 V, respectively. In the PDR region at 1.40 V, the conductance is practically independent of frequency and the susceptance is nearly linear, consistent with the simple $RC$ model of the device. In the NDR region at 1.72 V, the conductance displayed a strong frequency dependence and the susceptance showed an obvious inductive character consistent with $L_{QW} = \tau_1/G$ and $\tau_1 = 1.6$ ns. One possible explanation for the absence of inductance in the PDR region is that the resonant-tunneling traversal time is much shorter than in the NDR region because inelastic scattering significantly reduces the quasibound-state lifetime. This issue is presently being investigated.

### C. Electro-optic Measurements of Switching Time

A technique that has measured DBRTD switching with high resolution in the time domain is electro-optic sampling. In one version of this technique, switching was induced by a photoconductive gap in a transmission line [91], and in another version it was induced by electronic means (a pulse-forming circuit) [92]. In the version with a photoconductive switch,

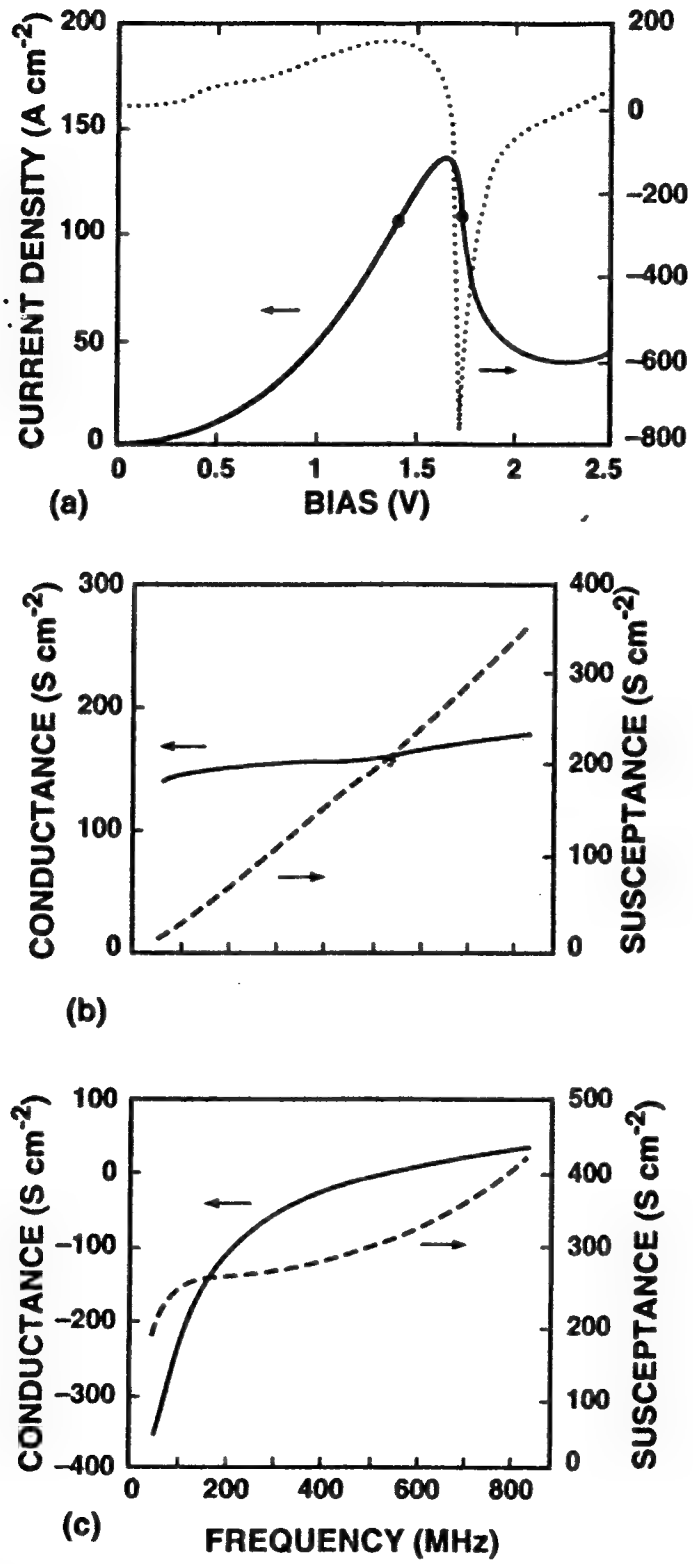


**Fig. 11.** (a) Experimental *I–V* curve of a low-current DBRTD containing two 4.4-nm-thick AlAs barriers and a 5.5-nm-thick $In_{0.53}Ga_{0.47}As$ quantum well. (b) Experimental differential conductance and susceptance (imaginary part of the admittance) vs. frequency for the device in (a) at a bias voltage in the PDR region at 1.40 V. (c) Experimental conductance and susceptance at a bias voltage in the NDR region at 1.72 V (after Ref. 80).

a DBRTD chip was mounted on one conductor of a heterogeneous coupled stripline in such a way that the $n^+$ GaAs substrate made contact to a stripline conductor on an $LiTaO_3$ substrate, and the top mesa was connected (by a whisker) to the conductor on a GaAs substrate. Synchronous pulses from a short-duration (~80 fs) dye laser were used to activate the photoconductive gap on the GaAs substrate and to measure the electric field between the conductors on the $LiTaO_3$ substrate by probing the change of refractive index induced by the switching action of the diode. The elapsed time between the 90 and 10% voltage points was found to be 2.1 ps. The DBRTD structure used for this test consisted of two 1.7-nm-thick AlAs barriers separated by a 4.5-nm-thick GaAs quantum well. It was the same DBRTD structure that oscillated up to approximately 200 GHz [93].

The electro-optic sampling technique with electrical excitation has yielded somewhat longer switching rise times, in the range of 6 to 10 ps [92]. These results were obtained for DBRTDs that, in theory, were at least as fast as the one discussed above. The discrepancy between the two results has been attributed to the fact that the photoconductive switch generates a very fast pulse across the DBRTD that is larger than $\Delta V$ in amplitude. Such a pulse can accelerate the switching process of the DBRTD by the effect known as *overdrive*.

### D. Microwave Noise Power Spectrum

The noise power of high-speed DBRTDs has been measured by a radiometric technique in the PDR region and by an oscillator FM noise technique in the NDR region. In the radiometric technique shown schematically in Fig. 12, the noise power generated by the DBRTD enters a circulator designed for operation around 1 GHz. The circulator feeds the power to a low-noise amplifier chain, and the output power of the amplifiers is measured with a spectrum analyzer in a narrow bandwidth $\Delta f$ centered at 1 GHz. The purpose of the circulator is to make the noise contribution of the amplifier, which is roughly 50% of the total noise, independent of the impedance of the DBRTD. From the noise power at the analyzer, an equivalent shot noise current $I_{eq}$ ($=\gamma I$) is derived using the circuit model of Fig. 12. This is a version of Fig. 8a in which $L_{QW}$ can be neglected because of the relatively low frequency. The thermal noise associated with $R_S$ is represented by a current generator $i_n = (4kT\,\Delta f/R_S)^{1/2}$ and is subtracted from the total noise in the process of deriving $I_{eq}$ at each bias point.

The measurement of noise power in the NDR region is much more difficult because of the strong tendency for high-speed DBRTDs to oscil-

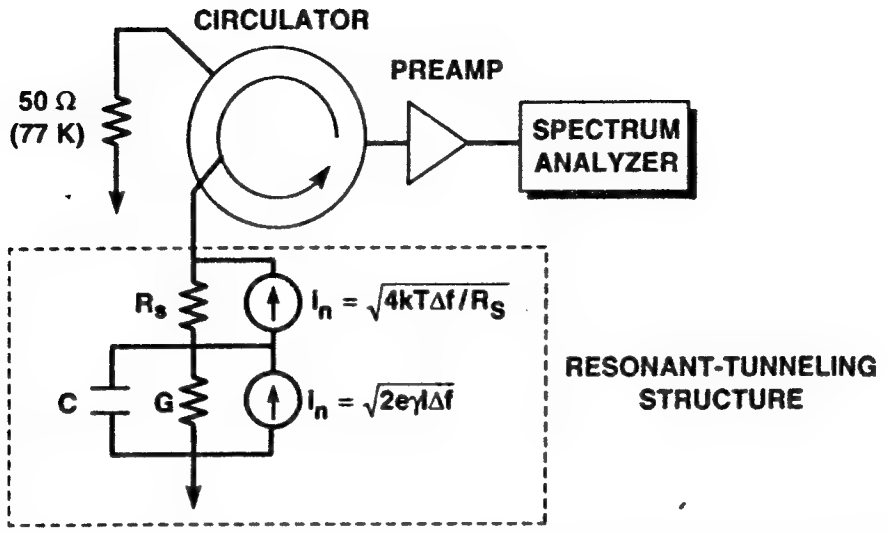


**Fig. 12.** Schematic diagram of technique used to measure microwave noise power of a DBRTD. The dashed box contains the equivalent noise circuit.

late in this region. With this fact in mind, a pragmatic approach is to make the DBRTD oscillate at a suitably low frequency and deduce the noise properties from the FM characteristics of the oscillator power spectrum [94]. This technique provides only an upper limit because other mechanisms, such as $1/f$ noise in the contacts, can contribute significantly to the oscillator power spectrum but are not accounted for in the analysis.

Shown in Fig. 13 are the experimental results at 77 K for the same GaAs/AlGaAs DBRTD as in Figs. 5 and 6. The device exhibits obvious shot noise suppression in the PDR region with a minimum $\gamma$ of approximately 0.35 at a bias voltage just below the current peak. At the lone bias point in the NDR region, the shot noise is enhanced by a factor of 8, in qualitative agreement with the theory discussed in Section IV.D. The results at room temperature were similar except that a lesser degree of suppression and enhancement were measured in the PDR and NDR regions, respectively. In addition, shot noise measurements have been carried out for an $In_{0.53}Ga_{0.47}As$/AlAs DBRTD having much thinner barriers and a much higher $J_P$ than the GaAs/AlGaAs device [94]. This device also had a superior PVCR of 12 at room temperature. The experimental shot noise factor for this diode in the PDR region was qualitatively similar to that of the GaAs/AlGaAs diode, supporting the conclusion that the shot noise suppression mechanism is inherent to all symmetric DBRTDs. Unfortunately, results were not obtained in the NDR region because of the difficulty in making this diode oscillate exclusively at low frequencies.

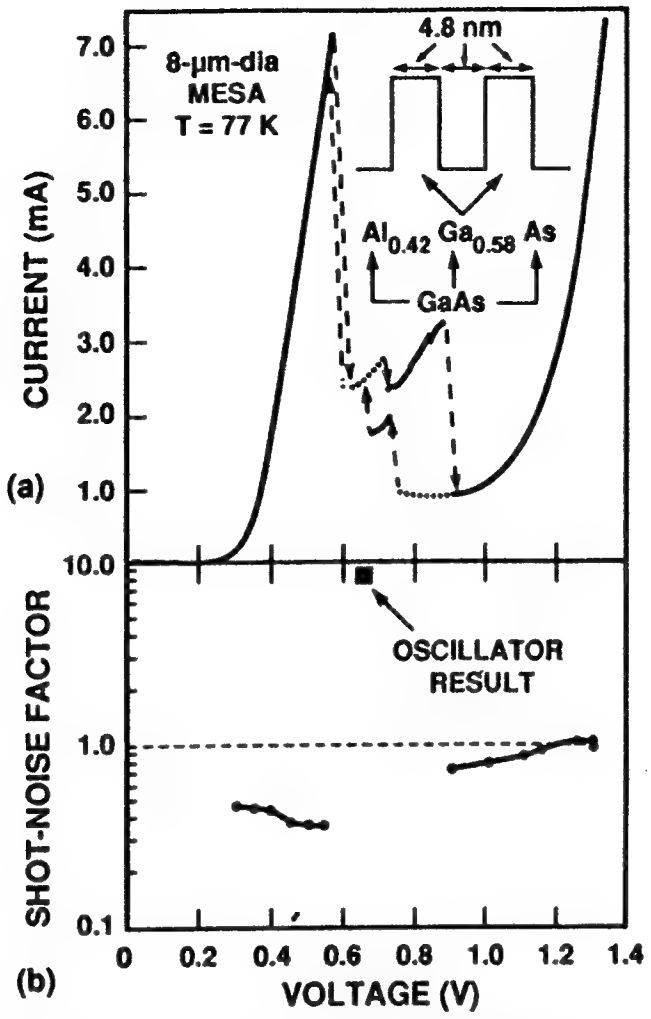


**Fig. 13.** (a) Experimental 77-K $I$–$V$ curve of a GaAs/$Al_{0.42}Ga_{0.58}As$ DBRTD having a 5.0-nm-thick quantum well and 5.0-nm-thick barriers. (b) Experimental shot noise factor of the DBRTD in (a) measured at a frequency of 1.0 GHz.

## VIII. SURVEY OF HIGH-SPEED APPLICATIONS

### A. Device Qualifications

Many of the DBRTD applications investigated up to the present time are analogous to $p$–$n$ (Esaki) tunnel-diode applications of the 1960s [95]. Most of the Esaki diode applications were abandoned with the advent of fast transistors because of the difficulty in designing satisfactory circuits using only two-terminal devices. The DBRTD has three advantages over Esaki diodes that compensate for this shortcoming. First, the DBRTD is roughly 10 times faster than the Esaki diode in both oscillations and switching. This allows the DBRTD to operate in the terahertz–picosec-

ond regimes that presently define the frontier of high-speed electronics. Second, the $I$–$V$ characteristics of DBRTDs can be tailored by *bandgap engineering* over a very broad range. For example, peak current densities can be designed to occur from roughly $10^2$ to $5 \times 10^5$ A cm$^{-2}$ and peak voltages from roughly 0.3 to 3 V, both in the presence of a useful PVCR. Third, DBRTDs are compatible with modern heterostructure transistor devices because they are grown monolithically by the same epitaxial techniques and fabricated by very similar methods. This opens up many possibilities of high-speed DBRTDs used in conjunction with heterostructure transistors to make integrated circuits having superior performance or functionality [96] compared to existing circuits.

At present, dozens of applications of DBRTDs are under development or being proposed. Some of these applications are summarized in the following sections. For a more complete discussion of applications, the reader is referred to one of the review articles on the subject [1,97].

### B. DBRTD Quasioptical Oscillator

The oscillation of the DBRTD at 712 GHz establishes it as the fastest solid-state electronic oscillator demonstrated to date at room temperature. As such, it has the potential to fill the need for coherent power in the region between 100 GHz and 1 THz, where fundamental-frequency solid-state sources are lacking. In this region the primary application of the DBRTD is a low-noise local oscillator for high-sensitivity coherent radiometers. In this application the instantaneous linewidth must be less than about 100 kHz, and the oscillator should be frequency tunable by at least $\pm 1\%$ of the nominal center frequency. A DBRTD oscillator satisfying these requirements is the quasioptical design depicted in Fig. 14a [98].

Shown in Fig. 14b is the experimental power spectrum of the quasioptical oscillator operating near 110 GHz. This particular oscillator contained a DBRTD made from the $In_{0.53}Ga_{0.47}As$/AlAs material system, having an $f_{max}$ of approximately 900 GHz. The oscillator power spectrum had a linewidth of approximately 20 kHz at 10 dB below the peak. The measured power was approximately 50 $\mu$W, which is sufficient to drive the superconducting quasiparticle mixers that operate in this frequency range and is possibly high enough to drive the next generation of cooled Schottky diode mixers made from InGaAs. Future versions of the quasioptical oscillator will operate up to frequencies of at least 500 GHz.

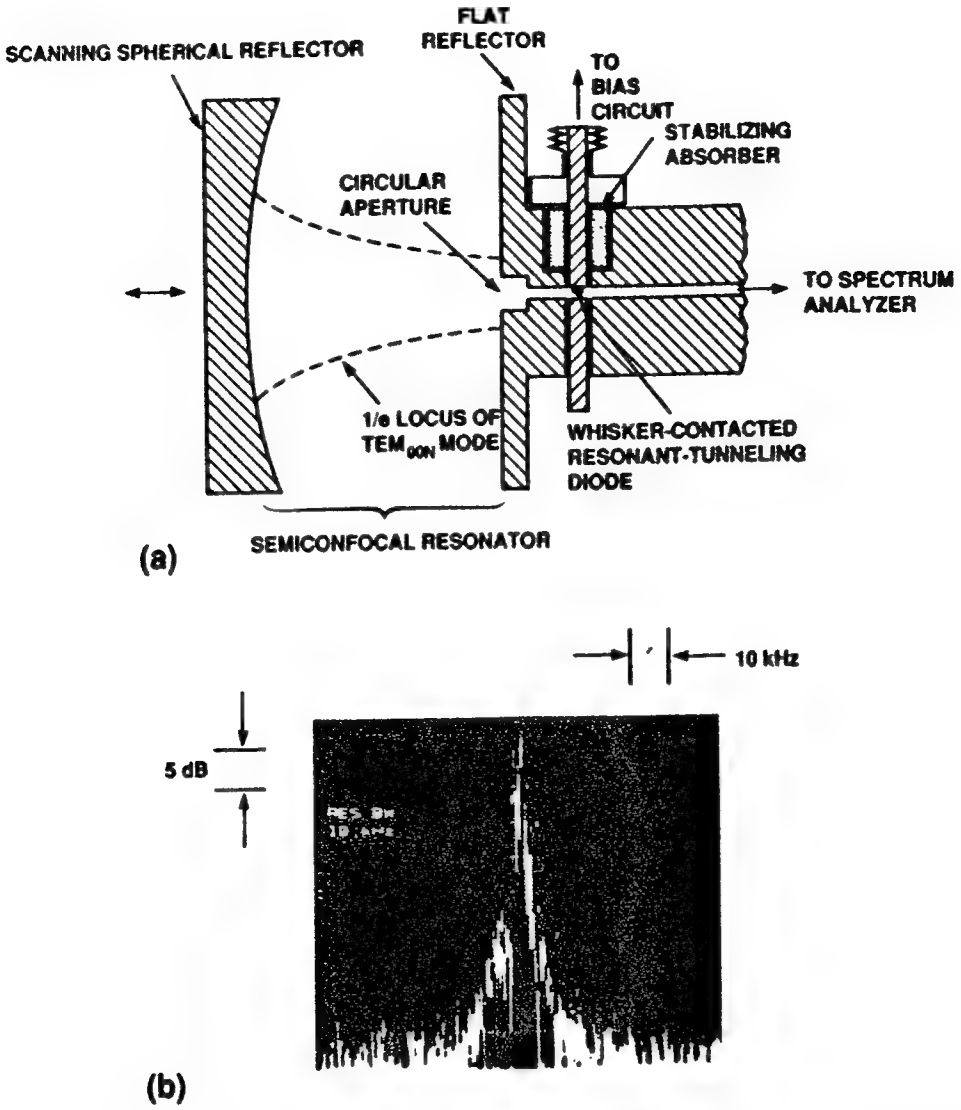


**Fig. 14.** (a) Cross-sectional view of a quasioptically stabilized DBRTD oscillator for operation in the millimeter- and submillimeter-wave regions. (b) Experimental power spectrum of quasioptically stabilized DBRTD oscillator operating near 110 GHz.

## C. DBRTD Pulse-Forming and Trigger Circuits

The fast switching behavior described in Section VI.C makes the DBRTD ideally suited for generating sharp edges in response to slowly varying input waveforms. The basic idea is to take the dc load line in Fig. 8b and superimpose on it an ac drive waveform of arbitrary period. The amplitude of the drive is chosen such that the diode voltage switches from the peak to the valley region as the drive increases from minimum to maximum voltage, and the diode voltage switches back to the peak region

as the drive decreases to its minimum. The resulting current waveform through the DBRTD has sharp leading and lagging edges and, if fed into a circuit separate from the drive circuit (by frequency discrimination techniques), should yield a square wave. With proper design the square wave can be induced with a relatively small amplitude drive waveform, which means there is high voltage gain. Another benefit is that the switching thresholds are well defined by the peak and valley points, so that the sharp edges always occur at the same phase of the drive voltage. This is a required property of a trigger. Monolithic DBRTD-based trigger circuits have been demonstrated alone up to 110 GHz [26] and as an integral part of a sampling head operating up to 26 GHz [99].

### D. DBRTD-Based Waveform Generation and Signal Processing Circuits

The flexibility in design of the DBRTD $I$–$V$ characteristics can be utilized to perform various specialized waveform generation functions. For example, if a DBRTD is grown with compositional and doping profiles that are perfectly symmetrical about the center of the quantum well, the $I$–$V$ curve will be antisymmetrical about the origin. When such an $I$–$V$ curve is driven with a sinusoidal voltage waveform, the current spectrum flowing through the diode will contain only odd harmonics of the drive waveform [100]. Furthermore, if the amplitude of the drive waveform is close to the valley voltage of the DBRTD, and if the PVCR of the DBRTD is sufficiently high, then the power contained in the fifth harmonic can exceed the power in the third. This property is depicted in Fig. 15a. The performance of a prototype microwave fifth-harmonic multiplier is displayed in Fig. 15b. The conversion efficiency from the fundamental drive frequency to the fifth harmonic is approximately 0.3%.

If two or more double-barrier structures are grown in tandem, the overall $I$–$V$ curve will have a sawtooth-like characteristic, similar to that observed with two or more Esaki diodes connected in series but without the parasitic impedance of the interconnect. By designing the DBRTDs properly, the successive peaks in the sawtooth can be separated by nearly equal voltage. This leads to the possibility of multibit analog-to-digital (A/D) conversion. Simulations on such a device have indicated that a 4-bit A/D converter made by this technique should operate up 30 GHz [101].

### E. DBRTDs in Memory and Logic Circuits

When a DBRTD is connected to the source terminal of an FET [102], or to the emitter terminal of a bipolar junction transistor (BJT) [103], a

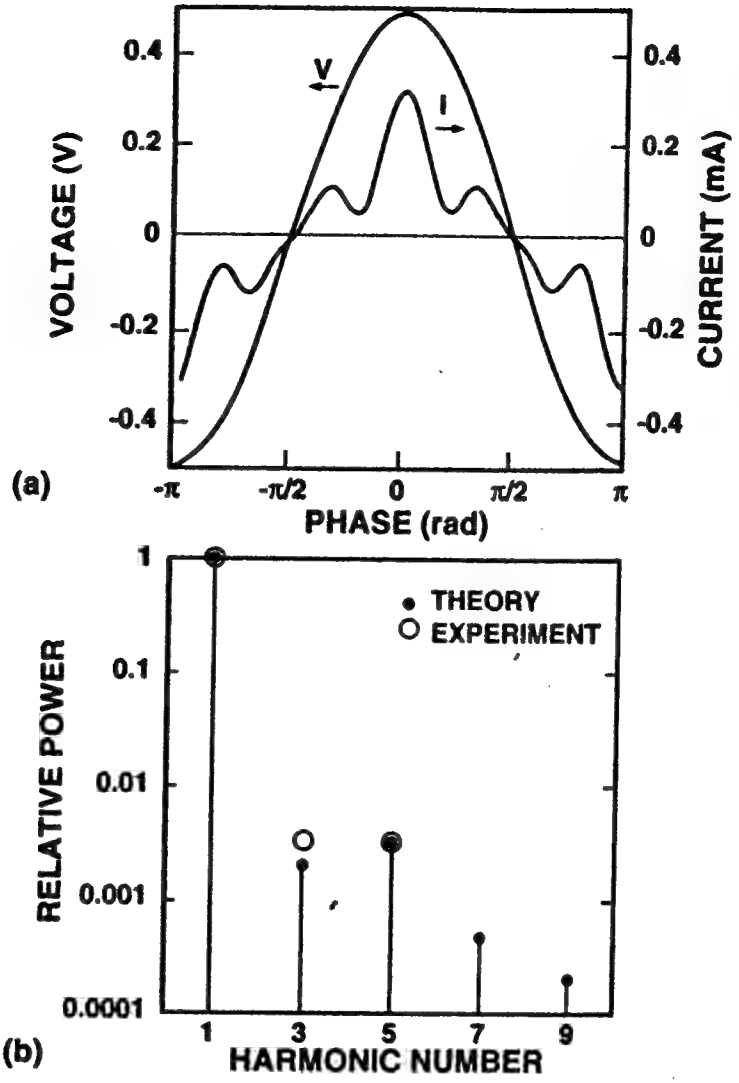


**Fig. 15.** (a) Simulated current waveform through a DBRTD having a perfectly antisymmetric $I$–$V$ curve and driven by a sinusoidal voltage having amplitude greater than $V_p$. (b) Power spectrum of the current in (a) for a voltage waveform frequency of 4.25 GHz.

negative transconductance region is introduced into the $I$–$V$ curves of the transistor–DBRTD combination. When the FET (BJT) transistor is loaded by a suitable resistive load at the drain (collector) terminal, the output at this terminal will be bistable in the sense that two different output states will be possible for the same gate (base) input. Which output state is realized depends on how the input was reached. This is the basis for a latch or a flip-flop, which are the building blocks of sequential (i.e., memory-dependent) logic. When either transistor is loaded by several DBRTDs in tandem, more than two possible output levels are obtained. This raises the possibility of multivalued (i.e., trinary or higher) logic families based on these devices [96].

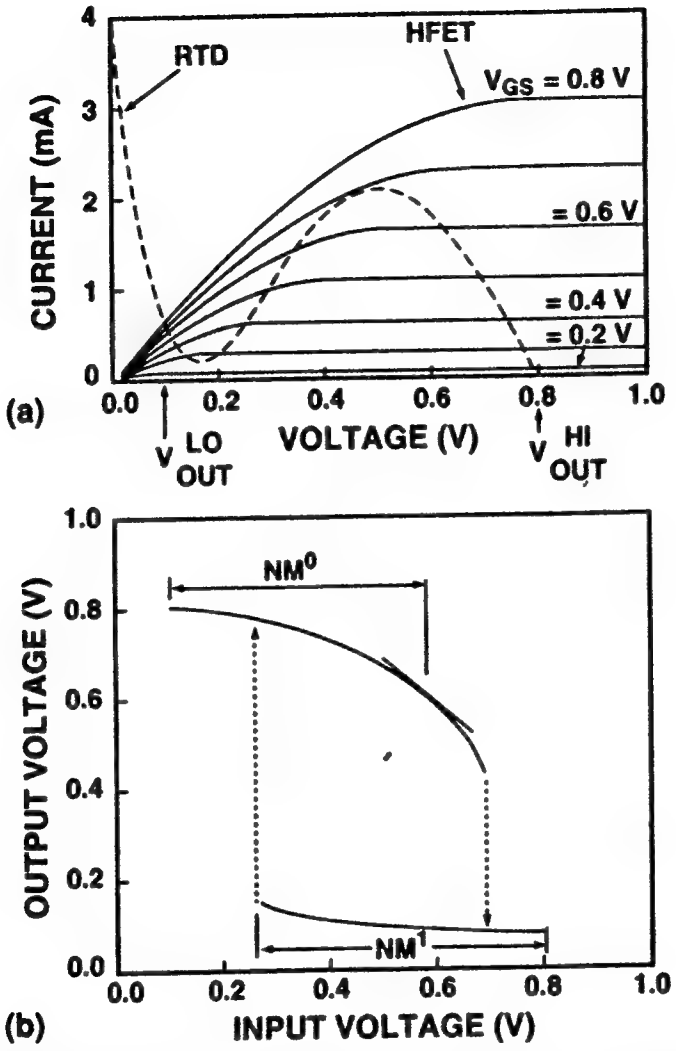


**Fig. 16.** (a) Load line presented by a DBRTD to a heterostructure field effect transistor. (b) Transfer characteristic of the logic-level inverter based on the load line in (a).

Improved performance (in terms of static power dissipation) with similar functionality can be obtained by using the DBRTD as the transistor load at the drain (collector) terminal and grounding the source (emitter). The analogous configuration of an FET and an Esaki diode load was originally proposed by Lehovec [104] as a low-power static RAM cell. It can also function as a low-power inverter for combinational logic. The simulated load line of a heterostructure FET transistor loaded by a DBRTD is shown in Fig. 16a. Clearly, the low static power is achieved by choosing a bias voltage $V_{DD}$ so that the low-output ($V_{OUT}^{LOW}$) logic state is just beyond the valley point of the DBRTD. The resulting static transfer characteristic is shown in Fig. 16b. The large hysteresis in this curve may enhance the logic noise margins, $NM^0$ and $NM^1$, and is also the basis for static-RAM applications. Such a circuit has been fabricated monolithi-

cally and shown to have the desired static properties [105]. This configuration has been predicted by numerical simulation to have a speed competitive with the fastest direct-coupled FET logic [106].

## ACKNOWLEDGMENTS

This work was sponsored by the Department of the Air Force Office, in part under a specific program supported by the Air Force Office of Scientific Research. The author has been fortunate to receive the managerial support of R. A. Murphy and M. A. Hollis and the theoretical support of A. L. McWhorter. The following people are also acknowledged for their recent contributions to the area of high-speed resonant-tunneling diodes: J. P. Mattia, C. D. Parker, K. M. Molvar, C. L. Chen, A. R. Calawa, M. J. Manfra, J. R. Söderström, and T. C. McGill. Finally, this chapter was improved significantly by the careful editorial work of K. J. Challberg of MIT Lincoln Laboratory.

## REFERENCES

1. F. Capasso, S. Sen, and F. Beltram, Quantum-effect devices, in "High-Speed Semiconductor Devices." Wiley, New York, 1990.
2. N. Yokoyama, H. Ohnishi, T. Mori, M. Takatsu, S. Muto, K. Imamura, and A. Shibatomi, in "Hot Electrons in Semiconductor Nanostructures: Physics and Applications" (J. Shah, ed.). Academic, Orlando, Florida, 1992.
3. See Chapter 11 by A. C. Seabaugh and M. A. Reed.
4. L. Esaki and R. Tsu, *IBM J. Res. Dev.* **14,** 61 (1970).
5. R. F. Kazarinov and R. A. Suris, *Sov. Phys. Semicond.* **6,** 120 (1972).
6. L. L. Chang, L. Esaki, and R. Tsu, *Appl. Phys. Lett.* **24,** 593 (1974).
7. T. C. L. G. Sollner, W. D. Goodhue, P. E. Tannenwald, C. D. Parker, and D. D. Peck, *Appl. Phys. Lett.* **43,** 588 (1983).
8. T. J. Shewchuk, P. C. Chapin, P. D. Coleman, W. Kopp, R. Fischer, and H. Morkoc, *Appl. Phys. Lett.* **46,** 508 (1985).
9. M. Tsuchiya, H. Sakaki, and J. Yoshino, *Jpn. J. Appl. Phys.* **24,** L466 (1985).
10. W. D. Goodhue, T. C. L. G. Sollner, H. Q. Le, E. R. Brown, and B. A. Vojak, *Appl. Phys. Lett.* **49,** 1086 (1986).
11. P. J. Price, *Phys. Rev. B* **36,** 1314 (1987).
12. M. Büttiker, *IBM J. Res. Dev.* **32,** 63 (1988).
13. E. Gerjuoy and D. D. Coon, *Superlatt. Microstruct.* **5,** 305 (1989).
14. D. J. BenDaniel and C. B. Duke, *Phys. Rev.* **152,** 683 (1966).
15. R. Tsu and L. Esaki, *Appl. Phys. Lett.* **22,** 562 (1973).
16. G. Bastard, *Phys. Rev. B* **24,** 5693 (1981).
17. J. R. Söderström, E. T. Yu, M. K. Jackson, Y. Rajakarunanayake, and T. C. McGill, *J. Appl. Phys.* **68,** 1372 (1990).
18. J. N. Schulman and T. C. McGill, *Phys. Rev. B* **23,** 4149 (1981).
19. E. O. Kane, *J. Phys. Chem. Solids* **8,** 38 (1959).
20. C. Mailhiot, T. C. McGill, and J. N. Schulman, *J. Vac. Sci. Technol. B* **1,** 439 (1983).
21. J. M. Ziman, "Principles of the Theory of Solids," 2nd ed. Cambridge, London, 1972.

22. S. Luryi, *Appl. Phys. Lett.* **47,** 490 (1985).
23. C. I. Huang, M. J. Paulus, C. A. Bozada, S. C. Dudley, K. R. Evans, C. E. Stutz, R. L. Jones, and M. E. Chaney, *Appl. Phys. Lett.* **51,** 121 (1987).
24. E. R. Brown, T. C. L. G. Sollner, C. D. Parker, W. D. Goodhue, and C. L. Chen, *Appl. Phys. Lett.* **55,** 1777 (1989).
25. S. K. Diamond, E. Ozbay, M. J. W. Rodwell, D. M. Bloom, Y. C. Pao, E. Wolak, and J. S. Harris, Jr., *IEEE Electron Device Lett.* **10,** 104 (1989).
26. E. Ozbay and D. M. Bloom, *IEEE Electron Device Lett.* **12,** 480 (1991).
27. P. Cheng and J. S. Harris, *Appl. Phys. Lett.* **56,** 1676 (1990).
28. V. K. Reddy, A. J. Tsao, and D. P. Neikirk, *Electron. Lett.* **26,** 1742 (1990).
29. K. L. Lear, W. S. Lee, and J. S. Harris, *IEEE Trans. Electron Devices* **36,** 2619 (1989).
30. H. M. Yoo, S. M. Goodnick, and J. R. Arthur, *Appl. Phys. Lett.* **56,** 84 (1990).
31. T. Inata, S. Muto, Y. Nakata, T. Fujii, H. Ohnishi, and S. Hiyamizu, *Jpn. J. Appl. Phys.* **25,** L983 (1986).
32. S. Sen, F. Capasso, A. L. Hutchinson, and A. Y. Cho, *Electron. Lett.* **23,** 1229 (1987).
33. A. A. Lakhani, R. C. Potter, D. Beyea, H. H. Hier, E. Hempfling, L. Aina, and J. M. O'Connor, *Electron. Lett.* **24,** 153 (1988).
34. T. Inata, S. Muto, Y. Nakata, T. Fujii, H. Ohnishi, and S. Hiyamizu, *Jpn. J. Appl. Phys.* **26,** L1332 (1987).
35. T. P. E. Broekaert, W. Lee, and C. G. Fonstad, *Appl. Phys. Lett.* **53,** 1545 (1988).
36. X. J. Song, J. B. Kuang, W. J. Schaff, P. J. Tasker, K. Yamasaki, and L. F. Eastman, *Proc. SPIE* **1288,** 136 (1990).
37. A. W. Higgs, L. L. Taylor, N. Apsley, S. J. Bass, and H. J. Hutchinson, *Electron. Lett.* **24,** 322 (1988).
38. J. R. Söderström, E. R. Brown, C. D. Parker, L. J. Mahoney, and T. C. McGill, *Appl. Phys. Lett.* **58,** 275 (1991).
39. K. Brennan and K. Hess, *Solid-State Electron.* **27,** 347 (1984).
40. E. R. Brown, S. J. Eglash, and C. L. Chen, unpublished.
41. J. R. Söderström, D. H. Chow, and T. C. McGill, *Appl. Phys. Lett.* **55,** 1094 (1989).
42. D. H. Chow, J. R. Söderström, D. A. Collins, C. Z.-Y. Ting, E. T. Yu, and T. C. McGill, *Proc. SPIE* **1283,** 2 (1990).
43. R. Beresford, L. Luo, K. F. Longenbach, and W. I. Wang, *Appl. Phys. Lett.* **56,** 551 (1990).
44. D. A. Collins, D. H. Chow, and T. C. McGill, *Appl. Phys. Lett.* **58,** 1673 (1991).
45. R. Beresford, L. Luo, and W. I. Wang, *J. Cryst. Growth* **111,** 651 (1991).
46. J. R. Söderström, J. Y. Yao, and T. G. Andersson, *Appl. Phys. Lett.* **58,** 708 (1991).
47. D. C. Houghton, H. C. Liu, D. Landheer, M. Buchanan, and M. D'Iorio, *Proc. SPIE* **943,** 65 (1988).
48. H. C. Liu, D. Landheer, M. Buchanan, D.C. Houghton, M. D'Iorio, and S. Kechang, *Superlatt. Microstruct.* **5,** 213 (1989).
49. U. Gennser, V. P. Kesan, S. S. Iyer, T. J. Bucelot, and E. S. Yang, *J. Vac. Sci. Technol. B* **8,** 210 (1990).
50. I. Pereyra, M. P. Carreno, and F. Alvarez, *J. Non-Cryst. Solids* **110,** 175 (1989).
51. E. T. Koenig, B. Jogai, M. J. Paulus, C. I. Huang, and C. A. Bozada, *J. Appl. Phys.* **68,** 3525 (1990).
52. J. S. Wu, C. Y. Chang, C. P. Lee, K. H. Chang, and D. G. Liu, *Solid-State Electron.* **34,** 403 (1991).
53. C. B. Duke, Tunneling in solids, in "Solid State Physics," supplement to Vol. 10. Academic Press, New York, 1969.
54. T. Weil and B. Vinter, *Appl. Phys. Lett.* **50,** 1281 (1987).

55. T. C. L. G. Sollner, *Phys. Rev. Lett.* **59,** 1622 (1987).
56. F. W. Sheard and G. A. Toombs, *Appl. Phys. Lett.* **52,** 1228 (1988).
57. K. M. S. V. Bandara, D. D. Coon, and H. Zhao, *J. Appl. Phys.* **66,** 1227 (1989).
58. V. J. Goldman, D. C. Tsui, and J. E. Cunningham, *Phys. Rev. Lett.* **58,** 1256 (1987).
59. E. S. Alves, L. Eaves, M. Henini, O. H. Hughes, M. L. Leadbeater, F. W. Sheard, G. A. Toombs, G. Hill, and M. A. Pate, *Electron. Lett.* **24,** 1190 (1988).
60. A. V. Zaslavsky, V. J. Goldman, D. C. Tsui, and J. E. Cunningham, *Appl. Phys. Lett.* **53,** 1408 (1988).
61. H. C. Liu, M. Buchanan, G. C. Aers, Z. R. Wasilewski, W. T. Moore, R. L. S. Devine, and D. Landheer, *Phys. Rev. B* **43,** 7086 (1991).
62. M. Cahay, M. McLennan, S. Datta, and M. S. Lundstrom, *Appl. Phys. Lett.* **50,** 612 (1987).
63. W. R. Frensley, *Phys. Rev. B* **36,** 1570 (1987).
64. A. van der Ziel, "Noise in Solid State Devices and Circuits," Chapter 3. Wiley, New York, 1986.
65. E. R. Brown, *IEEE Trans. Electron Devices* **39,** 2686 (1992).
66. E. E. Mendez, W. I. Wang, E. Calleja, and C. E. T. Goncalves da Silva, *Appl. Phys. Lett.* **50,** 1263 (1987).
67. P. J. Price, *Surf. Sci.* **196,** 394 (1988).
68. D. Landheer, H. C. Liu, M. Buchanan, and R. Śtoner, *Appl. Phys. Lett.* **54,** 1784 (1989).
69. A. C. Marsh, *IEEE J. Quantum Electron.* **23,** 371 (1987).
70. K. V. Rousseau, K. L. Wang, and J. N. Schulman, *Appl. Phys. Lett.* **54,** 1341 (1989).
71. F. Chevoir and B. Vinter, *Appl. Phys. Lett.* **55,** 1859 (1989).
72. N. S. Wingreen, K. W. Jacobsen, and J. W. Wilkins, *Phys. Rev. Lett.* **61,** 1396 (1988).
73. J. Leo and A. H. McDonald, *Phys. Rev. Lett.* **64,** 817 (1990).
74. E. R. Brown, C. D. Parker, and T. C. L. G. Sollner, *Appl. Phys. Lett.* **54,** 934 (1989).
75. R. K. Mains and G. I. Haddad, *J. Appl. Phys.* **64,** 3564 (1988).
76. L. F. Eastman, Cornell University, private correspondence.
77. V. P. Kesan, D. P. Neikirk, B. G. Streetman, and P. A. Blakey, *IEEE Trans. Electron Devices* **35,** 405 (1988).
78. S. Luryi, *Appl. Phys. Lett.* **52,** 501 (1988).
79. E. F. Schubert, F. Capasso, A. L. Hutchinson, S. Sen, and A. Gossard, *Appl. Phys. Lett.* **57,** 2820 (1991).
80. J. P. Mattia, Master's thesis, Massachusetts Institute of Technology, 1991.
81. H. C. Liu, *Phys. Rev. B* **43,** 12538 (1991).
82. H. Y. Sheng and J. Sinkkonen, *Superlatt. Microstruct.* **9,** 537 (1991).
83. D. J. Coleman, Jr. and S. M. Sze, *Bell Syst. Tech. J.* **50,** 1695 (1971).
84. S. Sze, "Physics of Semiconductor Devices." Wiley, New York, 1981.
85. T. P. E. Broekaert and C. G. Fonstad, "International Electron Devices Meeting Technical Digest," p. 559. IEEE, New York, 1989.
86. S. K. Diamond, E. Ozbay, M. J. W. Rodwell, D. M. Bloom, Y. C. Pao, and J. S. Harris, Jr., *Appl. Phys. Lett.* **54,** 153 (1989).
87. E. R. Brown, Resonant tunneling in high-speed double-barrier diodes, in "Hot Electrons in Semiconductor Nanostructures: Physics and Applications" (J. Shah, ed.), p. 469. Academic Press, Orlando, Florida, 1992.
88. E. R. Brown, J. R. Sōderstrōm, C. D. Parker, L. J. Mahoney, K. M. Molvar, and T. C. McGill, *Appl. Phys. Lett.* **58,** 2291 (1991).
89. J. M. Gering, D. A. Crim, D. G. Morgan, and P. D. Coleman, *J. Appl. Phys.* **61,** 271 (1987).

90. D. W. Whitson, M. J. Paulus, C. E. Stutz, E. Koenig, R. Neidhard, and K. R. Evans, in "Proceedings of the IEEE/Cornell Conference," p. 301. IEEE, New York, 1989.
91. J. F. Whitaker, G. A. Mourou, T. C. L. G. Sollner, and W. D. Goodhue, *Appl. Phys. Lett.* **53,** 385 (1988).
92. S. K. Diamond, E. Ozbay, M. J. W. Rodwell, D. M. Bloom, Y. C. Pao, E. Wolak, and J. S. Harris, Jr., in "OSA Proceedings on Picosecond Electronics and Optoelectronics," Vol. 4, p. 101. Optical Society of America, Washington, D.C., 1989.
93. E. R. Brown, W. D. Goodhue, and T. C. L. G. Sollner, *J. Appl. Phys.* **64,** 1519 (1988).
94. E. R. Brown, C. D. Parker, A. R. Calawa, and M. J. Manfra, *IEEE Trans. Electron Devices* **38,** 2716 (1991).
95. J. M. Carroll, "Tunnel-Diode and Semiconductor Circuits." McGraw-Hill, New York, 1963.
96. F. Capasso, S. Sen, F. Beltram, L. Lunardi, A. Vengurlekar, P. Smith, N. Shah, R. Malik, and A. Choh, *IEEE Trans. Electron Devices* **36,** 2065 (1989).
97. T. C. L. G. Sollner, E. R. Brown, W. D. Goodhue, and H. Q. Le, in "Physics of Quantum Electron Devices" (F. Capasso, ed.), p. 147. Springer, New York, 1990.
98. E. R. Brown, C. D. Parker, K. M. Molvar, and K. D. Stephan, *IEEE Trans. Microwave Theory and Tech.* **40,** 846 (1992).
99. A. Miura, S. Kobayashi, T. Yakihara, S. Uchida, H. Kamada, and S. Oka, in "International Microwave Symposium Digest," p. 1845. IEEE, New York, 1990.
100. T. C. L. G. Sollner, E. R. Brown, W. D. Goodhue, and C. A. Correa, *J. Appl. Phys.* **64,** L4248 (1988).
101. R. C. Potter, D. Shupe, T. H. Kuo, and H. C. Lin, in "IEEE International Symposium on Circuits and Systems," p. 2557. IEEE, New York, 1990.
102. T. K. Woodward and T. C. McGill, *Superlatt. Microstruct.* **4,** 1 (1988).
103. S. Sen, F. Capasso, A. Y. Cho, and D. L. Sivco, *IEEE Electron Device Lett.* **9,** 533 (1988).
104. K. Lehovec, *IEEE J. Solid-State Circuits* **14,** 797 (1979).
105. K. L. Lear, K. Yoh, and J. S. Harris, in "Proc. International Symposium GaAs and Related Compounds," p. 593. IEEE, New York, 1989.
106. E. R. Brown, M. A. Hollis, F. W. Smith, K. C. Wang, and P. M. Asbeck, in "Proc. International Solid-State Circuits Conference," p. 142. IEEE, New York, 1992.
107. E. R. Brown, C. D. Parker, A. R. Calawa, M. J. Manfra, T. C. L. G. Sollner, C. L. Chen, S. W. Pang, and K. M. Molvar, *Proc. SPIE* **1288,** 122 (1990).